iras *Sky Survey Atlas*

EXPLANATORY SUPPLEMENT

S. L. Wheelock

T. N. Gautier

J. Chillemi

D. Kester

H. McCallon

C. Oken

J. White

D. Gregorich

F. Boulanger

J. Good

T. Chester

Infrared Processing and Analysis Center
Jet Propulsion Laboratory

May 1994

The Infrared Astronomical Satellite (IRAS) was a joint project of NASA (U.S.), NIVR (The Netherlands) and SERC (U.K.).

PREFACE

This Explanatory Supplement accompanies the *IRAS Sky Survey Atlas* (ISSA) and the *ISSA Reject Set*. The first ISSA release in 1991 covers completely the high *ecliptic* latitude sky, $|\beta| > 50°$, with some coverage down to $|\beta| \approx 40°$. The second ISSA release in 1992 covers *ecliptic* latitudes of $50° > |\beta| > 20°$, with some coverage down to $|\beta| \approx 13°$. The remaining fields covering latitudes within 20° of the *ecliptic* plane are of reduced quality compared to the rest of the ISSA fields and therefore are released as a **separate** IPAC product, the *ISSA Reject Set*. The reduced quality is due to contamination by zodiacal emission residuals. Special care should be taken when using the *ISSA Reject* images (§IV.F).

In addition to information on the ISSA images, some information is provided in this Explanatory Supplement on the *IRAS Zodiacal History File* (ZOHF), Version 3.0, which was described in the December 1988 release memo (Appendix H).

The data described in this Supplement are available at the National Space Science Data Center (NSSDC) at the Goddard Space Flight Center. The interested reader is referred to the NSSDC for access to the *IRAS Sky Survey Atlas* (ISSA).

For additional information concerning ISSA, please contact:

Guest Investigator Support
Infrared Processing and Analysis Center
Mail Code 100-22
California Institute of Technology
Pasadena, CA 91125

S. Wheelock, T.N. Gautier and T. Chester
Pasadena
November 1993

TABLE OF CONTENTS

INDEX OF TABLES

II. IRAS SKY SURVEY ATLAS OVERVIEW

III. PROCESSING

IV. ANALYSIS RESULTS

V. FORMATS FOR THE IRAS SKY SURVEY ATLAS (ISSA)

APPENDIX A

INDEX OF FIGURES

I. INTRODUCTION

II. IRAS SKY SURVEY ATLAS OVERVIEW

III. PROCESSING

IV. ANALYSIS RESULTS

APPENDIX D

APPENDIX F

APPENDIX G

APPENDIX H

I. INTRODUCTION

A. General Overview

The *Infrared Astronomical Satellite* (IRAS) conducted a survey of 98% of the sky from low Earth orbit in four bands with effective wavelengths of 12, 25, 60 and 100 μm during a ten month period from January to November, 1983. The purpose of the survey was to produce an extremely reliable catalog of infrared point sources at a sensitivity unobtainable from within the Earth's atmosphere. The good stability of the IRAS infrared detectors allowed radiometry of extended astronomical sources with the IRAS survey data. The original extended emission atlas, known as *SkyFlux* and consisting of 16.5° square surface brightness images, was released along with the *IRAS Point Source Catalog* between 1984 and 1986 (*IRAS Catalogs and Atlases: Explanatory Supplement*, 1988, ed. C. A. Beichman *et al.* (Washington D.C.:GPO)).

The 16.5° × 16.5° *SkyFlux* images gave a broad view of infrared emission from the Galaxy and the solar system with high angular resolution and unprecedented sensitivity. It was clear, however, that large improvements in sensitivity and photometric accuracy were obtainable using knowledge gained in the production and analysis of the original IRAS data products. Accordingly, the Infrared Processing and Analysis Center (IPAC) reprocessed the IRAS data to produce improved images. The results of the reprocessing are now available as the *IRAS Sky Survey Atlas* (ISSA). The ISSA covers the sky with 430 fields. Each field is a 12.5° × 12.5° region centered every 10° along declination bands which are spaced 10° apart. There are two releases of the ISSA. The first release, in 1991, completely covers high ecliptic latitudes ($|\beta| > 50°$) with some coverage down to $|\beta| \approx 40°$. The second release, in 1992, covers ecliptic latitudes of $50° > |\beta| > 20°$ with some coverage down to $|\beta| \approx 13°$. The remaining fields between ecliptic latitudes $-20°$ to 20° are released as a separate product, the *ISSA Reject Set*, so named because of their reduced quality compared to the rest of the ISSA. These fields are contaminated by zodiacal emission residuals and zodiacal dust bands. The *ISSA Reject Set* is usable for many applications but *special* care should be taken when using these data for photometric measurements (§I.D.3 and §IV.F). This *IRAS Sky Survey Atlas Explanatory Supplement* describes in detail the production, analysis and formats of the *Atlas*.

The scientific motivation for ISSA is to present consistently calibrated infrared images of the entire sky from IRAS at spatial scales larger than 5′. The combination of calibration improvements (§III.A.2), removal of most of the zodiacal foreground (§III.C.2), and detector destriping (§III.C.3) result in a sensitivity increase of a factor greater than five over the *SkyFlux* images at short IRAS wavelengths. This is enough to reveal Galactic dust features previously invisible at 12 and 25 μm. Detector noise is the limiting noise of ISSA for small spatial scales at most locations above 20° ecliptic latitude. At latitudes within 20° of the ecliptic plane (the *ISSA Reject* region) the limiting noise is due to zodiacal dust bands and residual zodiacal emission.

The ISSA images are designed to give relative photometry for objects outside the solar system. They *cannot* be used for determining the absolute sky surface brightness.

Section §II.B gives important details about the calibration of IRAS. *The comparison of IRAS results with the Diffuse Infrared Background Experiment (DIRBE) on the Cosmic Background Explorer (COBE) satellite should be understood before using ISSA images for quantitative photometric measurements* (§IV.D.3).

The remainder of this Introduction provides a refresher on those aspects of the IRAS telescope and the IRAS survey needed to understand the ISSA images. It will define the terms and introduce the concepts used in this document. A collection of cautionary notes vital for the correct use of the ISSA images is also presented. An overview of the changes and improvements made since the *SkyFlux* atlas was released is presented in Chapter II. Chapter III gives a description of the processing used to produce the Atlas. Chapter IV presents results from analysis of the ISSA and the *ISSA Reject* images. Chapter V details the formats of the ISSA images.

B. The IRAS Survey

Complete details of the designs of the IRAS telescope and instruments, the IRAS sky survey and the IRAS data processing system, along with extensive descriptions of the IRAS data products, are contained in the *IRAS Explanatory Supplement* 1988, hereafter referred to as the *Main Supplement*. Short descriptions of the IRAS survey instrument and the survey design are included here for easy reference.

IRAS was launched into a Sun-synchronous polar orbit at 900 km altitude over the Earth's terminator to facilitate long scans of the sky along portions of circles centered on the Sun (Figure I.B.1 and *Main Supplement*, §III.B). This orbit geometry would have allowed the IRAS telescope to view the whole sky in exactly six months if it had remained pointed exactly 90° from the Sun. The IRAS survey strategy used the ability of the satellite to point at varying angles from the Sun to complete two confirming surveys of 98% of the sky and a third confirming survey of 75% of the sky within the ten month operating period of the satellite.

Each confirming survey, called an **HCON** for **H**ours **CON**firmation (*Main Supplement*, §III.A), consisted of a series of Sun-centered scans in which the 1/2°-wide focal plane array was moved by 1/4° between scans. In this way a double coverage of the sky was accomplished by scans separated by up to 36 hours, allowing point source detections from one scan to be correlated with other scans to confirm the reality of detections. Two HCONs (HCON-1 and HCON-2) were performed concurrently in the first six months of the IRAS mission, with the second HCON lagging behind the first by a few weeks. Solar elongation angles, ϵ, of the telescope line of sight were roughly confined to 80°–100° during HCON-1 and HCON-2. The third survey, HCON-3, was begun after the completion of the first two and used the full available range of solar elongation (60°–120°) in an attempt to cover the whole sky in less than six months. The third HCON was only 75% complete when it was terminated by exhaustion of the IRAS liquid helium supply.

A significant feature of the IRAS survey strategy is that zodiacal emission, arising from interplanetary dust in the solar system, presented a constantly changing source of

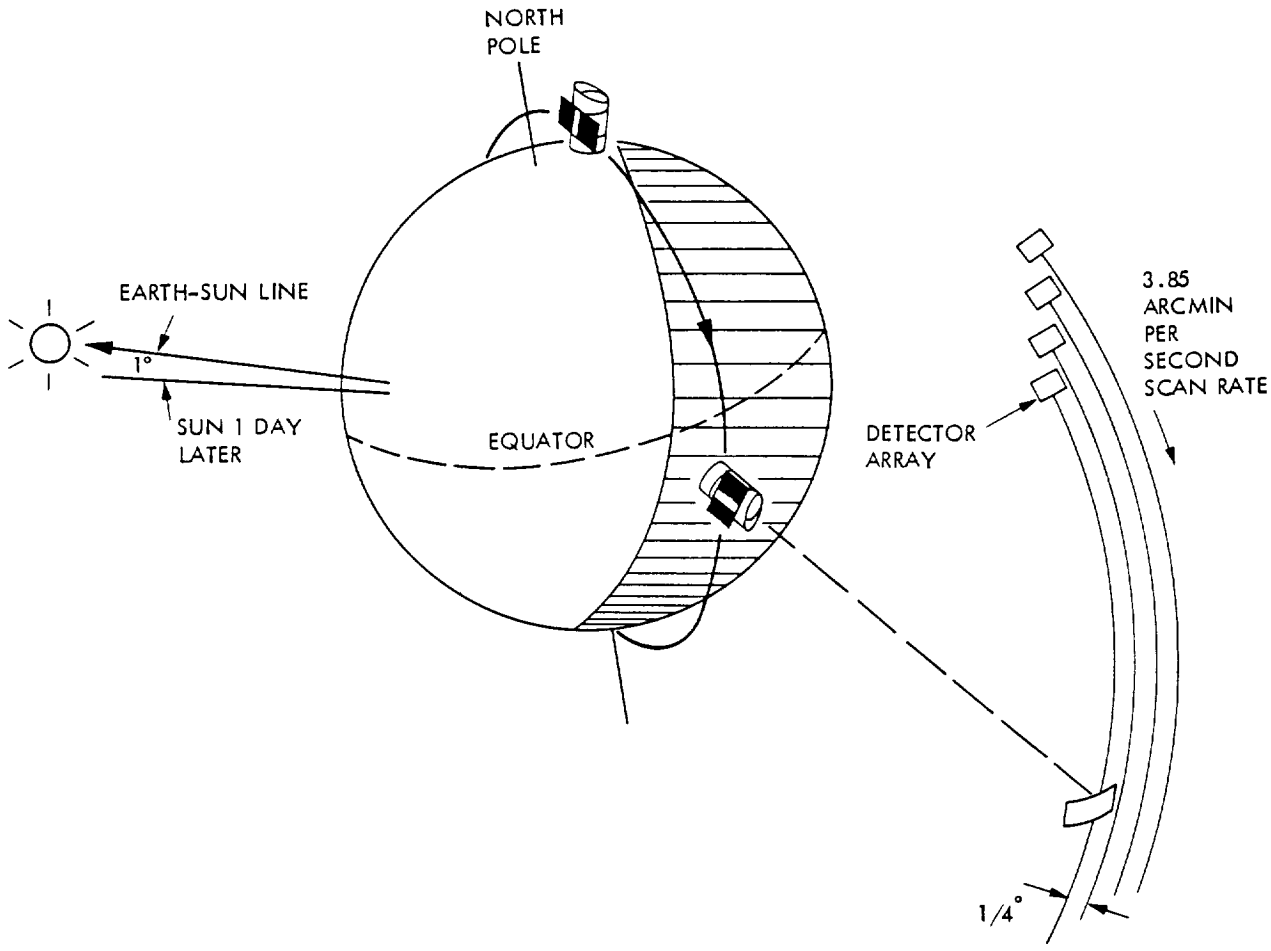

Figure I.B.1 A schematic drawing of the orbital geometry. The orbital altitude, 900 km, and inclination, 99°, combined with the Earth's equatorial bulge, led to a precession of the plane of the orbit of about 1° per day. As a result, the orbit plane constantly faced the Sun as the satellite orbited near the Earth's terminator. By pointing the satellite radially away from the Earth, the cold telescope was shielded from the heat loads from the Sun and Earth while providing natural scanning motion across the entire sky in about six months. A sequence of hours-confirming scans on the celestial sphere is also shown.

---

foreground emission through which IRAS observed. Two observations of the same point on the celestial sphere separated by as little as a few days would measure significantly different surface brightnesses because the Earth moved in its orbit and changed the line of sight through the zodiacal dust cloud. This variation produced steep gradients in individual

HCON images where adjacent locations on the sky were scanned at different times. This prevented direct co-addition of separate HCONs. The variation in zodiacal foreground was most troublesome at 12 and 25 μm (15% to 30% depending on the HCON) which fall near the peak wavelength of the zodiacal emission. At the longer wavelengths, diffuse Galactic emission becomes much stronger than zodiacal emission, reducing the effects of zodiacal variation.

The focal plane array of the IRAS survey instrument consisted of 62 detectors with either 15 or 16 detectors at each of the four IRAS wavelengths (Figure I.B.2). The telescope was oriented so that, during survey scans, the image of the sky moved across the array in the long direction at 3.85′ s^{-1}, producing complete coverage of a 0.5°-wide swath of sky. The four staggered rows of detectors in each wavelength band were designed to provide slightly more than 100% overlap of the detectors during a single scan. This provides slightly more than two samples per detector in the cross-scan direction, which substantially undersamples the telescope point spread function at the shorter wavelengths. Sampling rates of 16, 16, 8 and 4 samples per second of the 12, 25, 60 and 100 μm detectors, respectively, combined with the 3.85′ s^{-1} scan rate and the detector widths of 0.75′, 0.75′, 1.5′ and 3.0′, gives about a 50% oversampling in the in-scan direction. All 62 detectors did not operate correctly in orbit. Two nearly adjacent dead 25 μm detectors and one dead 60 μm detector left holes in the focal plane swath. Four noisy or partially blind detectors affected the 12 and 25 μm arrays (Figure I.B.2).

C. The IRAS Sky Survey Atlas

The *IRAS Sky Survey Atlas* is a set of machine-readable sky surface-brightness images, 12.5° × 12.5°, with 1.5′ pixels. Each image represents the sky surface brightness (minus a zodiacal emission model) at a particular IRAS wavelength within a specific field on the sky. Fields were defined by partitioning the entire sky into 430 12.5° × 12.5° regions centered every 10° along declination bands, which are spaced 10° apart. The rest of this Section summarizes the salient features in the processing of the ISSA images.

The IRAS survey array produced sky brightness measurements with higher spatial resolution in the in-scan direction than in the cross-scan direction. To reduce processing requirements, the first step in the data reduction to produce the ISSA images was to smooth and resample, at two samples per second, the time-ordered detector data streams to an in-scan resolution of 3.5′, 3.5′, 3.6′ and 4.7′ FWHM at 12, 25, 60 and 100 μm, respectively (Appendix B). Time delays were introduced independently for each detector in the smoothing and resampling process in order to rephase the data streams to sample simultaneously the same cross-scan line on the sky.

The processing removed a zodiacal emission model from the smoothed and rephased data, refined the detector zero point stability with two destriping algorithms and binned the data into images. Separate images of the individual HCONs were produced for each field and were visually examined to allow identification and removal of artifacts (§III.D.3). After removal of artifacts by editing the time-ordered data, new images were produced for each HCON and all HCONs were then co-added. Known asteroids remain in the

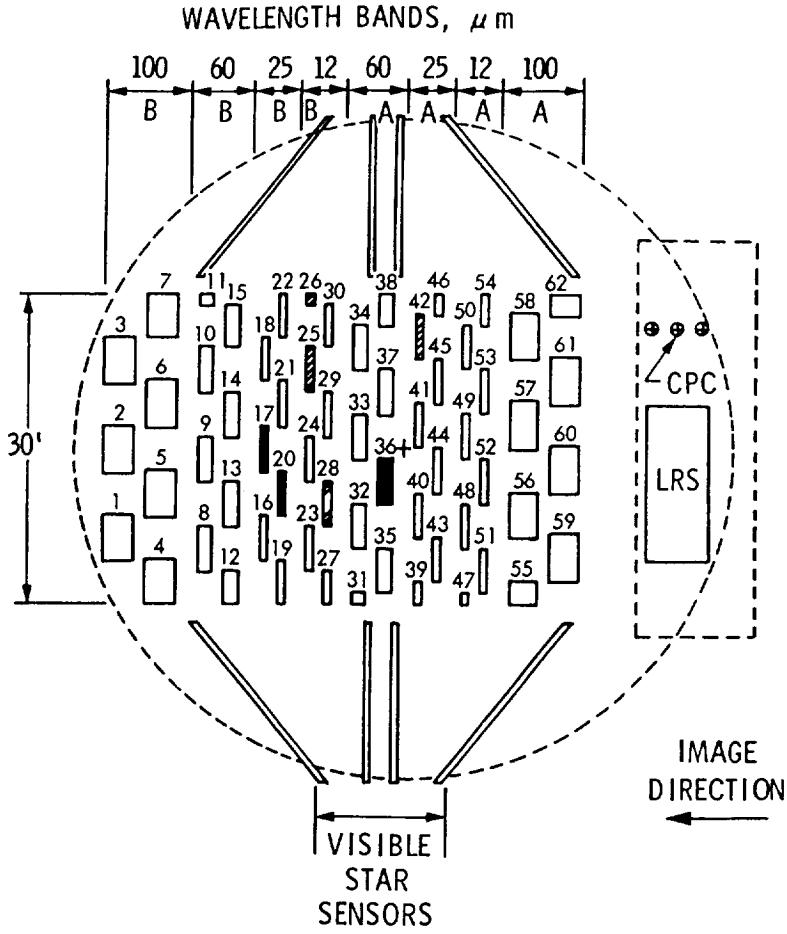

Figure I.B.2 A schematic drawing of the IRAS focal plane. The numbered rectangles in the central portion each represent the field of view of a detector, filter and field lens combination. The image of a source crossed the focal plane in the Y direction as indicated. The filled-in detectors were inoperative, while the cross-hatched detectors showed degraded performance during the mission.

---

individual HCON images but were removed from the data prior to producing the co-added images. Auxiliary images of sky coverage and statistical noise were also produced for each ISSA field. Due to volume constraints and limited utility (§III.C.4), the sky coverage and statistical noise images are not included in the released set of images. They are, however, available upon request at IPAC.

The co-added images contain some remaining features that do not confirm among the individual HCONs. These features include fine structure in the zodiacal cloud (the zodiacal dust bands, for instance), planets, unknown asteroids and orbital debris that escaped the artifact removal process. The individual HCON images enable users to identify these nonconfirming objects, both to avoid confusion with confirming sources and to study the nonconfirming sources.

D. Cautionary Notes

D.1 *Absolute Radiometry*

ISSA was designed to provide differential photometry, after removal of the zodiacal emission, over spatial scales larger than 5′. ISSA *cannot* be used for determining absolute sky surface brightness. Uncertainty of the absolute zero point is dominated at 12 and 25 μm by uncertainties in the zodiacal emission model (§III.C.2 and Appendix G) and at 60 and 100 μm (§II.B.4 and III.A.2) by imperfect knowledge of the detector offsets. All bands are affected to some extent by both of these error sources.

An uncertainty of as much as 30% at 60 μm and 60% at 100 μm exists in the frequency response correction, which affects the relative brightness measurements at spatial scales above a few degrees. Read §II.B before using ISSA images for quantitative measurements.

There is an ongoing effort with COBE scientists to understand the calibration differences between the IRAS and DIRBE data for measurements of sky brightness on large spatial scales (§IV.D.3). IPAC newsletters will contain any updated results of this work. Unless the IRAS-DIRBE comparison indicates an uncalibrated nonlinearity in the IRAS data, *the accuracy of the IRAS point source calibration is not and will not be impacted by the results of this comparison.*

D.2 *Point Source Photometry*

ISSA is designed to study extended structures in the survey data and has *not* been optimized for accuracy for sources smaller than 5′. Point sources are *not* optimally analyzed with this product. The *IRAS Point Source Catalog* Version 2, and the *IRAS Faint Source Survey* (Moshir *et al.* 1992) should be consulted for survey information on point sources. See §IV.C for discussion of expected accuracy of point sources measured with ISSA.

D.3 *Photometric Errors in Low Latitude Images, ISSA Reject Set*

The images within 20° of the ecliptic plane are of reduced quality compared to the rest of the ISSA due to contamination by zodiacal emission residuals and the zodiacal dust bands. The residual background errors at 12 and 25 μm in the reject region can be up to ten times worse than in the nonreject region. If *special* care is taken when estimating the background (§IV.F) at 12 and 25 μm, the reject images remain scientifically useful. At 60 and 100 μm, the residual background errors are smaller than at 12 and 25 μm, making the reject images especially useful at the longer wavelengths.

D.4 *Confirmation of Sources*

Due to the increased sensitivity of the ISSA images, more nonconfirming objects or anomalies are visible than in the *SkyFlux* images. Nonconfirming objects are those objects that appear in only one HCON intensity image. These objects may be orbiting satellites, asteroids or space debris. If not removed, they can appear in the co-added image. No confirmation co-adder was implemented in producing the co-added ISSA image (§III.C.4). Therefore, for each ISSA field, all individual HCON intensity images were examined visually to identify objects appearing in only one HCON image. When found,

the contaminated portion of the offending scan was identified and removed. Less than 1% of the entire survey database was removed by this visual inspection process (§III.D.3). Even though great care was taken to remove anomalies, some remain in the co-added image. Individual HCON images should be examined to verify the reality of unusual features in the co-added image.

D.5 *Solar System Debris*

Emission from some solar system material remains in the data and can cause confusion. This includes some asteroids, zodiacal dust bands, comet tails, comet trails and planets. Some asteroids remain in the co-added images since only known asteroids as of the 1986 publication of the *IRAS Asteroid and Comet Survey* (Matson 1986) were removed.

The zodiacal dust bands are seen in different aspects in different HCONS and will appear as nonconfirming extended emission bands parallel to the ecliptic plane at ecliptic latitudes less than 15°. The images affected by the dust bands are in the *ISSA Reject Set.*

Both comet tails and trails are seen in the data. Dust associated with comet tails, caused by either charged ionized particles blown by solar wind or neutral particles blown by radiation pressure, appear when the comet is closest to the sun. The tail of comet IRAS-Araki-Alcock is visible in some images near the north ecliptic pole (fields 416 and 418). Comet trails, composed of larger debris insensitive to radiation pressure, spread along the orbit of the comet and accumulate over a long period of time. In the ISSA images comet trails appear as streaks crossing the image nearly perpendicular to the scan direction. A list of ISSA fields affected by known comet trails is found in §III.C.4. Planets are also visible in ISSA fields that cover the lower latitude sky, §III.C.4.

D.6 *Residual Photon-Induced Responsivity Effects*

Artifacts resembling tails appear around point sources in the ISSA images. The tails are due to a photon-induced responsivity enhancement, or hysteresis effect, that is a function of source strength and background. Sources brighter than 15 Jy at 12 μm and 20 Jy at 25 μm are expected to have tails. Some sources at less than these thresholds may have tails. Point source tails were not removed from the data. More than one tail may radiate from a single point source in the co-added images due to point sources being scanned in several directions.

At 60 and 100 μm, hysteresis effects remain around bright areas (within $\approx 6°$) such as the Galactic plane. The effect of the photon-induced brightness around sources will change depending on the scan direction. See *Main Supplement* §IV.A.8 for explanation of photon-induced responsivity enhancement.

D.7 *Calibration Change Due to Improvements in the Accuracy of Detector Solid Angles*

Improved solid angle estimates were derived for each detector based on two-dimensional response functions (see *Explanatory Supplement to the IRAS Faint Source Survey* Version 2 1992, §II.D.2). The improved solid angles differ from those used in making the original image products, e.g., *SkyFlux* and *IRAS Zodiacal History File* (ZOHF) Version 2.0. Compared to *Main Supplement* Table IV.A.1 the average of new effective solid angles for

full size detectors increased by 13%, 8% and 6% at 12, 25 and 100 μm, respectively, and decreased by 3% at 60 μm. A change in the solid angles has an inverse effect on calculated intensity values. Therefore, the values in the ZOHF Version 3.1 will be fainter at 12, 25 and 100 μm compared to ZOHF Version 2.0 and slightly brighter at 60 μm.

D.8 *Ascending vs. Descending Scans*

Several users of the ZOHF Version 2.0 and 3.0 (§I.F and Appendix H) have found that the descending scans (scans which progress with decreasing ecliptic latitude) are systematically brighter at the ecliptic plane than the ascending scans (scans which progress with increasing ecliptic latitude). In the IRAS orbit, descending scans always look behind the Earth in its orbit while ascending scans always look ahead. The magnitude of the effect is about 2% at 12 and 60 μm, 1.5% at 25 μm, and 4% at 100 μm as seen at the north ecliptic pole between the ascending and descending scans. Analysis as described in Appendix H shows that a large part of the ascending-descending asymmetry can be attributed to uncorrected calibration drifts. However, the possibility that some small part of the asymmetry is a real feature of the sky cannot be ruled out (Dermott 1994, submitted to *Nature*).

E. Processing Caveats

E.1 *Mosaicking*

All images covering $|\beta| > 50°$ can be mosaicked without additional offset adjustments to an accuracy of about 0.1 MJy sr^{-1}. This capability is due to the use of a global destriping algorithm (§III.C.3.a), which brought all confirming coverages of the sky to a common background level.

Fields covering the lower latitude sky, $|\beta| < 50°$, were processed differently from the fields in the $|\beta| > 50°$ sky (§III.C.3.b). Fields in the lower latitude sky can be mosaicked with the same accuracy as those in the $|\beta| > 50°$ sky except near the Galactic plane and where the $|\beta| > 50°$ sky and $|\beta| < 50°$ sky join. At these two locations, ISSA field boundary discrepancies of 1–2 MJy sr^{-1} at 60 μm and 3–5 MJy sr^{-1} at 100 μm are measurable.

E.2 *Saturated Data*

An error was found in the algorithm for handling saturated intensity values. The error eliminated the wrong detector when saturation occurred and affects the *SkyFlux* images as well as the entire set of ISSA images. As a result, saturated intensity values were included in the images while some nonsaturated intensity values were erroneously eliminated. This effect occurs mainly in the Galactic plane where the 60 and 100 μm detectors saturate, but it is not considered a significant problem since it affects less than 0.1% of detector data (§III.D.4.b).

E.3 *Destriper Anomalies*

An error was found in the software that derived the parameters for one of the destriper algorithms implemented for ISSA, resulting in poor corrections for some scans in the $|\beta| > 50°$ sky. This error affects less than 1% of the data. Although destriper problems were removed in the quality checking process (§III.D), some destriper anomalies remain in the $|\beta| > 50°$ images. A typical destriper anomaly is visible at 4h31m46.5s:-63d40m15s (ISSA field 13). The magnitude of the effect at this location is about 0.5 MJy sr^{-1} at 12 and 25 μm. Typically the anomaly is very short, less than 0.5°. The software was fixed for processing the $|\beta| < 50°$ sky.

E.4 *Low Spatial Frequency Artifacts*

Residual zodiacal emission effects remain in the ISSA images due to imperfections in the zodiacal model. This is seen as either sharp discontinuities or gradients in the ISSA images. Discontinuities occur where adjacent regions of the sky were observed through a different part of the zodiacal dust cloud. An example of a discontinuity occurs at 12 and 25 μm around 60° and 240° ecliptic longitude. This is referred to as the mission overlap discontinuity. The 60° point marks the beginning of the descending leg and the 240° point marks the beginning of the ascending leg of the HCON-1 and HCON-2 survey. Six months later the descending leg had progressed to the 240° point and the ascending leg to the 60° point. Thus the same part of the sky was viewed six months later through a different part of the zodiacal dust cloud. The peak magnitude of the change in the intensity along this longitude occurs at $-15°$ ecliptic latitude, where the discrepancy is enhanced by a geometric effect caused by looking through a zodiacal dust band at a different time of year. The change in intensity is roughly 2.0 MJy sr^{-1} at 12 μm, which is about 7% of the local intensity prior to zodiacal emission removal. For $|\beta| > 50°$, the worst discrepancy at 12 μm is roughly 5% of local intensity prior to zodiacal emission removal and about 2% at 25 μm.

In addition to discontinuities, other large angular scale artifacts not attributable to the Galaxy remain in the images. These are due to differences between the zodiacal emission and the zodiacal model used in producing the ISSA (§IV.E.3).

F. The IRAS Zodiacal History File

The same resampled and rephased time-ordered data described in §I.C were used to produce the *IRAS Zodiacal History File* (ZOHF) Version 3.0, released in December 1988, and all subsequent versions. The ZOHF is a time-ordered record of the entire IRAS survey in which all detectors in each band of the survey array have been added together over eight-second intervals to produce a $0.5° \times 0.5°$ beam. An important difference between the ZOHF and the ISSA images is that the ZOHF retains the zodiacal dust emission as observed during the IRAS survey. For additional information on the ZOHF refer to Appendix H.

Version 3.1 of the standard ZOHF was released in May 1990 and corrected a single error found in Version 3.0. The problem affected the intensities of a very small number

of ZOHF samples in Version 3.0: none at 12 μm, one at 25 μm, one at 60 μm and 382 (0.03%) at 100 μm. The affected samples were lowered 23% on the average, with a maximum decrease of 45%. The description and analyses presented in the IRAS circular accompanying Version 3.0 and in Appendix H of this Supplement are not changed by this correction.

The ZOHF is also available with the zodiacal emission removed. This product was made by subtracting the zodiacal emission as predicted by the J. Good model (Appendix G). The Zodiacal Emission Removed ZOHF is available from IPAC by special request.

In response to requests by IPAC General Investigators, two additional versions of the ZOHF were produced and released by IPAC. A version of the ZOHF was generated giving each pixel the maximum in-scan resolution of 2′ while maintaining the 0.5° resolution cross-scan. This product is known as the 2′ In-scan ZOHF and was produced for the purpose of studying the zodiacal dust bands near the ecliptic plane. The Bright Point Source Removed (BPSR) ZOHF was produced in response to a user request and was generated by removing flux contribution due to bright point sources and associated tails. Point sources were identified using the IRAS Point Source Catalog. Detector samples within a 10′ radius of the known source and along the source tail were removed from the scan data prior to computing an eight-second intensity average. Under certain conditions this algorithm produced a nonphysical increase in a 0.5° × 0.5° pixel brightness compared to the brightness in the ZOHF Version 3.0. This can occur in areas where sources are fainter than surrounding structure. Due to this discrepancy, *IPAC recommends that special care be taken when using the* BPSR ZOHF.

All released ZOHF products as well as the ISSA are available through:

Coordinated Request and User Support Office (CRUSO)
NASA/GSFC
Code 633.4
Greenbelt, MD 20771.

II. IRAS SKY SURVEY ATLAS OVERVIEW

A. Changes and Improvements in Atlas

The processing that created the ISSA images was designed to correct several problems that limited the sensitivity and usability of the *SkyFlux* images. These problems include the effects of the photon-induced responsivity enhancement (*Main Supplement* §IV.A.8), also known as hysteresis, which degraded photometric accuracy around bright regions such as the Galactic plane at 60 and 100 μm; variations in detector responsivity and electronic offsets that produced prominent striping in the *SkyFlux* images; and spatial and temporal variations of the observed zodiacal foreground producing steep, artificial gradients in the *SkyFlux* images, which obscured faint sky features and prevented co-addition of the individual HCON images. Finally, the 2′ pixels of the *SkyFlux* images just critically sampled the resolution of the time-ordered detector data for the 12, 25 and 60 μm bands, making interpretation difficult without further interpolation.

The combination of all improvements reduced the residual stripes to the level of the intrinsic detector noise and largely eliminated interference from the zodiacal foreground. The removal of the zodiacal foreground emission increased the sensitivity over the *SkyFlux* images by roughly a factor of five. The destripers reduced the detector-to-detector noise by factors of 2–3 at 12 and 25 μm and 1.5–2.0 for 60 and 100 μm. This results in images with similar noise in the in-scan and cross-scan directions. Coaddition provides an additional factor of $\sqrt{3}$ improvement over individual HCON images. The co-added images reveal faint structure at 12, 25 and 60 μm totally invisible in the *SkyFlux* images. Details of the quality of the ISSA images will be found in Chapter IV.

A.1 *Improvements in Relative Calibration*

When looking at uniform sky, equal-sized detectors within a band will give different measurements due to variations in detector baselines and responsivities. With perfect calibration, these variations are removed and images of the sky appear uniform. Any imperfections in calibration result in detector-to-detector striping in the images. Calibration enhancements for ISSA, described in §III.A.2, reduced the detector-to-detector stripes by roughly a factor of ten at 12 and 25 μm relative to the calibration used in the *SkyFlux* images. *No calibration changes have affected the IRAS point source calibration.*

A.2 *Zodiacal Foreground Removal to Permit Coaddition*

A foreground predicted by the zodiacal emission model described in §III.C.2 and Appendix G was removed from the time-ordered detector data, permitting useful co-addition of the individual HCON images. The subtraction of the zodiacal model resulted in a five-fold or better reduction, compared to the non-zodiacal-removed data, in gradients and artifacts due to changes in zodiacal foreground during the IRAS survey. However, some effects of the zodiacal foreground remain in the data. Since the zodiacal emission model is not perfect, insufficient foreground was removed in some places and too much was removed in others. Residual foreground removal errors for $|\beta| > 50°$ are 3–5% of the original background, 0.5 MJy sr^{-1} at 12 μm and 1.0 MJy sr^{-1} at 25 μm over scales of 10°. For

$50° > |\beta| > 20°$, the residuals are 1.0 MJy sr^{-1} at 12 μm and 2.0-2.5 MJy sr^{-1}at 25 μm over scales of 10°.

The zodiacal emission model assumed a physical dust distribution which did *not* include the dust bands. The dust band emission remains in the data and produces artifacts in the images at low ecliptic latitudes, the *ISSA Reject Set*.

A.3 *Destripers to Stabilize Detector Baselines*

Stripe noise due to residual baseline fluctuations, residual zodiacal foreground and uncalibrated responsivity variations was reduced with two destripers. The first destriper globally compared all of the survey data at 1.2 million points on the sky (Emerson and Gräves 1988). At each point, the global destriper attempted to match each detector to the average of all other detectors in the same wavelength. This was accomplished by applying a slowly varying baseline correction to every scan of every detector. The assumption of global destriping is that the average of all IRAS measurements, after zodiacal foreground removal, of a particular point on the sky is the best estimate for the brightness at that point. The second destriper, known as the local destriper, used a similar comparison of each detector to the average of all detectors to make further baseline adjustments. This destriper used only the data in a single 12.5° field. The local destriper was able to accomplish about a 10% reduction in cross-scan RMS left after global destriping. The two destripers are described in §III.C.3.

A.4 *Oversampling to Improve the Representation of Spatial Information*

The 1.5′ pixel spacing in the ISSA images improves the sampling interval by 25% over the *SkyFlux* images and obviates the need to further smooth the time-ordered data.

A.5 *Improved Pointing Information*

Improvements in the pointing reconstruction for the IRAS survey contribute slightly to improved resolution in the ISSA images (§III.A.1).

A.6 *Particle Radiation Removal*

Signal processing on board the IRAS satellite attempted to remove from the IRAS detector data noise spikes due to high-energy protons and electrons. However, many small spikes and vestiges of large spikes remained in the *SkyFlux* images. A deglitcher removed this noise from the ISSA images (§III.A.3).

A.7 *Known Asteroid Removal from the Coadded Images*

Known asteroids listed in the *IRAS Asteroid and Comet Survey* (Matson 1986) were removed from the data prior to making the co-added images. This eliminated a major contributor of nonconfirming sources (§III.C.4) in the co-added images. Asteroids remain in the individual HCON images.

A.8 *Full-Sized Detectors*

When flux measurements are converted to surface brightness, point sources measured by undersized detectors appear too bright. Thus, to eliminate photometric problems associated with combining different detector sizes, only the operative, full-sized detectors (Table II.A.1) were used in making the ISSA images. The *SkyFlux* images used $\frac{3}{4}$-sized as well as full-sized detectors.

Table II.A.1
Detectors Used in IRAS Sky Survey Atlas Images

Wavelength (μm)	Detectors												
12	23	24	25	28	29	30	48	49	50	51	52	53	
25	16	18	19	21	22	40	41	42	43	44	45		
60	08	09	10	13	14	15	32	33	34	35	37		
100	01	02	03	04	05	06	07	56	57	58	59	60	61

B. Overview of Calibration

B.1 *Point Source Calibration Method*

The brightness scale of the IRAS detectors was set in a three-step process. First, the point source calibration of the 12 μm IRAS survey detectors was tied to the ground-based 10 μm absolute calibration by Rieke *et al.* (1984) via measurements of α Tau. This calibration was extrapolated to 25 and 60 μm using stellar models. The extrapolation from 60 to 100 μm was based on observations and model calculations of asteroids. Details of this process are presented in Chapter VI of the *Main Supplement*. *No changes have been made to the IRAS absolute point source calibration for* ISSA.

Calibration was then transferred to a secondary standard, NGC6543, and internal stimulators were used for short-term maintenance of the point source calibration. Details of this process are found in Chapter VI of the *Main Supplement*. A model was used to track the point source responsivity of the detectors between internal stimulators. A number of improvements to this model were made and are detailed in §III.A.2.

B.2 *Spatial Frequency Response*

As mentioned above, the IRAS detector responsivities were monitored by the use of internal stimulators, which were flashed for a duration similar to that of a point source scanning across a detector at the survey rate. These flashes were calibrated to NGC6543 as discussed in Chapter VI of the *Main Supplement*. All data were scaled relative to the response to the flashes, thus accurately calibrating data to the point source frequency.

Longer exposure to point sources revealed a difference between the short term (AC) and long term (DC) responsivity of the detectors, suggesting that a correction to the point source calibration was needed for extended source photometry. This correction was

obtained by measuring detector response as a function of dwell time during the IRAS mission in an attempt to define the frequency response of the IRAS detectors. Point sources were scanned across the detectors at $\frac{1}{2}$, $\frac{1}{4}$, $\frac{1}{8}$ and $\frac{1}{16}$ of the survey scan rate. Measurements were extended to longer periods, with flashes of the internal stimulators lasting tens of seconds for 12 and 25 μm and by extended stares at point sources for 60 and 100 μm. Some of these measurements are shown in Figures II.B.1(a)–(c), which is reproduced from Figure IV.A.4 of the *Main Supplement*. The temporal response shown in Figures II.B.1(a)–(c) is translated into a spatial frequency response using the IRAS survey scan rate of $3.85'\ s^{-1}$.

No attempt was made to perform a true frequency response correction for the ISSA data. Instead, the point source calibration was multiplied by a single factor in each band in order to best represent the surface brightness at large spatial scales ($> 2°$ at 12 and 25 μm and $> 5°$ at 60 and 100 μm). The factors were 0.78, 0.82, 0.92 and 1.00 at 12, 25, 60 and 100 μm, respectively. ISSA and the ZOHF products are therefore DC calibrated. To recover the correct brightness on the smallest spatial scales (point sources), the inverse of these factors should be applied to the total flux measured. The correction factors for intermediate spatial scales can be determined for 12 and 25 μm from Figure II.B.1(a). Suggested corrections for 12 and 25 μm are found in Table II.B.1.

Table II.B.1

Suggested Correction Factors for Spatial Frequencies Between $6'$ and $2°$ at 12 and 25 μm

Spatial Scale (deg)	Multiplication Factors*	
	12 μm	25 μm
0.1	1.15	1.10
0.2	1.18	1.13
0.5	1.25	1.18
1.0	1.28	1.20
1.5	1.28	1.23
2.0	1.28	1.23

* Multiplication factors to recover small-scale photometry from the ISSA data.

While the frequency response of the detectors at 12 and 25 μm was clear, no consistent measurement was obtained for 60 and 100 μm. Figures II.B.1(b) and II.B.1(c) suggest a nonlinearity which makes the frequency response at 60 and 100 μm dependent on brightness. The uncertainty in the overall linearity of the photometric scale at the long wavelengths results in photometric uncertainties of about 30% and 60% for extended sources at 60 μm and 100 μm, respectively.

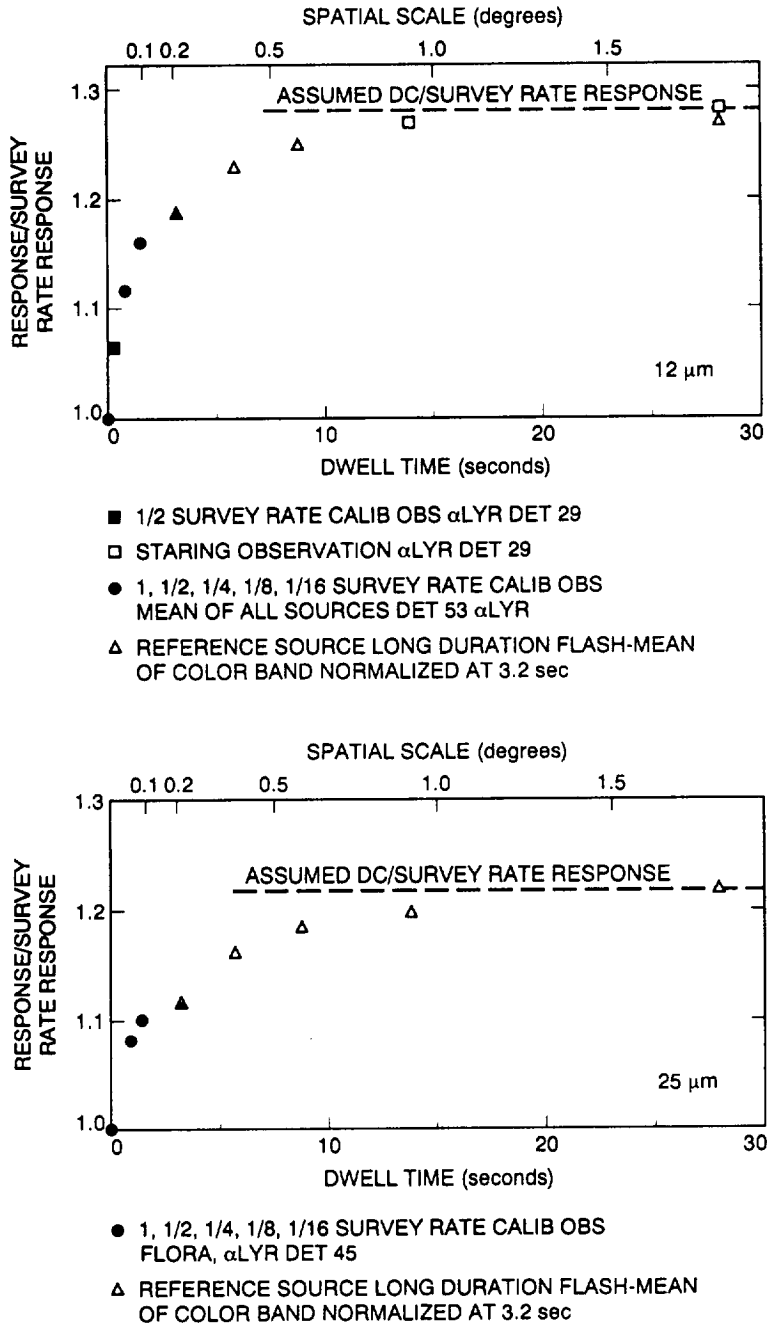

Figure II.B.1(a) Measurements of the response vs. dwell time to measure frequency dependence of the detectors at 12 (top panel) and 25 (bottom panel) μm. The measurements were made either by crossing a source at scan rates less than the survey rates or by viewing long flashes of the internal reference source. The upper horizontal scale has translated the dwell time of the lower scale to spatial frequency using the IRAS survey scan rate of $3.85' \text{ s}^{-1}$.

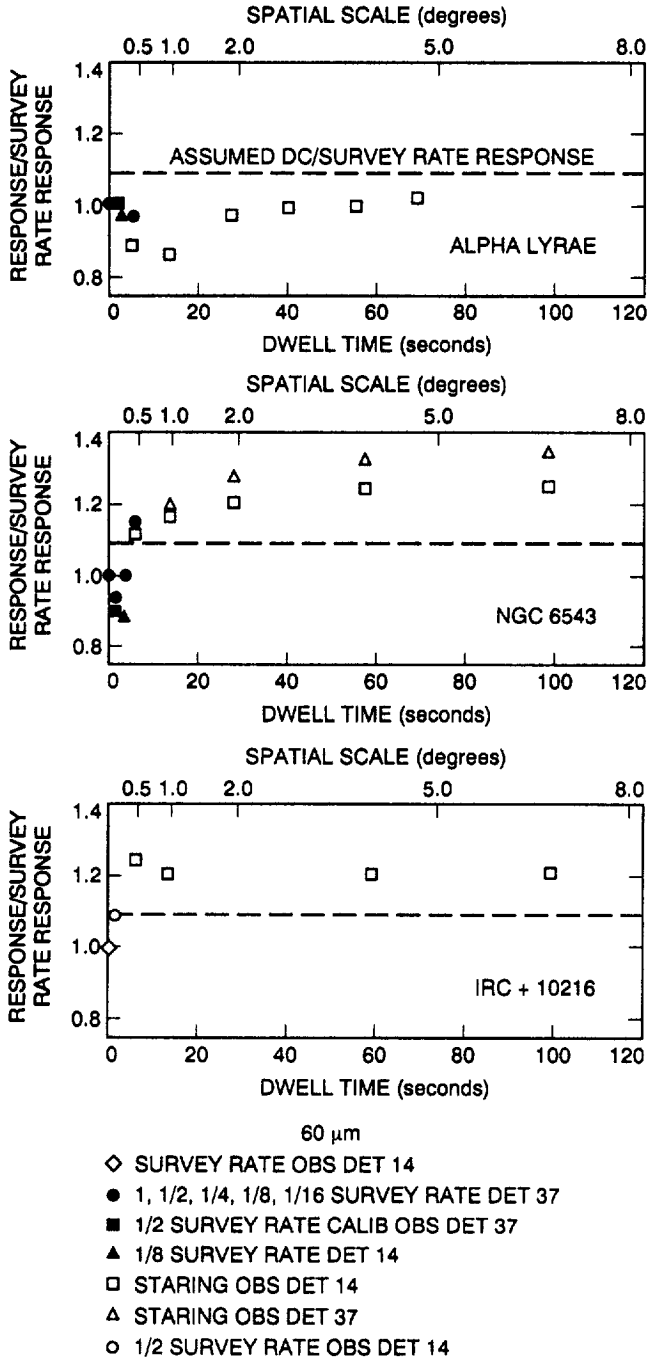

Figure II.B.1(b) Measurements of the response vs. dwell time to measure frequency dependence of the detectors at 60 μm. The measurements were made either by crossing a source at scan rates less than the survey rates or by viewing long flashes of the internal reference source. The upper horizontal scale has translated the dwell time of the lower scale to spatial frequency using the IRAS survey scan rate of $3.85' \text{ s}^{-1}$.

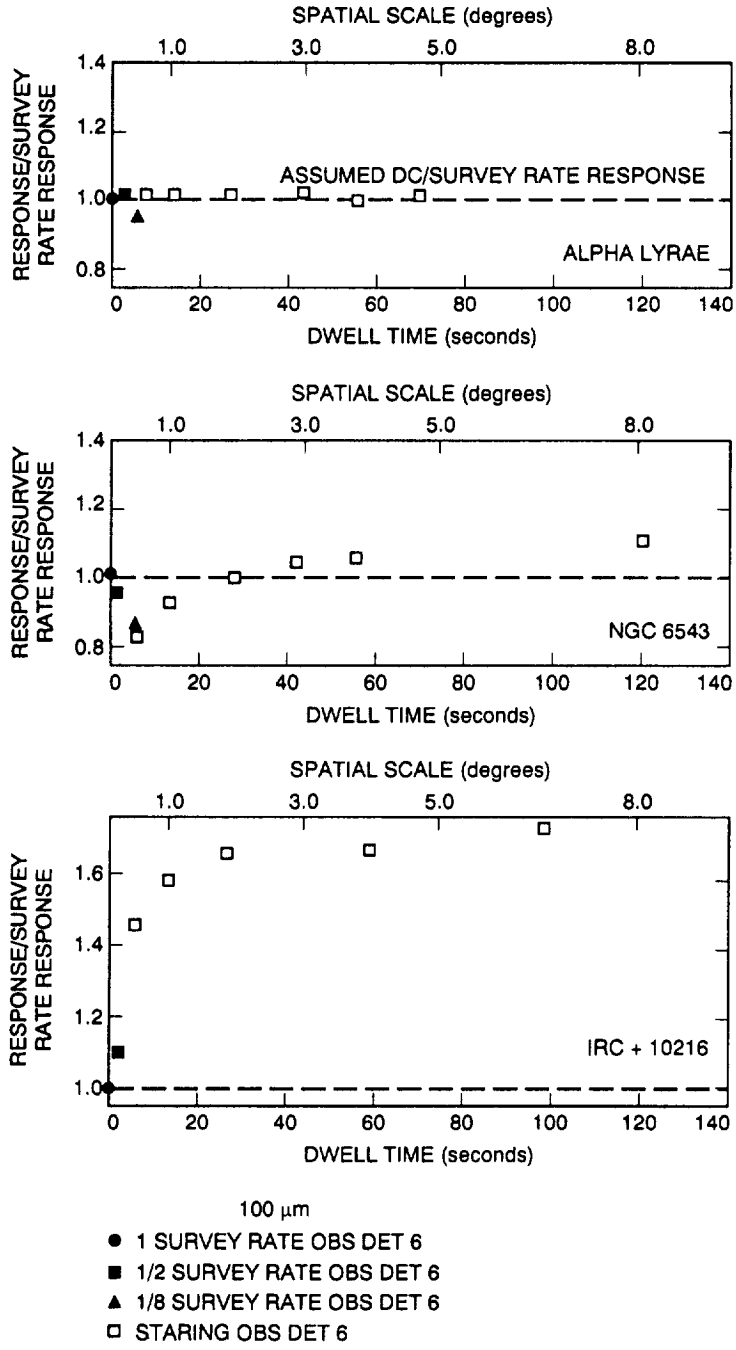

Figure II.B.1(c) Measurements of the response vs. dwell time to measure frequency dependence of the detectors at 100 μm. The measurements were made either by crossing a source at scan rates less than the survey rates or by viewing long flashes of the internal reference source. The upper horizontal scale has translated the dwell time of the lower scale to spatial frequency using the IRAS survey scan rate of $3.85' \text{ s}^{-1}$.

B.3 *Detector Effective Solid Angles*

After the data were corrected for frequency response of the detectors and their electronics as discussed in §II.B.2, the effective solid angle of each detector was used to yield the average surface brightness over the field of view (*Main Supplement* §IV.A.3). The solid angle values used for ISSA have improved since the *SkyFlux* release in 1986 and are discussed in §II.D.2 of the *Explanatory Supplement to the Faint Source Survey*. The magnitude of the difference is given in §III.A.2.c.

B.4 *Zero Point Calibration*

The zero point of the IRAS calibration was set and maintained by reference to an area of sky free from point sources near the north ecliptic pole and NGC6543 (the secondary calibration standard *Main Supplement* §*VI.B*), which was accessible throughout the entire IRAS mission. This area was called the Total Flux Photometric Reference or TFPR. The TFPR was observed daily using the special calibration observation CS-15. The total signal from each detector was compared to the brightness model for the TFPR (§III.A.2.b) and the difference between the measured and predicted electrical signal was ascribed to the electronic offset. The value of the electronic offset used for correction of the zero point in survey observations was obtained by linear interpolation between offsets obtained during these measurements of the TFPR. This process is described in more detail in §VI.B.3 of the *Main Supplement*. The accuracy of the IRAS zero point is dependent on the accuracy of the TFPR brightness prediction (§III.A.2.b).

The TFPR model was derived based on a TFPR position of $\beta = 89.2°$ and $\lambda = 94.6°$ where β and λ represent ecliptic latitude and ecliptic longitude, respectively. However, due to the method by which the CS-15 calibration observations were executed, the actual position observed as the TFPR varied slightly throughout the mission. The observed position of the TFPR varied between $\beta = 88.8°$, $\lambda = 268.9°$ and $\beta = 89.2°$, $\lambda = 95.0°$ depending on the scan direction past NGC6543 at $\beta = 89.8°$, $\lambda = 150.3°$. NGC6543 was used in the point source calibration as a secondary transfer standard (*Main Supplement* §VI.B). Although this caused discrepancies in the derived offsets, it is not considered a major source of error. The variation in flux among the TFPR locations is roughly 0.03%, 0.5%, 0.2% and 1.9% at 12, 25, 60 and 100 μm, respectively, of the absolute zero point as assumed by the TFPR model, §III.A.2.b.

B.5 *Calibration Limitations for Extended Sources*

The zero point calibration was severely limited by our knowledge of the absolute flux and the annual variation of the TFPR. This is not a major problem since the ISSA images are not intended to provide accurate absolute photometry. Uncertainties for the TFPR model are found in §III.A.2.

As discussed in §II.B.2, the IRAS scan data were not corrected for all spatial frequencies. Features in the ISSA with spatial scales less than 2° at 12 and 25 μm and less than 5° at 60 and 100 μm appear too faint. The correction factors for point sources are given in §II.B.2. Suggested correction factors for intermediate spatial scales are found in Table

II.B.1. Large uncertainties, 30% and 60% at 60 and 100 μm, respectively, exist in the factors for spatial scale corrections. This uncertainty in the frequency response of IRAS at long wavelengths is the major source of uncertainties in the absolute calibration of ISSA. The user is directed to a careful reading of §II.B.2 and examination of Figures II.B.1(b) and (c) before attempting to perform photometric corrections for spatial scales at 60 and 100 μm.

C. Product Description

ISSA, combined with the *ISSA Reject Set*, is a set of 430 machine-readable images in Flexible Image Transport System (FITS) format (Wells *et al.* 1981). Each image consists of 500 × 500 pixels covering a 12.5° × 12.5° field of sky with a pixel size of 1.5′. The fields are along declination bands which are spaced 10° apart. In right ascension, the spacing varies due to convergence at the poles. Field numbering starts at the south equatorial pole as shown in Figures II.C.1 – II.C.3. *Note that the numbering scheme is different from the SkyFlux fields*. Appendix A lists the entire ISSA and *ISSA Reject Set* with corresponding field centers.

For each field and IRAS wavelength (12, 25, 60 and 100 μm), there is an intensity image for each confirming coverage (HCON-1, HCON-2 and HCON-3) plus a co-added image of all the coverages. Coverage and standard deviation images were also produced and are available upon request at IPAC.

The FITS intensity images are either 16 or 32 bits per sample. The number of bits per sample was determined by examining the intensity range and comparing it to 5% of median noise, where noise is the standard deviation of the mean of each pixel. If 16 bits is too small to hold the intensity range down to the 5% of median noise level, then the number of bits that will carry information down to that threshold is used. In FITS-formatted images, any number greater than 16 bits requires 32 bits per sample.

The size of each intensity image is either 0.5 or 1.0 Mbytes, depending on noise level and dynamic range of signal. The entire set of ISSA plus *ISSA Reject* images has a size of 4.2 Gbytes. The *ISSA Reject Set* comprises about 1.4 Gbytes.

ISSA is available through:

Coordinated Request and User Support Office (CRUSO)
NASA/GSFC
Code 633.4
Greenbelt, MD 20771.

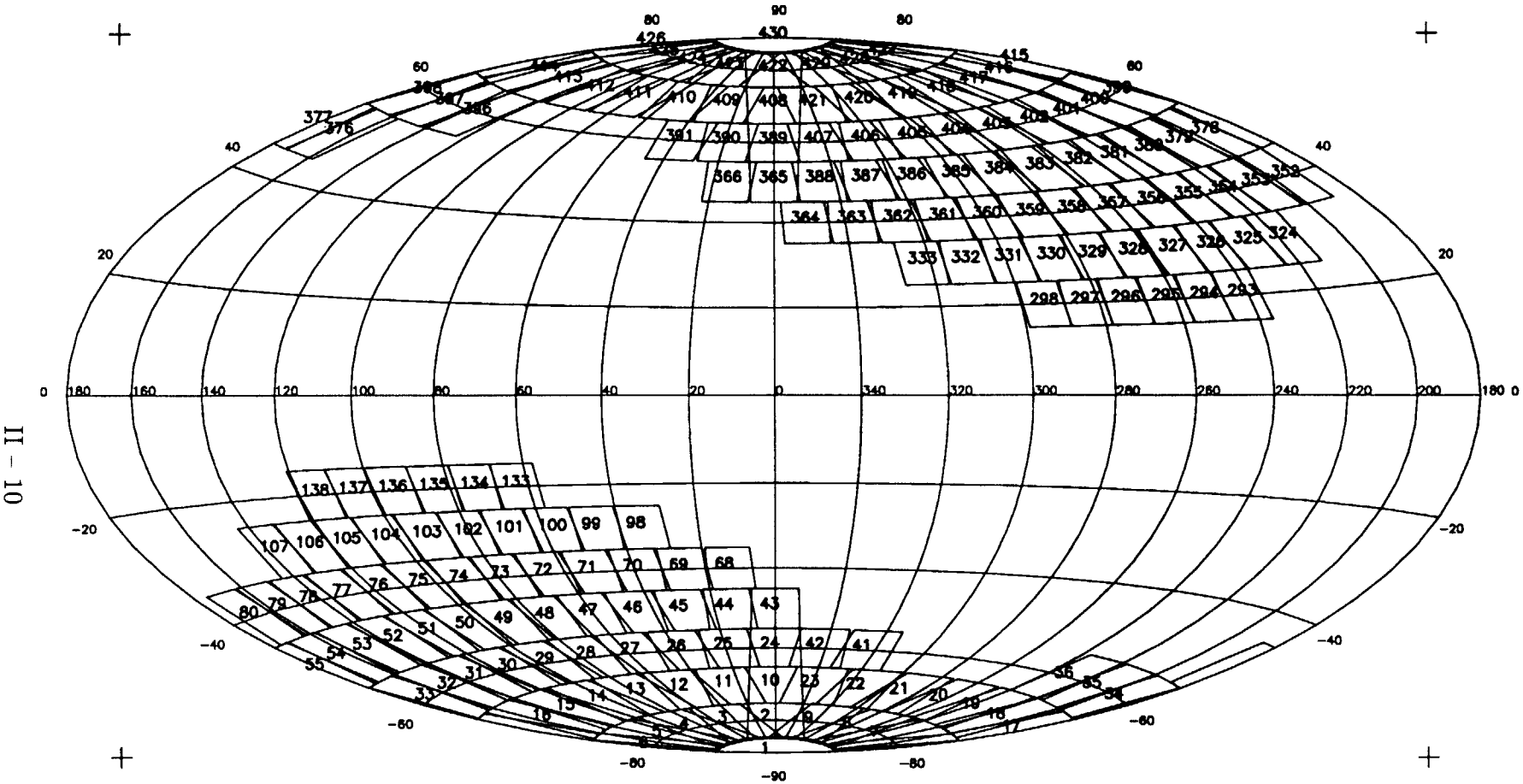

Figure II.C.1 ISSA Fields for $|\beta| > 50°$ in Equatorial Coordinates

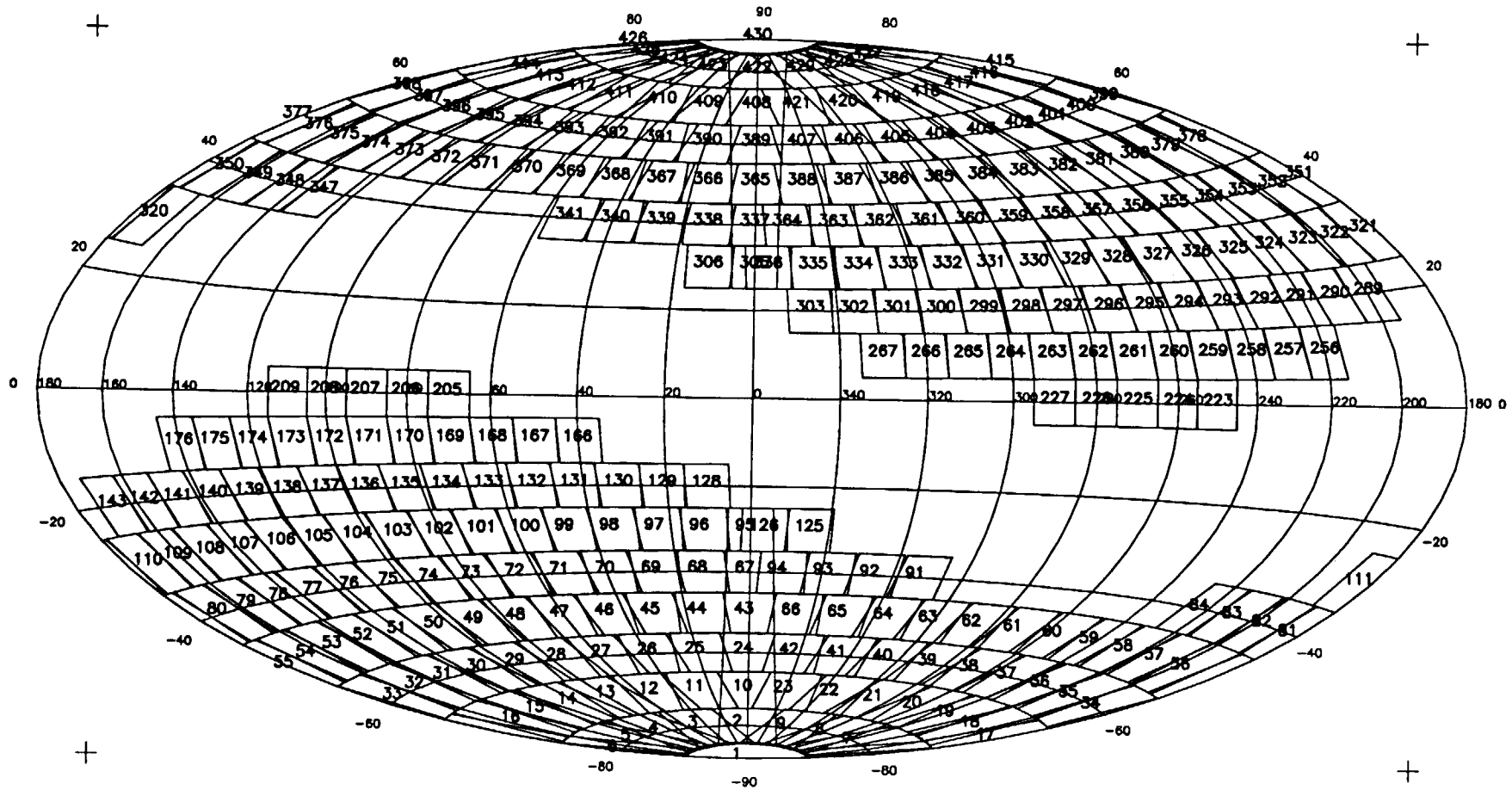

Figure II.C.2 ISSA Fields for $|\beta| > 20°$ in Equatorial Coordinates

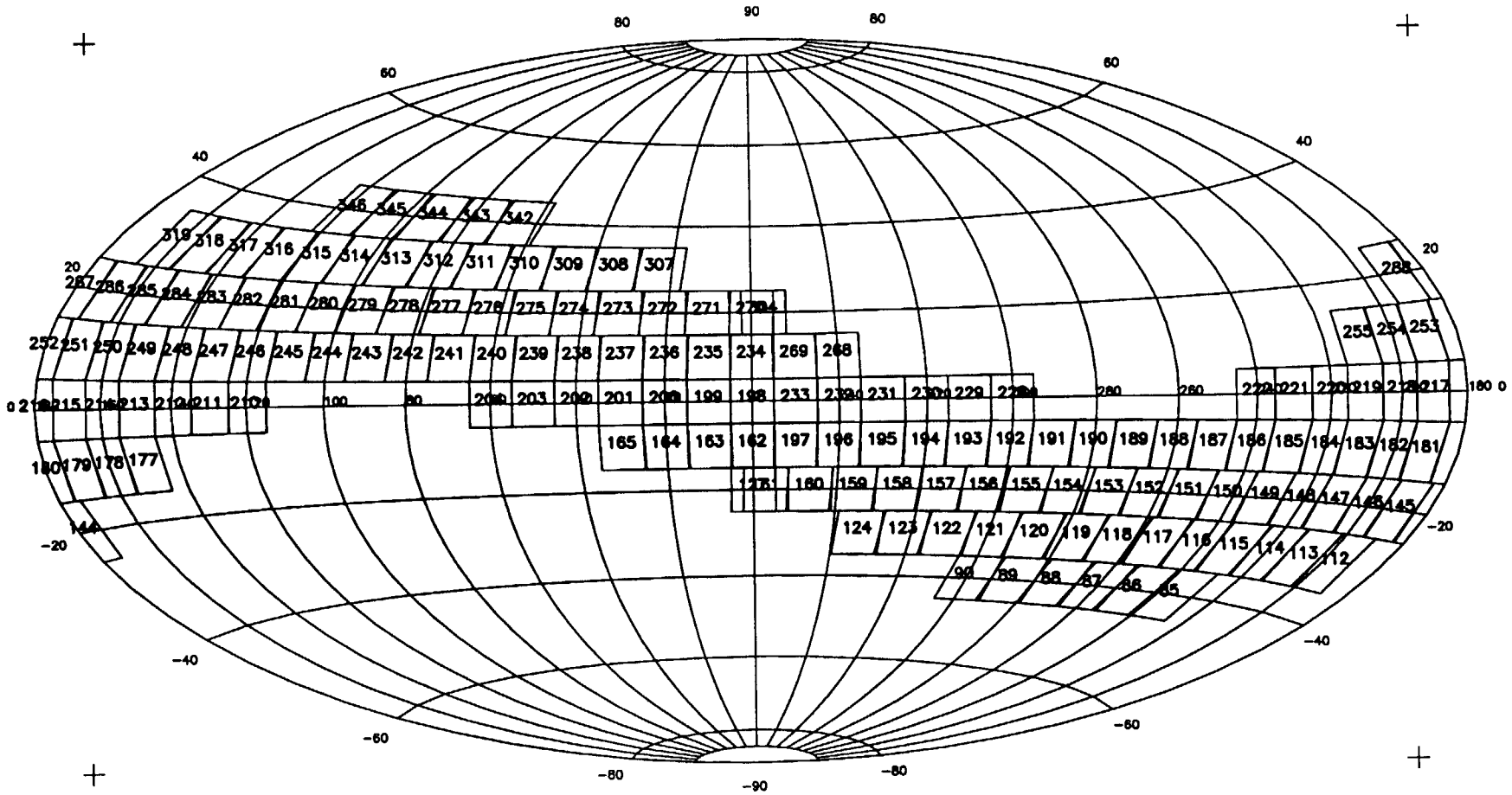

Figure II.C.3 ISSA Reject Fields $|\beta| < 20°$ in Equatorial Coordinates

III. PROCESSING

The production of the ISSA images involved three major processing steps. First, the entire IRAS survey detector data were reprocessed using improved pointing reconstruction and calibration algorithms, §III.A. The time-ordered detector data were then reorganized according to celestial position, §III.B. Finally, the images were produced after removing the zodiacal foreground and destriping, §III.C.

A. Time-Ordered Detector Data Improvements

The ISSA images, like the *SkyFlux* images (*Main Supplement* §V.G), were made from in-scan, time-ordered detector data that were calibrated, positionally phased, compressed, position-tagged, filtered and resampled. The compressed, time-ordered database used by ISSA incorporates improved boresight and calibration information. In addition, radiation hits were removed from the time-ordered data used in making the ISSA. These improvements are discussed below.

Time-ordered detector data were smoothed using the same algorithm as described in the *Main Supplement*, §V.G for *SkyFlux*. This algorithm smoothed and resampled the IRAS detector data from 16, 16, 8 and 4 samples per second at 12, 25, 60 and 100 μm, respectively, to two samples per second at each wavelength. Additional information is found in Appendix B of this Supplement.

A.1 *Positional Improvements*

Positional calculations were improved since the *SkyFlux* processing by the following corrections and modifications. Most important was the correction of an error that advanced the in-scan position by 115″ for half the mission data. This error was found in the *SkyFlux* images and the ZOHF Version 2.0. No other data products were affected. A second improvement was in the data phasing. Phasing is the process by which the individual detector data streams are realigned with respect to each other to bring together samples taken at the same in-scan sky position. The satellite scan rate used for this process was changed from the initial scan rate of an observation to its average rate. A third improvement involved implementation of a new algorithm for the position computation. The cumulative effect of the position corrections and improved interpolation scheme is quantified for the ZOHF in Appendix H, Table H.4.

Although pointing reconstruction errors were a relatively small contributor to the original position errors, improvements in the satellite pointing reconstruction made to support the *IRAS Faint Source Survey* were also incorporated in the time-ordered detector data (*Explanatory Supplement to the IRAS Faint Source Survey*, §II.B). In general, pointing reconstruction improvements reduced the in-scan 1-σ boresight uncertainties from 3.0″ to 1.5″ and the cross-scan 1-σ from 4.5″ to 3.0″. In addition, many scans that had anomalously bad pointing were improved to bring them to the same accuracy as the other scans.

A.2 *Calibration Improvements*

Several important changes were made in the IRAS calibration software. An improved model of the detector response function that corrects the first-order effects of the radiation-induced and photon-induced responsivity enhancement was implemented. Improvements were made to the model of the Total Flux Photometric Reference (TFPR), which was used in maintaining the zero point of the IRAS detectors. Improved estimates of the solid angles of the detector fields of view were used and the measurement of the internal reference source was derived using a more robust algorithm. In addition, an empirical method for reducing scan-to-scan variations was implemented at 25 μm (§III.C.1).

A.2.a *Detector Response Function*

The response of each detector was known to be enhanced due to radiation and photon exposure (*Main Supplement* §VI.B.4). This responsivity enhancement is referred to as the hysteresis effect. A response function for each detector was implemented that models hysteresis at the point source frequency. The model corrects all detectors for radiation-induced responsivity enhancement due to the South Atlantic Anomaly (SAA) and the 60 and 100 μm detectors for photon-induced responsivity enhancement. At 12 and 25 μm, the photon-induced responsivity enhancement that created the point source tail artifacts was not removed by this model. Point source tails remain in the data.

The parameters for the hysteresis model were derived based on the history of the point source responsivity as measured by the internal reference source after SAA crossings and Galactic plane crossings. The internal reference source was used at the beginning and end of each survey scan to monitor the point source responsivity of the system. A history was kept of the point source responsivity for each detector throughout the mission. From this history, the responsivity measurements were sorted and organized based on time from SAA crossing and again based on time from Galactic plane crossing. These two different datasets were used in deriving time constants for each detector to represent the exponential decay of the responsivity after particle radiation or photon exposure. The hysteresis formula is given in Table III.A.1. The detector response due to photon exposure as shown in the equation is $\Delta R(t)$ and is only applicable to the 60 and 100 μm detectors. For the 12 and 25 μm detectors the value of $\Delta R(t)$ is zero. The derived detector time constants are listed in Tables III.A.2(a)–(d). The improvement at 100 μm in tracking the point source responsivity is seen in Figure III.A.1. This figure shows the average percent difference within a $5° \times 10°$ bin in the point source fluxes as measured from ascending and descending scans along ecliptic longitude 270°. At this longitude the Galactic plane is crossed around $-15°$ ecliptic latitude. For this set of point sources, the original uncorrected response function resulted in the ascending scans overestimating the point source flux values after the Galactic plane crossing by 10%–15% compared to the descending scans (solid line). The hysteresis-corrected point source fluxes (broken line) show a reduced effect across the Galactic plane. Discrepancies on the order of 6% RMS remain.

Table III.A.1
Hysteresis Equation

$$R(t) = \left[A + B \cdot e^{-\frac{t}{\tau_B}}\right] / \left[1 - \Delta R(t)\right] \qquad \text{for } T_1 < t < T_2$$

$$A = R(T_1) - \left[R(T_1) * \Delta R(t)\right] - B \cdot e^{-\frac{T_1}{\tau_B}}$$

$$B \cdot e^{-\frac{t}{\tau_B}} = \frac{e^{-(t-T_1)/\tau_B}}{1 - e^{-(T_2-T_1)/\tau_B}} \left[\Big(R(T_1) - \big(R(T_1) \cdot \Delta R(T_1)\big)\Big) - \Big(R(T_2) - \big(R(T_2) \cdot \Delta R(T_2)\big)\Big)\right]$$

$$\Delta R(t) = \min\left(\Delta R(t-\Delta) * e^{\Delta/\tau_p} + K \cdot F_{\text{int}}(t-\Delta), \Delta R_{\max}\right)$$

$$K \cdot F_{\text{int}}(t-\Delta) = K \cdot F_{\text{int}}(t-\Delta) \quad \text{if } F_{\text{int}}(t-\Delta) \geq \text{Threshold}$$
$$= 0 \quad \text{if } F_{\text{int}}(t-\Delta) < \text{Threshold}$$

R = total detector response
ΔR = detector response due to photon exposure
τ_B = bias boost time constant
τ_p = photon exposure time constant
K = max %/saturation (Joules)
F_{int} = integrated flux over time interval Δ measured in Joules
Δ = delta time
t = time from last bias boost
T_1 = time of first internal stimulator
T_2 = time of second internal stimulator

Detector responsivity is a function of spatial frequency. Although the hysteresis model was derived from data taken with the internal stimulators, which measure the point source or AC frequency response, it was assumed that this model would represent the hysteresis effect at all spatial scales. Only the factors discussed in §II.B.2 were used to scale the point source responsivity to an extended emission responsivity prior to producing the ZOHF and ISSA products. To verify that the hysteresis model was effective for extended spatial scales, ascending and descending scans (before and after hysteresis correction) in the 0.5° ZOHF were compared. The result of this comparison showed the same hysteresis effect existed for extended spatial scales at 60 and 100 μm as for point sources. After hysteresis corrections were applied at 60 and 100 μm, a 5%–6% discrepancy remains between 6° and 15° of the Galactic plane. Larger uncertainties still occur within 6° of the plane.

A.2.b *Zero Point Calibration*

The detector calibrated zero points were maintained by daily reference to a patch of sky of measured brightness near the north ecliptic pole called the Total Flux Photometric

Table III.A.2(a)
Time Constants, 12 μm

Detector #	Tau for Bias Boost (sec)
23	1200
24	1200
25	1200
26	1200
27	1200
28	1200
29	1200
30	1200
47	1200
48	1200
49	1200
50	1200
51	1200
52	1200
53	1200
54	1200
Mean Time Constant	1200
Standard Deviation	0

Table III.A.2(b)
Time Constants, 25 μm

Detector #	Tau for Bias Boost (sec)
39	1200
40	1200
41	1300
42	1300
43	1700
44	1500
45	1500
46	1000
16	1000
17	—
18	1200
19	1000
20	—
21	1000
22	1200
Mean Time Constant	1238
Standard Deviation	222

Reference (TFPR) (§II.B.4). The brightness of the TFPR varies with time largely due to the Earth's annual motion through the cloud of interplanetary dust surrounding the Sun. A model of this variation was developed for use with the daily calibration observations. The method used to measure the brightness of the TFPR and the assumptions made to develop the TFPR model are the same as used for *SkyFlux* processing. This is described in the *Main Supplement* §VI.B.3. A brief description is repeated below for completeness. Improvements to the TFPR model used in the ISSA processing are explained below.

A sinusoidal variation added to a constant term was found to be a reasonable model for the TFPR brightness. The largest annual variation is due to the tilt of the symmetry plane of the zodiacal dust distribution with respect to the orbital plane of the Earth causing a variation in the line-of-sight path length through the dust cloud toward the north ecliptic pole. A secondary contribution is due to the eccentricity of the Earth's orbit that causes changes in the temperature and density of the interplanetary dust as the Earth's distance to the Sun changes. Some of the constant term in the TFPR model is due to the Galactic emission toward the north ecliptic pole.

To determine the constant term of the TFPR model, the brightness of the TFPR was measured between eight and ten times, depending on wavelength, during the IRAS mission using a special observation called the Total Flux CALibration, TFCAL. The TFCALs were

Table III.A.2(c)

Time Constants, 60 μm

Threshold = $.6E^{-11}$ Joules, $1.27E^{-6}$ $Wm^{-2}sr^{-1}$
Saturation = $3.2E^{-10}$ Joules, $6.76E^{-5}$ $Wm^{-2}sr^{-1}$

Detector #	Tau for Bias Boost (sec)	Tau for Photon Exp. (sec)	Max. Effect (%)
8	633	383	6
9	782	400	3
10	914	407	6
11	10000	476	6
12	10000	420	12
13	785	568	5
14	828	351	8
15	10000	250	8
31	10000	476	7
32	10000	439	10
33	10000	340	10
34	910	350	10
35	10000	626	5
36	—	—	—
37	10000	430	13
38	1000	375	9
Mean Time Constant	—	419	8
Standard Deviation	—	93	3

based on the fact that two observations of the TFPR at different responsivities would yield both the absolute brightness of the TFPR and the zero point of the electronics. The change in the responsivities for the 12 μm detectors was achieved by use of the alternate bias level available to those detectors. For detectors at 25, 60 and 100 μm, the TFCAL observations made use of the responsivity enhancement caused by the heavy exposure of the detectors to the protons trapped in the South Atlantic Anomaly (SAA). Normally, a bias boost was applied during and immediately after SAA passages to anneal the detectors and return the responsivity to normal. For execution of the TFCALs, the bias boost annealing was delayed for a fraction of an orbit until the satellite could point to the TFPR. Two observations of the TFPR were made separated by the bias boost annealing cycle. Flashes of the internal stimulators during both TFPR observations calibrated the responsivity before and after the bias boost. Under the assumption that the electronic zero point remained unchanged by the bias boost, the brightness of the TFPR was extracted using this method. Responsivity variations of 300 to 400% were obtained at 60 and 100 μm, while variations of 30% were typical for 12 and 25 μm.

Table III.A.2(d)

Time Constants, 100 μm

Threshold = $.6E^{-11}$ Joules, $0.57E^{-6}$ $Wm^{-2}sr^{-1}$
Saturation = $3.2E^{-10}$ Joules, $3.04E^{-5}$ $Wm^{-2}sr^{-1}$

Detector #	Tau for Bias Boost (sec)	Tau for Photon Exp. (sec)	Max. Effect (%)
55	1200	1590	22
56	980	756	23
57	2200	1554	16
58	1400	1540	20
59	1200	1565	16
60	1200	1667	20
61	1600	1616	20
62	1450	1560	18
1	1320	1460	24
2	1490	1415	17
3	1600	1867	8
4	1100	1547	23
5	1415	1420	16
6	1000	704	13
7	1000	401	12
Mean Time Constant	1344	1377	18
Standard Deviation	316	413	5

An important detail of the implementation of the TFCAL observations is the assumption that the bias boost did not alter the electronic zero point of the detectors. This was in fact an erroneous assumption. The bias boost did indeed change the electronic zero point of the detectors in most boosted modules due to heating of the cold electronics by the boosted bias current. This however was successfully modeled for removal in the TFCAL reduction process.

Independent information was obtained concerning the initial zero point for each detector from a single 'chop' experiment performed during the first week of the IRAS mission. The cryogenically cooled cover which was still in place allowed zero background conditions for detectors at 12 and 25 μm. Measurements agreed with results from the TFCALs to within 6% and 10% at 12 and 25 μm. No measurements were obtainable at 60 and 100 μm because of uncertainties in the 60 and 100 μm background levels with the cover on (*Main Supplement* §VI.B.3.a).

In principle, the sinusoidal parameters of the TFPR model could be determined from the TFCAL measurements alone. However, the limited number of TFCALs were insufficient to yield an accurate phase and amplitude of the sinusoidal component. Instead, a

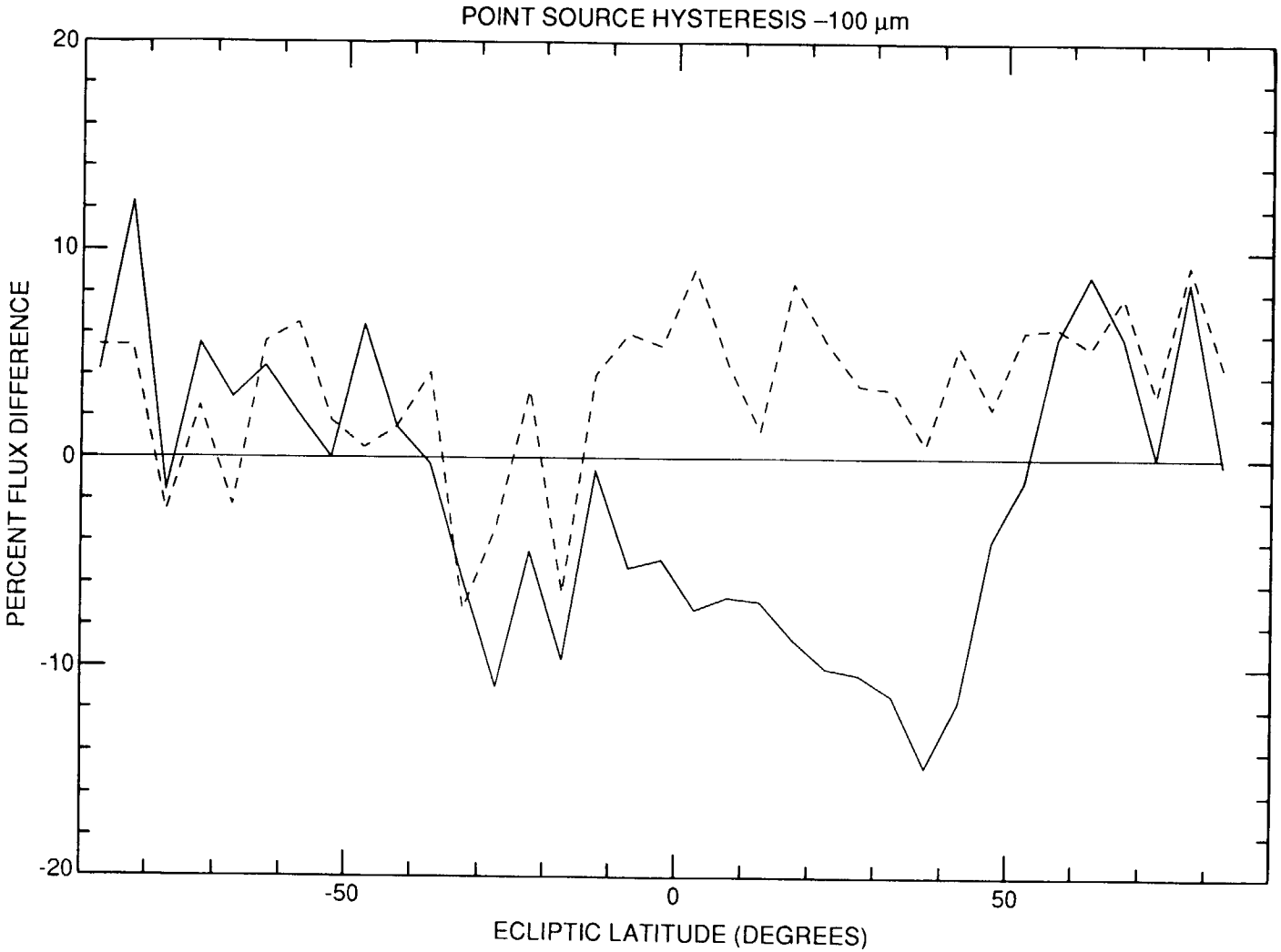

Figure III.A.1 Point Source Hysteresis Comparison — 100 μm. This figure shows the 100 μm point source flux discrepancy due to the hysteresis effect across the Galactic plane. A set of 100 μm point sources were selected along ecliptic longitude 270°. Fluxes were measured and compared from ascending and descending scans and the percent difference between the ascending and descending scans was computed. The percent differences were averaged within a 5° × 10° bin and plotted. The Galactic plane crossing is around −15° ecliptic latitude. The solid line represents the values from uncorrected scans and the broken line represents the values from hysteresis-corrected scans.

measure of the annual variation was available in the form of differences between the north and south ecliptic pole brightnesses derived from about 200 IRAS survey scans. Each scan observed both poles within 50 minutes. The difference between the polar brightnesses removed drifts on time scales greater than 50 minutes. The annual variation in the brightness at the TFPR was then derived by fitting a sinusoid to the polar differences. The amplitude of the annual variation at the TFPR is then half the variation derived from the differences. This observationally determined the effect of the Earth's motion with respect to the symmetry surface of the zodiacal dust cloud. The polar difference had the undesirable effect of canceling out the TFPR brightness variations due to the eccentricity of the Earth's orbit. To account for the eccentricity of the Earth's orbit in the TFPR model, it was necessary to add back a model which represented this variation.

When results of the TFCALs observations were combined with data extracted from survey scans connecting the north and south ecliptic poles, a smooth, sinusoidal variation in the TFPR brightness was apparent.

Two significant changes were made in the TFPR model used to produce the ISSA and ZOHF Versions 3.0 and 3.1. Unlike the previous TFPR model, the current model includes the effect of the eccentricity in the Earth's orbit about the Sun as calculated from the zodiacal emission model of J. Good (Appendix G). The special calibration observations, the TFCAL observations, which determine the constant term of the TFPR model (also described in §VI.B.3 of the *Main Supplement*), were re-analyzed with noticeably improved results. The improved values for the TFPR model are found in Table III.A.3.

The internal consistency of the TFCAL observations is now 2% or better of the TFPR brightness at 12, 60 and 100 μm and 5% at 25 μm. The zero point uncertainties in the TFPR model based upon internal inconsistencies are now 0.36, 1.2, 0.17, and 0.4 MJy sr^{-1}, at 12, 25, 60 and 100 μm, respectively. The uncertainties in the basic responsivity calibration of the IRAS data traced back to standard stars and the asteroid model remains 2%, 5%, 5% and 10% at 12, 25, 60 and 100 μm, as discussed in §VI.C.2.c on page VI–24 of the *Main Supplement*. The actual zero point uncertainties of the survey observations are larger than those of the TFPR model due to baseline drifts on time scales shorter than one day, variation of the sky position observed as the TFPR (§II.B.4) and other systematic effects discussed in §IV.

A.2.c *Other Calibration Enhancements*

The accuracy of the calibration was enhanced by the use of more accurate solid angle measurements for the detectors (see §I.D.7 and the *Explanatory Supplement to the IRAS Faint Source Survey* Version 2, §II.D.2) and a more robust method of extracting internal calibration flashes in confused areas of the sky. The improved solid angles resulted in sky brightness shifts of 13% at 12 μm, 8% at 25 μm, 3% at 60 μm and 6% at 100 μm. These band average estimates are calculated for full-sized detectors and only affect the extended emission calibration. Calibration stability was improved by a few percent due to the improved accuracy in measuring the internal reference source.

Table III.A.3 TFPR Model Parameters[1]

Effective wavelength (μm)	12	25	60	100
Parameter:[2]				
B_0 (MJy/sr)[3]	12.5	23.3	8.1	9.6
statistical uncertainty[5]	0.3	1.2	0.08	0.2
total uncertainty[6]	1.6	3.1	0.47	1.3
B_1 (MJy/sr)[3]	1.73	2.66	0.67	0.19
uncertainty[7]	0.1	0.1	0.1	0.05
φ (day)[4]	−38.3	−32.8	−34	−31
uncertainty[7]	1.6	1.5	8	9

[1] The parameters have been converted to sky brightness (MJy sr^{-1}) in order to illustrate the relative magnitudes of the parameters. The parameters were originally derived relative to the flashes of the internal reference source.

[2] At a time t in days the model assumes B[TFPR] to be:

$$\mathrm{B[TFPR]} = B_0 + B_1 \times \sin[(2\pi/365.25) \times (t - \varphi)]$$

[3] The usual convention of using a flat spectral distribution for the sources was followed in deriving the flux densities.

[4] 1983 January 1 (UT) is t = 1.0 days.

[5] The statistical uncertainty corresponds to the standard deviation in the fit to the observations.

[6] The total uncertainty incorporates uncertainties from stimulator flash stability, baseline drift corrections, frequency response, feedback resistor nonlinearities and solid angle uncertainties.

[7] This uncertainty is obtained from a combination of statistical uncertainties within model fits and the dispersion among fits to different subsets of the IRAS pole-to-pole scans.

A.3 *Deglitching*

The time-ordered detector data were improved by the removal of radiation hits. Even though IRAS used an onboard deglitcher, many artifacts with an amplitude of less than 100 times the sample noise remained in the data. These artifacts were typically due to charged particles impacting the detectors (*Main Supplement* §IV.A.6).

The deglitcher used by the ISSA is the same as that used for the *IRAS Faint Source Survey (Explanatory Supplement to the Faint Source Survey*, §II.C.2.a). The algorithm operated on the time-ordered detector data prior to phasing and compressing. The processor monitored the output of a high-pass filter over the detector data streams for events that exceeded the local detector noise by a factor of five (SNR > 5). Events with power at a frequency greater than the point source frequency threshold were identified as glitches. The glitches were replaced using linear interpolation between the data points on either side of the offending glitch and a quality flag for the interpolated sample was set appropriately to signal downstream processors that deglitching had occurred. No interpolated data were used in creating the ISSA images. The deglitch filter removed more than 95% of the radiation hits with SNR > 5. Most of the removed glitches were at 12 and 25 μm.

B. Time-Ordered to Position-Ordered Detector Data

After reprocessing the entire survey time-ordered detector data, the scans were broken into segments and re-ordered based on sky position. All scans that cover an area of sky were grouped into one database called an ISSA field. A field is an accumulation of all the time-ordered IRAS data that cross over the region of the sky defined by the field boundaries. The scans defined within an ISSA field were used to make an ISSA image.

C. Image Production

The following steps, described in detail below, precede the creation of the ISSA images. An empirically derived adjustment was applied to the 25 μm detectors, the zodiacal foreground was removed and two destriping algorithms were implemented. Then the individual HCON images were produced, along with the co-added images. Data in the position of known asteroids were removed in the process of making the co-added images. These data were not removed from individual HCON images.

C.1 *Empirical Corrections*

An empirical correction in offset and gain to reduce scan-to-scan variations, visible in the ZOHF product was derived by F. Boulanger for 80% of the survey scans in the ZOHF Version 3.0 at 12, 25 and 60 μm (Appendix F and Boulanger and Pérault 1988).

Although the intent was to reduce striping in the ZOHF, the corrections proved effective in reducing the scan-to-scan variations in the ISSA at 25 μm. The 25 μm detectors were highly correlated in their scan-to-scan variations making the application of a single gain and offset to *each* detector within a scan effective in reducing the scan-to-scan striping at 25 μm in the ISSA. The average gain correction at 25 μm was 1.001 and the RMS of gain corrections at 25 μm was 1.032 (Appendix F). The 12 μm and 60 μm detectors did not demonstrate the same detector-to-detector correlation and the Boulanger corrections

were not applied to these detectors. No corrections were available for 20% of the survey scans due to constraints in the empirical procedure.

C.2. *Zodiacal Foreground Removal*

Zodiacal dust emission is a prominent source of diffuse emission in all IRAS survey bands. The apparent dust temperature of about 250 K makes the zodiacal emission most prominent in the 12 and 25 μm bands. The dust distribution is concentrated toward the ecliptic plane. The zodiacal contribution to the observed surface brightness depends on the amount of interplanetary dust along the particular line-of-sight, an amount which varies with the Earth's position within the dust cloud. Consequently, the sky brightness of a particular location on the sky, as observed by IRAS, changes with time as the Earth moves along its orbit around the Sun. The effect of the variable zodiacal emission was to introduce step discontinuities in the *SkyFlux* images where adjacent patches of sky were observed at different times. These artificial gradients, as well as the natural gradients associated with the concentration of zodiacal emission toward the ecliptic plane, obscured faint features on the sky and made useful co-addition of the several HCONs difficult. A zodiacal emission model was subtracted from the ISSA data to reduce the foreground zodiacal emission and make it possible to co-add the remaining emission.

A physical model of the zodiacal foreground emission based on the radiative properties and spatial distribution of the zodiacal dust was used to estimate the large-scale zodiacal emission. It is described in detail in Appendix G. The use of a physical model allowed a consistent prediction of the zodiacal emission for scans at large solar elongations where empirical models would have difficulty due to the paucity of IRAS data at such angles.

The model used fourteen parameters to describe the dust distribution and the radiative properties of the dust. They include features such as dust cloud density, tilt of the dust symmetry plane with respect to the ecliptic plane and emissivity of the dust as a function of wavelength. The predicted zodiacal emission for direction and time was obtained by integration of dust emission along that line-of-sight through the model dust cloud. The parameters were determined by fitting the model to a selected set of IRAS scans. Because the model assumed a physical dust distribution that did *not* include the zodiacal dust bands, the zodiacal dust bands remain in the data.

Users wishing to know the total sky brightness in a particular region as observed by IRAS may do so by using the ZOHF Version 3.1 (§I.F).

Zodiacal emission subtraction removed 95% of the total brightness at the north ecliptic pole at 12 and 25 μm. The residual zodiacal emission seen at the north ecliptic pole at 12 and 25 μm shows variations of 0.5 MJy sr^{-1} and 1.0 MJy sr^{-1}, respectively. This appears in the ISSA images as a "bow-tie" at the pole. At intermediate latitudes this variation in residual foreground appears as low-frequency (greater than 5° period) striping of somewhat lower amplitude than the polar bow-tie (0.2 MJy sr^{-1} at 12 μm). The residuals increase to 1.0 MJy sr^{-1} and 2.0 MJy sr^{-1} at 12 and 25 μm for fields near the ecliptic plane.

C.3 *Destriping*

Due to imperfections in the calibration and zodiacal models, detector-to-detector stripes remained in the IRAS detector data. Without destriping, the ratio of cross-scan to in-scan RMS noise in a flat region of the sky at 12 and 25 μm is between two and three, and between 1.5 and 2.0 at 60 and 100 μm. Since a goal of ISSA was to have the cross-scan RMS noise be equivalent to the in-scan RMS noise, two methods to remove detector-to-detector variations were implemented. Each used information from crossing scans to derive destripe parameters. Each detector of each scan was corrected with an offset computed from the derived parameters. No gain corrections were applied.

The two algorithms are referred to as the global destriper and the local destriper. The global destriper utilized the entire IRAS survey time-ordered, zodiacal-emission-removed dataset to derive destripe parameters for each detector within a scan. The global corrections not only assisted in decreasing the detector-to-detector striping but also brought the three sky coverages (HCONs) to a common background level. This allows mosaicking without additional offset adjustments. The local destripe parameters were derived from the position-ordered, globally-corrected detector data. The local destriper reduced the cross-scan RMS noise as measured after global destriping by an additional 10%.

The combination of the two methods reduced the cross-scan striping such that the ratio of cross-scan to in-scan RMS noise in flat regions is nearly 1.0 for all bands (§IV.E.1).

C.3.a *Global Destriper Overview*

The following is a brief overview of the global destriper. A detailed description can be found in Appendix D. Global destriping of ISSA was accomplished using a BasketWeave DeStriping algorithm (BWDS) (Emerson and Gräves 1988). This algorithm was based on the assumption that each detector of the same wavelength should see the same intensity when pointed at the same spot in the sky anytime during the mission after removal of the zodiacal emission. A typical detector scan path during a single observation crosses the paths of many hundreds of other detectors of the same wavelength taken at other times during the mission. It was therefore possible to generate an intensity difference history for each detector scan. The difference data were fit with a polynomial. Each scan was then adjusted by a portion of the difference between the original scan and the fit. The process was repeated until the differences were minimized.

There were a number of difficulties involved in implementing this approach, including issues related to anomalies in the incoming datastream as well as the completeness of the zodiacal emission and hysteresis removal. One major consideration was the enormous size of the database needed to support a global basketweaver. Over the entire mission, there were 1.2 million focal plane crossings. After careful selection (Appendix D) the final database size ranged between 470 megabytes for 25 μm to 730 megabytes at 12 μm. The size of the database affected fitting and checking strategies.

Intensity difference fits were performed for each scan at each wavelength using at most tenth order orthogonal polynomials. The fit technique and order varied to some extent with wavelength.

Intensity difference plots provided good visibility as to the quality of the fit. However, due to the volume of data, comprehensive manual checking using plots alone was not feasible. A computer program analyzed the fits for each detector within each scan, producing a set of parameters. These parameters served to indicate possible fitting problems. Histograms were generated for each parameter and the fits which produced extreme outliers were investigated. Identified problems were either fixed or removed (Appendix D).

C.3.b. *Local Destriper*

The local destriper algorithm was based on the same assumption as the global algorithm. Each detector of the same wavelength should see the same intensity when pointed at the same spot in the sky at any time during the mission after removal of zodiacal emission. However, the local destriper operated only on portions of scans within a region of an ISSA field. Unlike the global destriper, which utilized a subset of focal plane crossings, the local destriper utilized information from all focal plane crossings within the defined region. The local destriper was effective in further reducing the cross-scan RMS noise left by the global destriper by about 10%.

Input to the local destriper was position-ordered, zodiacal-emission-removed, globally corrected detector data. The process of deriving local destripe parameters involved several steps. A co-added image was made of all scan segments within a defined region of sky. Then the trajectory of the detector over the co-added image was determined. Differences were taken between the intensity values of the detector along the scan and the corresponding co-added intensities along the scan trajectory. A first-order function was fit to the differences for each detector. Finally, detector intensity values were corrected with the derived parameters and a new co-added image was created. The process was repeated for five iterations.

The iterations of the co-added image were made at varying pixel sizes, from $12.0'$ for the first iteration to $1.5'$ for the final. Starting with a coarse co-added image as a template helped in reducing the lower frequency striping. Point sources were detected and excluded from the co-added image to prevent a large point source influencing a coarse pixel and thereby influencing the detector scan differences and subsequent fit.

An error in the local destriper software resulted in some scans in the $|\beta| > 50°$ sky receiving poor fits from this processor. The error occurred whenever a scan had a time gap in the time-ordered detector data. Most of these local destripe problems were removed in the quality checking process, (§III.D). Some remain in the $|\beta| > 50°$ images (§I.E.3). The software was fixed for processing the $|\beta| < 50°$ sky.

Due to the residual zodiacal emission near the ecliptic plane and the lack of crossing scans, the fields covering the $|\beta| < 50°$ sky were processed differently through the local destriper from the fields covering the $|\beta| > 50°$ sky. For the high-ecliptic-latitude sky, pa-

Table III.C.1(a)

Field-Groups for 12 and 25 μm

Field-Group	ISSA and ISSA Reject Fields
1	209 210 211 245 246 247 281 282 283 315 316 317 346 347 348 373 374 375
2	140 141 142 143 176 177 178 179 212 213 214 215 248 249 250 251 284 285 286 318 319 320 349 350
3	54 80 81 110 111 112 144 145 146 180 181 182 216 217 218 252 253 25 4 287 288 289 290 321 322 323 351 352 353 354
4	56 57 82 83 84 113 114 115 147 148 149 183 184 185 219 220 22 1 255 256 257 291 292
5	37 57 58 59 60 84 85 86 87 115 116 117 118 149 15 0 151 152 185 186 187 188 221 222 223 224 257 258 259 260 292
6	37 38 39 40 60 61 62 63 87 88 89 90 118 119 120 121 152 153 154 155 188 189 190 191 224 225 226 227 260 261 262 263
7	91 92 93 122 123 124 156 157 158 192 193 194 228 229 230 264 265 26 6 299 300
8	94 125 126 159 160 161 195 196 197 231 232 267 268 301 302
9	95 127 128 129 162 163 164 198 199 233 234 235 269 303 304 335 336
10	97 129 130 131 163 164 165 166 198 199 200 201 202 234 235 236 237 238 270 271 272 273 274 304 305 306 307 308 335 336 337 338 339 364
11	132 167 168 203 204 205 239 240 241 275 276 277 309 310 311 340 341 342 368 369
12	169 170 171 172 205 206 207 208 241 242 243 244 277 278 279 280 311 312 313 314 342 343 344 345 369 370 371 372 392 393 394 395
13	155 156 157 191 192 193 227 228 229 230 231 263 264 265 266 267 297 298 299 300 301 331 332 333 360 361

rameters were derived for each detector within a 12.5° field independent of the surrounding fields. This was possible due to the large number of crossing scans within any given field at the higher latitudes. For fields nearer the ecliptic plane, the scans were nearly parallel and therefore did not have as much crossing information to reduce the effect of the residual zodiacal emission. Processing these fields independently of surrounding fields would have resulted in poorer quality images and the loss of the ability to mosaic. To take advantage of the surrounding information, several 12.5° fields (20–40) were concatonated into one large field, known as a field-group, and sent through the local destriper. Parameters were derived, as before, for each scan segment within a field-group. Even though a single IRAS scan crossed several ISSA 12.5° fields which make up a field-group, the different

Table III.C.1(b)

Field-Groups for 60 and 100 μm

Field-Group	ISSA and ISSA Reject Fields
1	139 172 173 174 175 208 209 210 211 244 245 246 247 280 281 282 283 314 315 316 317 345 346 347 348 372 373 374 375 395
2	108 109 139 140 141 142 143 175 176 177 178 179 211 212 213 214 215 247 248 249 250 251 283 284 285 286 317 318 319 320 348 349 350 375
3	54 55 80 81 82 109 110 111 112 143 144 145 146 179 180 181 1 82 215 216 217 218 251 252 253 254 286 287 288 289 290 320 321 322 323 350 351 352 353 354
4	56 57 58 59 82 83 84 85 86 113 114 115 116 147 1 48 149 150 183 184 185 186 219 220 221 222 255 256 257 258 290 291 292 323
5	37 38 58 59 60 61 85 86 87 88 116 117 118 119 150 151 152 153 186 187 188 189 222 223 224 225 258 259 260 261
6	37 38 39 40 60 61 62 63 87 88 89 90 118 119 120 121 152 153 154 155 188 189 190 191 224 225 226 227 260 261 262 263
7	40 63 64 65 66 90 91 92 93 121 122 123 124 155 1 56 157 158 191 192 193 227 228 229 230 263 264 265 266 298 299 300 331 332
8	66 67 93 94 95 96 124 125 126 127 128 158 159 160 161 162 194 195 196 197 198 230 231 232 233 234 266 267 268 269 270 300 301 302 303 304 332 333 334 335 364
9	95 96 97 127 128 129 130 131 162 163 164 165 166 198 199 200 201 2 02 234 235 236 237 238 270 271 272 273 304 305 306 307 308 335 336 337 338 339 364
10	100 130 131 132 165 166 167 168 201 202 203 204 237 238 239 240 272 273 274 275 276 307 308 309 310 338 339 340 341 364 367 368
11	169 170 171 172 205 206 207 208 241 242 243 244 277 278 279 280 311 312 313 314 342 343 344 345 369 370 371 372 392 393 394 395

scan segments were treated separately when deriving local destripe parameters. Including information from adjacent fields forced agreement in the overlap regions. The overlap from the adjacent fields and from higher latitude fields where there are crossing scans allowed a better destriping result. For the 12 μm and 25 μm images, the sky was divided into 13 field-groups. A list of ISSA fields that make up each field-group is found in Tables III.C.1(a) and III.C.1(b). Field-groups were defined differently for 60 μm and 100 μm as shown in Figures III.C.1(a) and III.C.1(b). Some field-groups overlapped to preserve integrity at field boundaries. By using these large fields as input to the local destriper, most images remain mosaickable. Boundary discrepancies, on the order of one to two MJy sr^{-1} at 60 μm and three to five MJy sr^{-1} at 100 μm, remain near the Galactic plane and where the higher latitude fields join the field-groups.

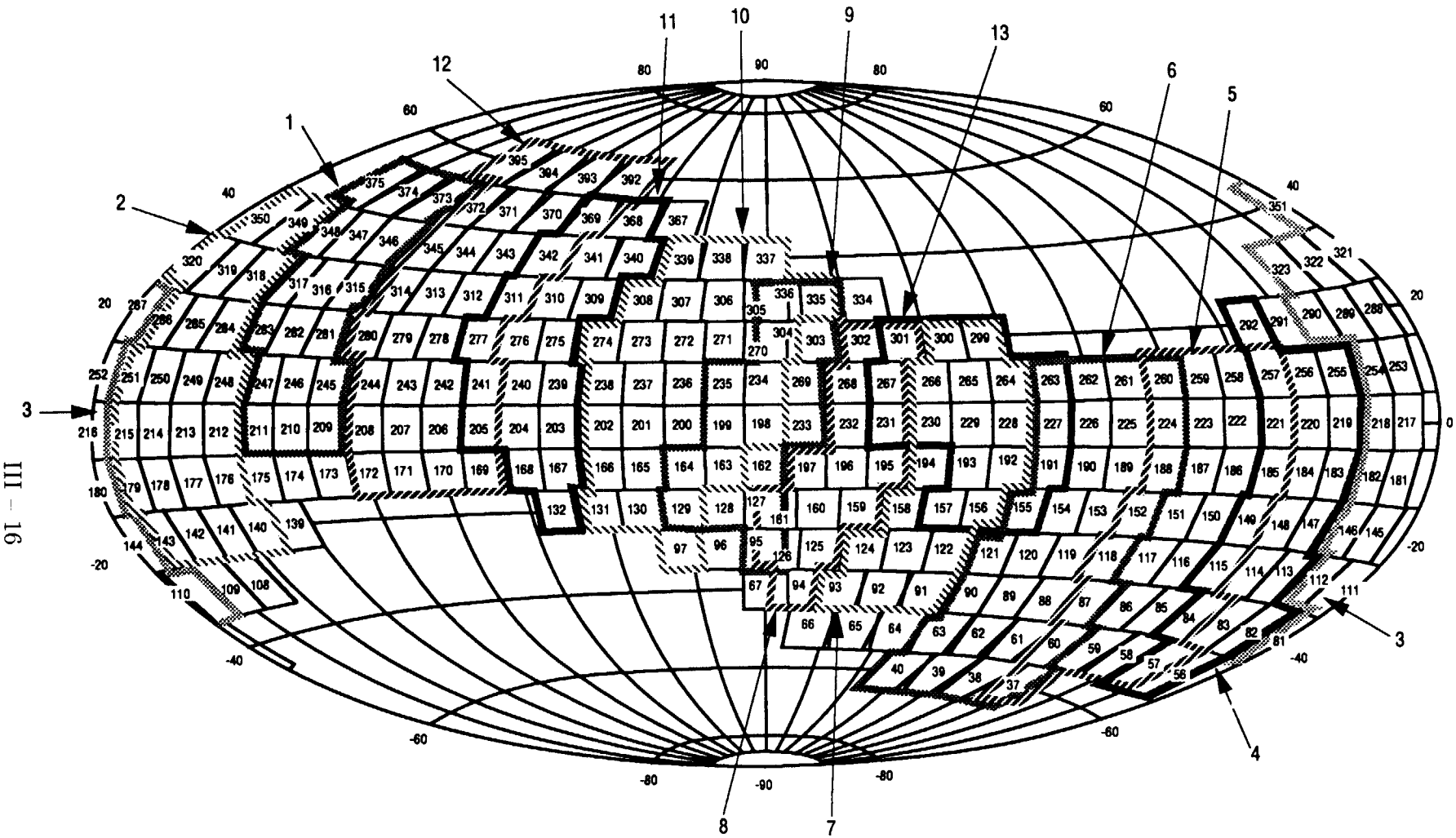

Figure III.C.1(a) Field-Group Boundaries for the 12 and 25 μm Local Destriper Processing in Equatorial Coordinates

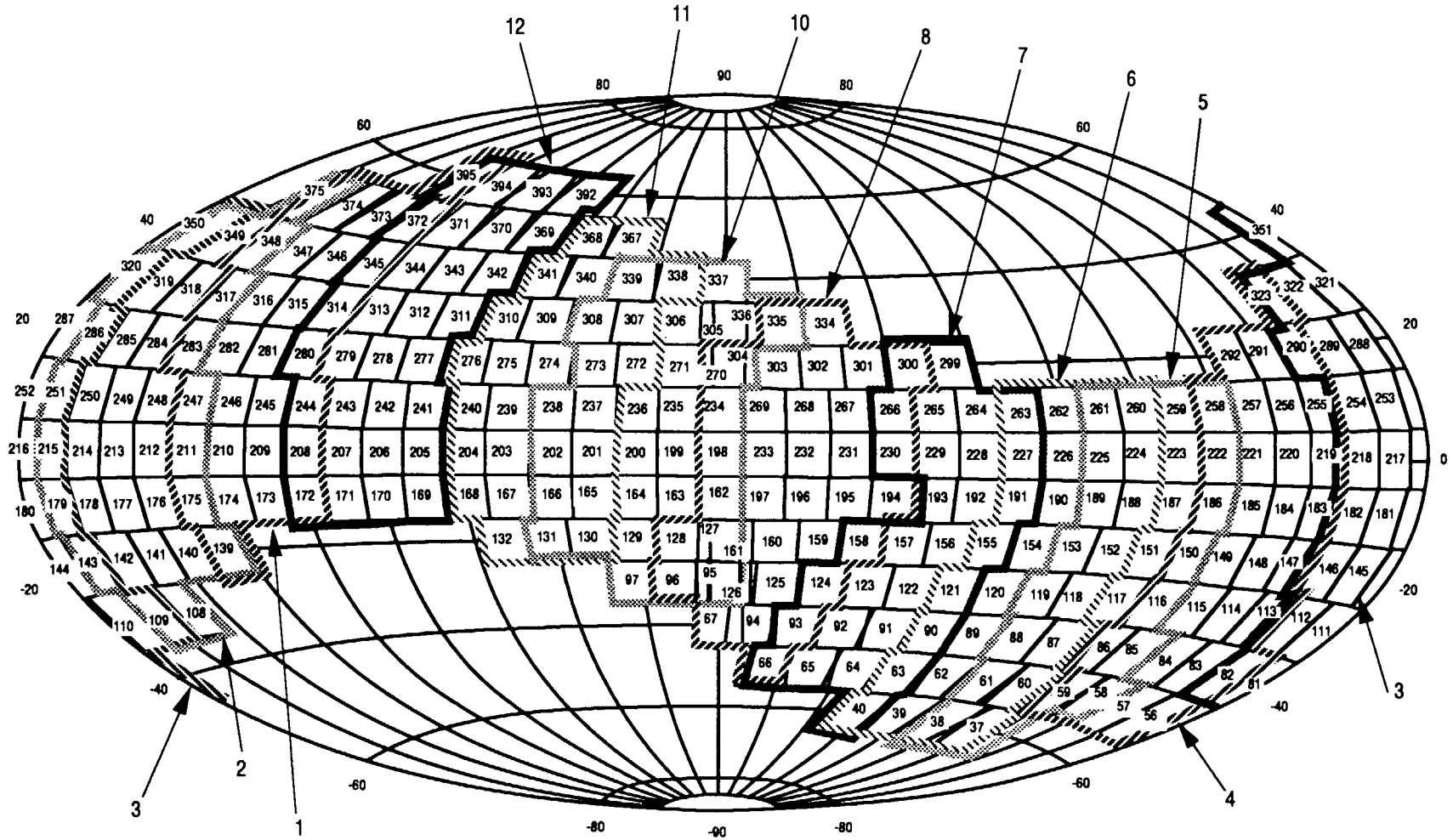

Figure III.C.1(b) Field-Group Boundaries for the 60 and 100 μm Local Destriper Processing in Equatorial Coordinates

C.4 *Image Assembly*

Once the zodiacal foreground and detector stripes were removed, the position-ordered detector data were projected and binned into an image. This process utilized a gnomonic projection to convert sky position into image line and sample values for each detector. After all scans were binned for a given field into separate HCON images, the co-added images were created. Data in the positions of known asteroids were removed from the individual HCON data stream prior to creating the co-added images. All images were then visually inspected for anomalies.

The gnomonic projection used in the ISSA was the same as that used in the *SkyFlux* images (*Main Supplement* §X.D.2.a). It produced a geometric projection of the celestial sphere onto a tangent plane from a center of projection at the center of the sphere. Each individual field has its own tangent projection plane with the tangent point at the center of the field. The ISSA binning algorithm placed the detector intensity value into each pixel within a 2′ radius of the actual detector position on the image. No adjustment was made for scan direction and there was no weighting based on the spatial responsivity function of the detectors. The resultant point spread functions are discussed in §IV.C. Cumulative information per pixel was kept for each HCON, including the sum of intensities, counts and sum of intensities squared. After all scans were binned, a final intensity image at each wavelength was made by using the simple mean intensity at each pixel. An image of the standard deviation was also calculated.

The number of data points per pixel varies depending on sky coverage. For the sky covered by two HCONs, a typical average count per pixel is 10–14 depending on band with a maximum count of around 16. For the sky covered by three HCONs, a typical average count per pixel is 15–20 depending on band with a maximum count of around 30. These counts increase for fields at higher ecliptic latitudes. At the north ecliptic pole a typical average is 25–50 with a maximum of around 65–70.

An attempt was made to automate the rejection of nonconfirming objects prior to co-addition by examining the flux distribution within a single pixel. In principle, a non-confirming object would differ sufficiently from the overall distribution such that it could be recognized and rejected by setting a simple threshold based on the flux distribution. However, the distribution of brightness among scans was so varied, especially around point sources, that nonconfirming objects could not be rejected without setting the threshold to one or two sigma. In addition, asteroids are only 2.1σ from the mean in the part of the sky covered by three HCONs. *Therefore, no confirmation algorithm was implemented.*

Since the population distribution was not useful in separating out artifacts, the noise images (§I.C) were considered to be of minimal utility and therefore were not released.

Data in the position of known asteroids were removed only from the co-added images. A list was obtained from the *IRAS Asteroid and Comet Survey* (Matson 1986). This database provided detector and sighting times. The actual window of data removed depended on the duration of the sighting on a detector. A pad of one second prior and two seconds after the given sighting was used to account for the effects of the convolu-

tion filter used in creating the compressed, time-ordered detector data. Comet tails and trails were *not* removed from the co-added images. Most comet trails appear near the ecliptic plane where there remains a difference in the residual zodiacal foreground between HCONs primarily due to the zodiacal bands. Given the different background levels for each HCON, the removal of comet trails in this region from the individual HCON data prior to co-addition would result in undesirable streaks in the co-added image along the paths of the clipped comet trails. No fields in the $|\beta| > 50°$ sky are affected by comet *trails*. The comet *tail* of IRAS-Araki-Alcock is seen in fields 416 and 418. A list of fields affected by comet trails is found in Table III.C.2. Figure III.C.2 shows the comet trails for different HCONs. Note that all but four fields (128, 129, 166 and 167) are from the *ISSA Reject Set*. A list of trail positions is found in Sykes and Walker 1992.

Table III.C.2
ISSA and ISSA Reject Fields Containing Comet Trails

Field	Field	Field
115	164	203
116	166*	204
117	167*	216
118	180	217
119	181	218
120	182	219
121	183	220
128*	184	221
129*	185	232
145	190	233
146	191	234
147	192	235
148	193	236
149	194	252
150	195	253
153	196	254
154	197	255
155	198	272
159	199	282
160	200	283
162	201	316
163	202	317

* ISSA fields NOT in the ISSA Reject Set.

Table III.C.3 lists the position and corresponding ISSA field affected by planets. Jupiter was specifically avoided during the IRAS mission due to the stength of its infrared radiation. Mars was not viewed by IRAS due to a coincidence between its motion

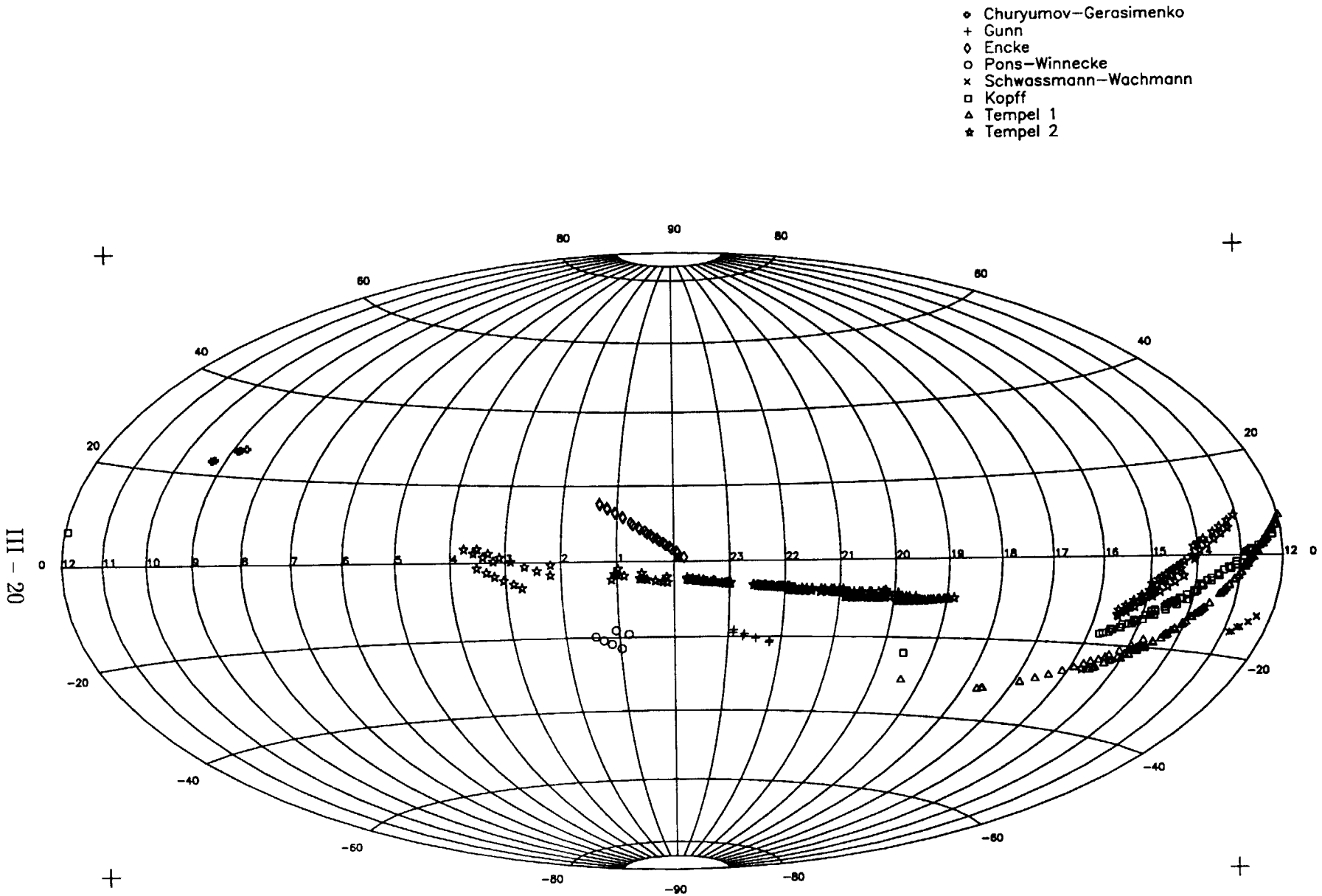

Figure III.C.2 Known Comet Trails as Seen by IRAS Plotted in Equatorial Coordinates

and the timing of survey observations near its location. Venus and Mercury were not scanned due to their proximity to the Sun. Pluto is too faint to be detectable in the ISSA data (Aumann and Walker 1987).

Table III.C.3
Planet Positions and Corresponding ISSA and ISSA Reject Fields

Planet	Field	RA	DEC
Uranus	150	16h10m36.9s	−21d02m21s
Saturn	183	13h45m18.2s	−08d13m07s
Neptune	152	17h43m03.5s	−22d13m57s
Neptune	153	17h54m20.9s	−22d11m59s

D. Quality Checking

ISSA data were subjected to quality checks during the pre-production, production and post-production processing stages.

D.1 *Pre-Production*

Prior to image production, a machine-readable file of previously identified anomalous scans was compiled. The file contains start and stop times of the scans to clip completely from processing. The various sources from which this clipping information was culled include the *SkyFlux* images, telescope pointing anomalies discovered during production of the *IRAS Faint Source Survey* and scans identified through individual research efforts. A summary list is presented in Appendix C.

D.2 *Production*

During image production, the global basketweaver corrections were applied to each scan in a given field. There were several conditions, however, that could prevent the global corrections from being applied to a portion or all of a scan (Appendix D). In these cases either the scan was completely ignored in downstream processing or was turned over to the local destriper to derive a fit to the local background.

D.3 *Post-Production*

The final step of the quality checking was to inspect each image visually to identify any anomalous data not removed in the previous quality checking. Individual HCON images were examined to identify anomalous features. When found, the end points of the scan portion containing the anomaly were identified and that entire scan portion was removed. The main criterion for removal of an anomaly at this stage was that it not confirm in another HCON image for that field. Identified anomalies were removed from both the individual HCON images and the co-added images. Once an anomaly was removed, the field was reprocessed, creating a new set of individual HCON and co-added images which were again inspected to verify removal of the anomaly.

In general, anomalies found during this process consisted of detections of nonconfirming space debris or showers of energetic particles. As mentioned in §III.C.4, comet tails and trails were not removed. The tail of comet Iras-Araki-Alcock is seen in fields 416 and 418. If an anomaly appeared faint or was not covered by another HCON it was generally not removed. Anomalies not seen in the co-added image or near a field boundary were not removed.

To maintain consistency during a somewhat subjective process, one person, Gwen Johnson, performed the inspections and identifications of anomalies for all images during this post-production quality check.

The amount of data removed during the post-production quality checking of the $|\beta| > 20°$ sky is shown in Table III.D.1(a). The amount of data removed from the *ISSA Reject Set* is shown in Table III.D.1(b).

Table III.D.1(a)

Amount of Data Removed in Anomaly Processing ($|\beta| > 20°$)

Wavelength (μm)	% Data Removed ($|\beta| > 50°$)	% Data Removed ($|\beta| < 50°$)
12	0.18	0.51
25	0.30	0.31
60	0.14	0.24
100	0.07	0.26

Table III.D.1(b)

Amount of Data Removed in Anomaly Processing of the ISSA Reject Set ($|\beta| < 20°$)

Wavelength (μm)	% Data Removed
12	0.34
25	0.30
60	0.27
100	0.47

D.4 *Types of Anomalies*

An attempt was made to characterize the anomalies found by visual inspection. Anomalies fell into two main groups, data anomalies and processing anomalies, which are described below. Most of these anomalies were removed through the visual inspection process described in §III.D.3. All processing problems were corrected in the software except those that caused the improper handling of saturated data.

D.4.a *Data Anomalies*

— Focal Plane and Partial Focal Plane Anomalies

All or a subset of the detectors in the focal plane jumped to a higher intensity for a time then fell back to approximately their original intensity. Both the rise and fall were fairly sharp. This was likely due to either a particle or paint flake in the near field of the telescope or by a shower of secondary energetic particles from the observing structure. Figure III.D.1 shows the distribution of focal plane anomalies.

— Detector Streaks/Ministreaks

One or a few detectors showed nonconfirming spikes or raised intensity. Generally the mini-streaks were due to orbital debris in the field of view, whereas detector streaks were due to calibration problems. The distribution of detector streaks and ministreaks is found in Figure III.D.2.

D.4.b *Processing Anomalies*

— Local Destriper

These anomalies were shown to appear only after the local destriper processing. They were caused by an error in the local destriper software that did not account for data gaps in the time-ordered detector data. A number of local destriper anomalies were left in these images because they were not bright enough to stand out visibly. This error was corrected prior to processing the $|\beta| < 50°$ sky. Distribution of local destriper anomalies for the $|\beta| > 50°$ sky is found in Figure III.D.3.

— Saturated Detector Data

An error was found in the algorithm for handling saturated intensity values. This error affected the *SkyFlux* images as well as the entire set of ISSA images. The algorithm eliminated the wrong detector when saturation occurred. This resulted in the inclusion of saturated intensity values in making the images while erroneously eliminating some nonsaturated intensity values. Figure III.D.4 shows that the problem occurred mainly in the Galactic plane where 60 and 100 μm detectors saturate. Table III.D.2 provides a list of fields along with the number of occurrences in each field. The total number of occurrences throughout the mission is 6,289. Each occurrence reflects a single detector saturation. There may be several detectors saturated within a second of data. Assuming that on an average ten detectors saturate per second, the total number of occurrences is about $< 0.005\%$ of the survey data.

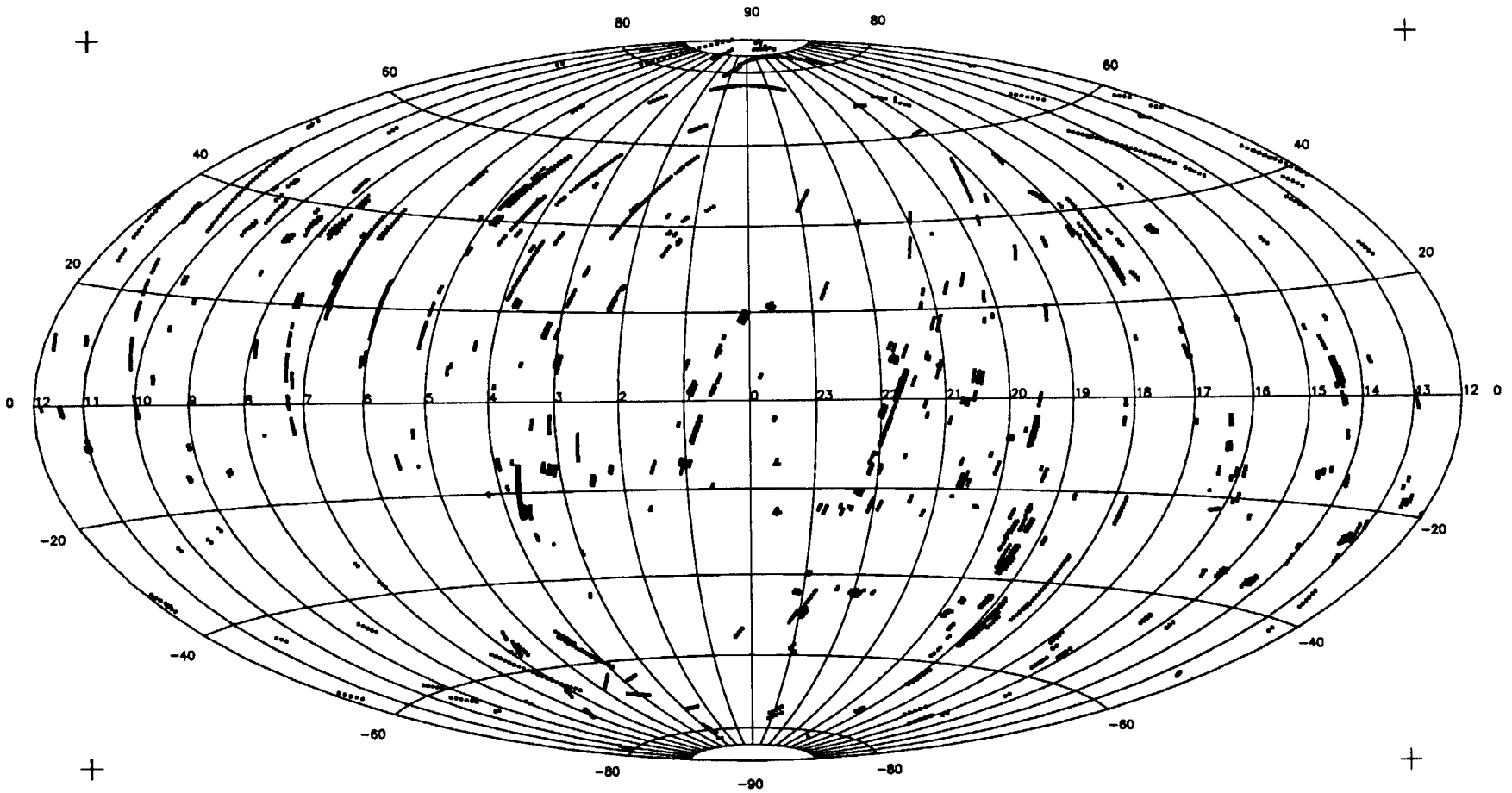

Figure III.D.1 Distribution of Focal Plane Anomalies Plotted in Equatorial Coordinates

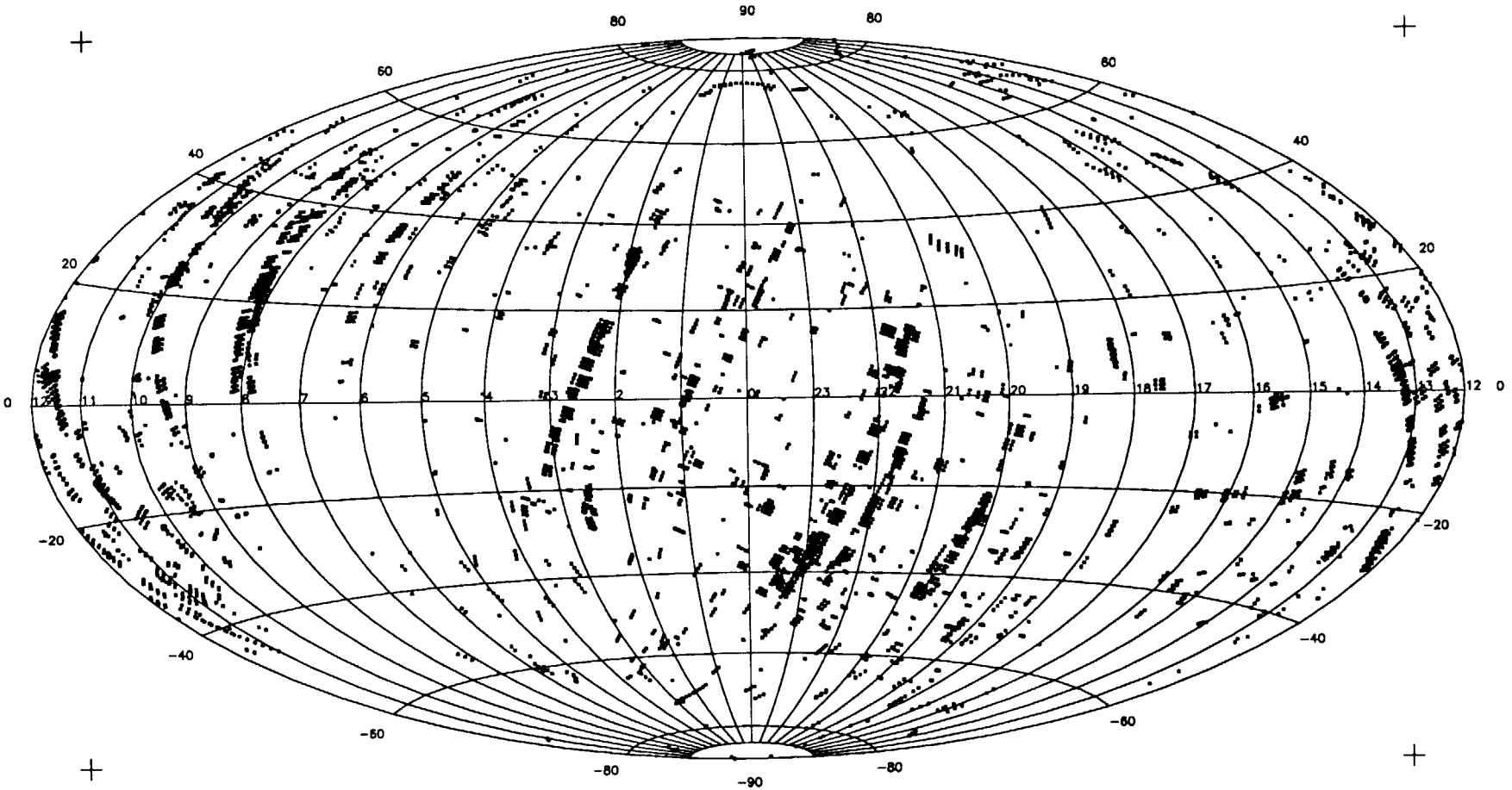

Figure III.D.2 Distribution of Mini-Streak and Detector-Streak Anomalies Plotted in Equatorial Coordinates

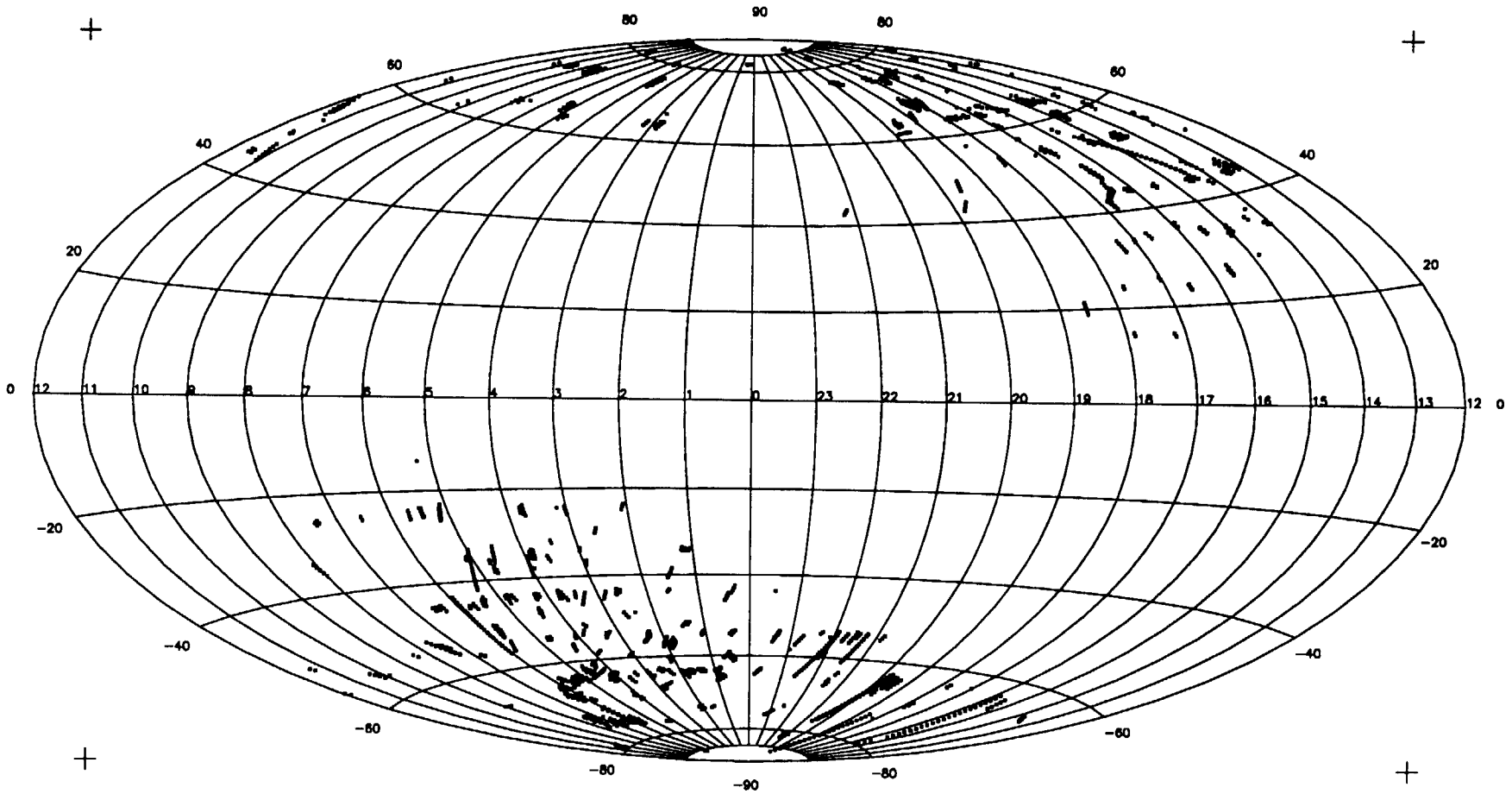

Figure III.D.3 Distribution of Local Destripe Anomalies for $|\beta| > 50°$, Plotted in Equatorial Coordinates

Table III.D.2

ISSA and ISSA Reject Fields Affected by Saturated Data

Field #	Occurrences	Field #	Occurrences
17	14	153	387
18	12	170	338
32	194	171	103
33	289	182	22
34	24	* 183	22
35	30	189	278
36	76	* 190	278
37	57	206	436
52	113	207	196
58	17	226	136
59	369	227	14
60	119	248	12
77	32	* 249	12
78	27	262	8
86	37	263	163
87	448	284	10
104	8	297	77
* 105	8	298	115
117	374	331	2
118	1603	360	6
119	30	361	4
137	8	390	9
* 138	8	391	59
152	27	407	6

* Overlapping area with adjacent field not included in total.

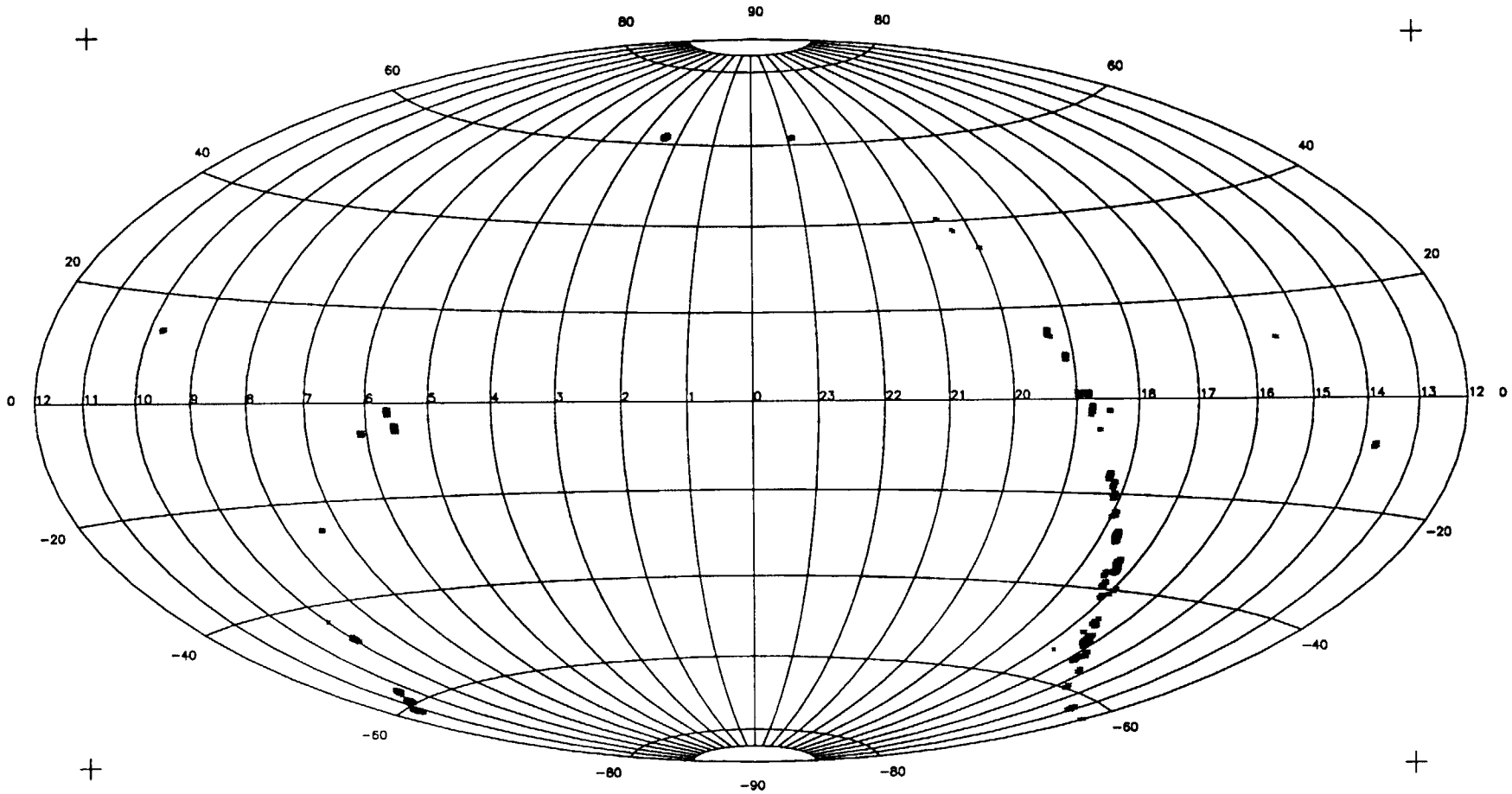

Figure III.D.4 Occurrences of Saturated Data for Entire Sky, Plotted in Equatorial Coordinates

IV. ANALYSIS RESULTS

A. Analysis Overview

Analysis of the *IRAS Sky Survey Atlas* was designed to verify the accuracy and analyze the quality of the ISSA images. The analysis is mainly confined to the high-ecliptic-latitude sky, released in 1991. The analysis concentrated on the position accuracy, photometric consistency, spatial resolution and noise of the Atlas. The results reported here are applicable to the entire ISSA data set, which covers the $|\beta| > 20°$ sky. The remaining set of images covering the $|\beta| < 20°$ sky is of reduced quality and considered a separate product, *ISSA Reject Set*. The reduction in quality is due to residual zodiacal emission at the ecliptic plane and the zodiacal bands. A separate analysis is presented for these images, §IV.F. The analysis results show that the ISSA images are accurate to within the limitations of the IRAS data. ISSA data are positioned accurately to better than 0.1 pixel. The spatial resolution of ISSA is 4.5′ to 5′. Measurement of ISSA point sources show that the data are photometrically consistent with the *IRAS Point Source Catalog* to within 10%. This uncertainty is due to the positioning of a point source within the convolution filter that was used to resample the full resolution IRAS data to 2′ samples (Appendix B). Relative surface brightness photometry over large spatial scales is possible. The effects of detector-to-detector offsets and zodiacal emission shifts have been reduced so that the noise level in the ISSA images in the high-ecliptic latitude sky is approximately that expected from the noise in individual IRAS detectors.

B. Positional Accuracy

Positional accuracy and small source photometric consistency were studied using point sources selected from the *IRAS Point Source Catalog* to be bright enough to measure easily in the ISSA data and to be free of interference from extended emission or nearby point sources. Point sources at 12 and 25 μm were selected to be at high Galactic latitude, $|b| > 30°$, with brightness between 5 and 55 Jy and correlation coefficients of 0.99 or greater. The 23 sources at 12 μm and 24 sources at 25 μm are listed in Table IV.B.1. Point sources at 60 and 100 μm were selected from the IRAS galaxy list (Soifer *et al.*, 1987) to have a large radial velocity (> 4000 km s^{-1}) with brightness between 5 and 55 Jy. The velocity criterion is designed to select small angular diameter galaxies unlikely to be extended at the resolution of the ISSA maps. The 14 sources at 60 μm and 15 sources at 100 μm are listed in Table IV.B.1.

Table IV.B.1
Point Sources Used in the Position and Photometric Analyses

12 μm		25 μm		60 μm		100 μm	
IRAS Name	Field	IRAS Name	Field	IRAS Name	Field	IRAS Name	Field
00515 − 6308	25	00515 − 6308	25	00163 − 1039	162†	00163 − 1039	162†
01452 − 8026	3	01452 − 8026	3	02228 − 2500	98	02228 − 2500	98
02039 − 5722	26	02039 − 5722	26	04315 − 0840	169†	04315 − 0840	169†
02110 − 7143	11	02110 − 7143	11	04461 − 0624	169†	04461 − 0624	169†
02238 − 5947	26	02238 − 5947	26	05189 − 2524	135	05189 − 2524	135
03040 − 8013	3	03040 − 8013	3	08354 + 2555	316†	09320 + 6134	397
03336 − 7636	3	03336 − 7636	3	09320 + 6134	397	09437 + 0317	213†
05150 − 4056	73	04330 − 6307	28	10565 + 2448	319†	10565 + 2448	319†
05174 − 3345	102	05150 − 4056	73	12540 + 5708	399	12540 + 5708	399
05217 − 3943	73	05174 − 3345	102	12590 + 2934	322†	12590 + 2934	322†
05345 − 4406	73	05217 − 3943	73	13136 + 6223	399	13136 + 6223	399
10416 + 6740	414	05345 − 4406	73	13136 + 6223	400	13136 + 6223	400
10521 + 7208	414	10416 + 6740	414	13183 + 3423	322†	13183 + 3423	322†
11284 + 6936	415	10521 + 7208	414	23488 + 2018	270†	23488 + 2018	270†
15448 + 3828	355	11284 + 6936	415	23591 + 2312	270†	23591 + 2312	270†
15566 + 3609	355	15448 + 3828	355				
16164 + 5952	402	15566 + 3609	355				
16342 + 6034	402	16164 + 5952	402				
17126 + 3625	357	16342 + 6034	402				
17133 + 3651	357	17126 + 3625	357				
17329 + 5359	383	17133 + 3651	357				
17403 + 6234	403	17329 + 5359	383				
		17403 + 6234	403				
		20427 − 8243	9				

† These fields are from the $|\beta| < 50°$ sky.

The position accuracy analysis consisted of comparing the apparent position of the selected sources in the ISSA maps with the published source locations in the *IRAS Point Source Catalog*. The ISSA position was taken to be the photocenter of the source in the ISSA map. Photocenters were obtained by producing a flux-weighted average of the pixel positions over a circular region surrounding a source after subtraction of a local background. Figures IV.B.1(a) and IV.B.1(b) display histograms of difference between the PSC position and the ISSA position for the selected point sources. Table IV.B.2 summarizes the statistics obtained from the histograms. The mean position differences between the PSC and ISSA are less than 0.1 pixel (9″) and the expected position uncertainty of a single source is less than 0.2 pixel (18″).

Table IV.B.2
Position Difference Statistics

	12 μm	25 μm	60 μm	100 μm
# of Sources	23	24	14	15
Mean Δ R.A. (′)	0.004	0.001	0.040	0.031
$\sigma(\Delta$ R.A.)(′)	0.156	0.267	0.179	0.224
Mean Δ Dec. (′)	0.070	0.034	−0.078	−0.131
$\sigma(\Delta$ Dec.)(′)	0.126	0.225	0.156	0.236

C. Point Spread Function

The selected point sources (see §IV.B) were used to study the ISSA point spread function (PSF). The full widths at half maximum (FWHM) of these point sources were measured from ISSA data which had been interpolated to 0.15′ sample spacing using a sinc function of 1.5′ period apodized with a cosine to a full width of 12 zero crossings. Contour plots of interpolated point spread functions are shown in Figures IV.C.1(a)–(d). Note that there is some noncircularity evident. The short axes of the PSFs, when discernible, line up with the predominant scan direction. Table IV.C.1 lists the measured FWHMs of the point spread functions in both the long and short dimensions. These measurements indicate that the resolution of the ISSA is 4′ to 5′, depending on the orientation of the long axis of the image. This spatial resolution is consistent with expectations based on the binning algorithm used to produce the ISSA images.

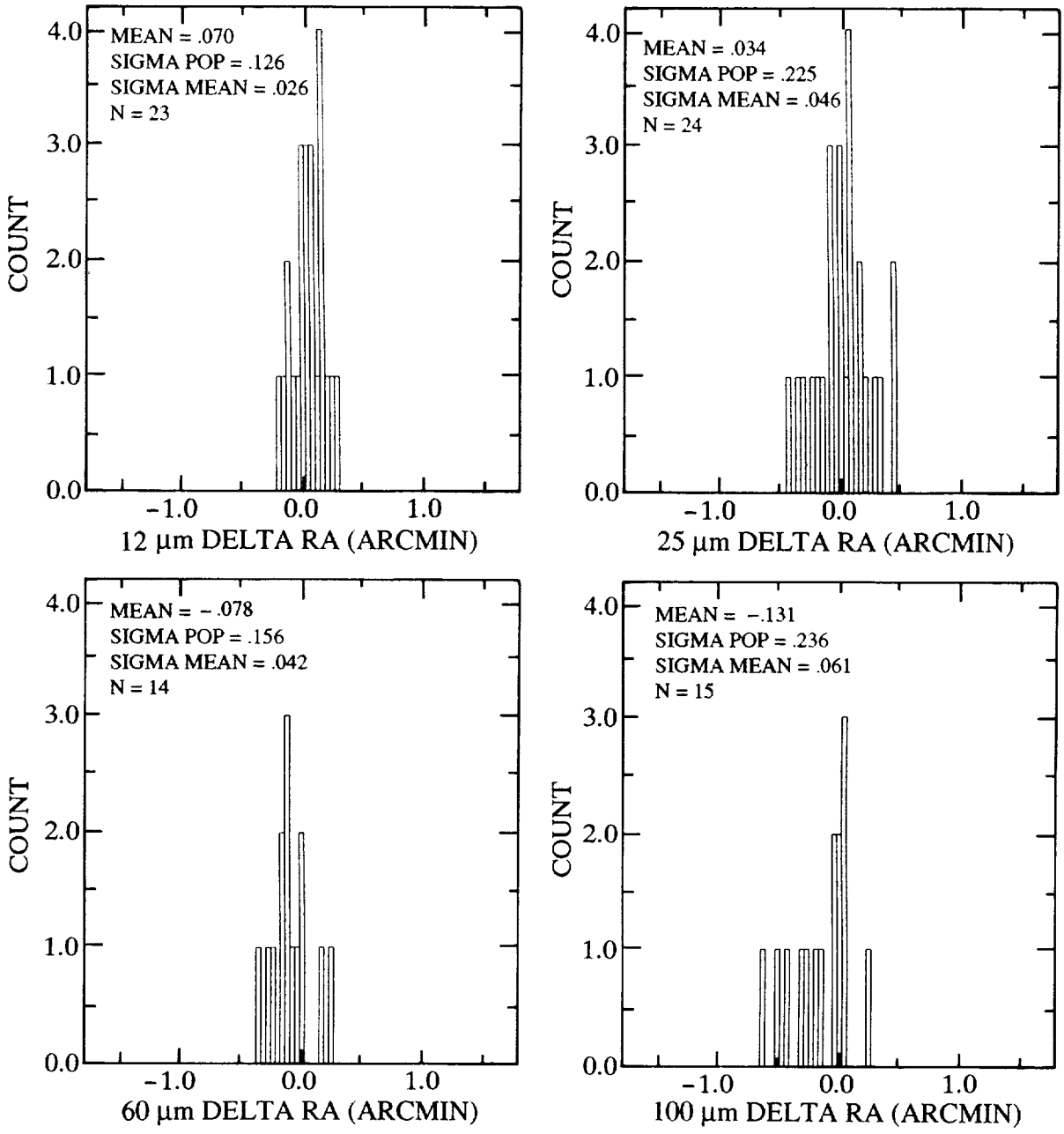

Figure IV.B.1(a) Histograms of Position Differences in RA Between PSC and ISSA

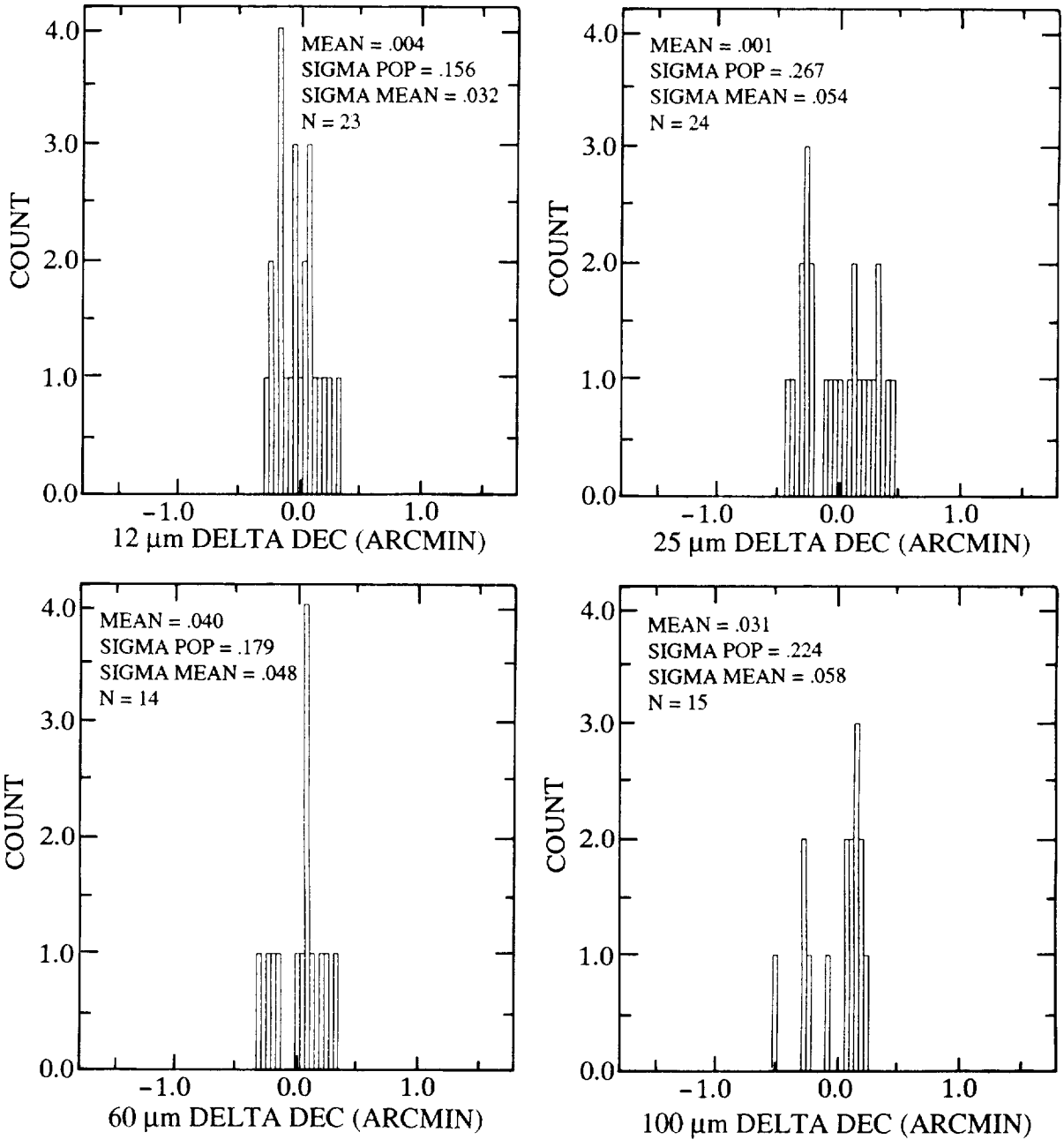

Figure IV.B.1(b) Histograms of Position Differences in DEC Between PSC and ISSA

Table IV.C.1
Point Spread Function Dimensions

	IRAS Name	field	flux (Jy)	FWHM (arcmin)
12 μm	10521+7208	414	35.6	3.7 × 4.8
	15448+3828	355	37.0	3.7 × 4.9
	17133+3651	357	48.2	3.6 × 5.3
	05174-3345	102	27.3	3.6 × 4.7
	03040-8013	3	26.2	3.6 × 4.7
25 μm	20427-8243	9	12.6	3.6 × 4.6
	01452-8026	3	20.8	4.5 × 4.9
	17329+5359	383	21.4	3.6 × 5.3
	04330-6307	28	12.1	3.5 × 3.9
	02238-5947	26	12.1	3.8 × 4.6
60 μm	08354+2555	316	24.3	3.7 × 4.2
	00163-1039	162	6.9	2.7 × 3.9
	04315-0840	169	33.5	3.5 × 4.6
	23488+2018	270	17.0	3.2 × 5.2
100 μm	13183+3423	322	24.4	4.5 × 4.8
	10565+2448	319	14.3	4.6 × 5.2
	23488+2018	270	21.0	5.2 × 6.1
	09320+6134	397	20.1	4.8 × 5.2

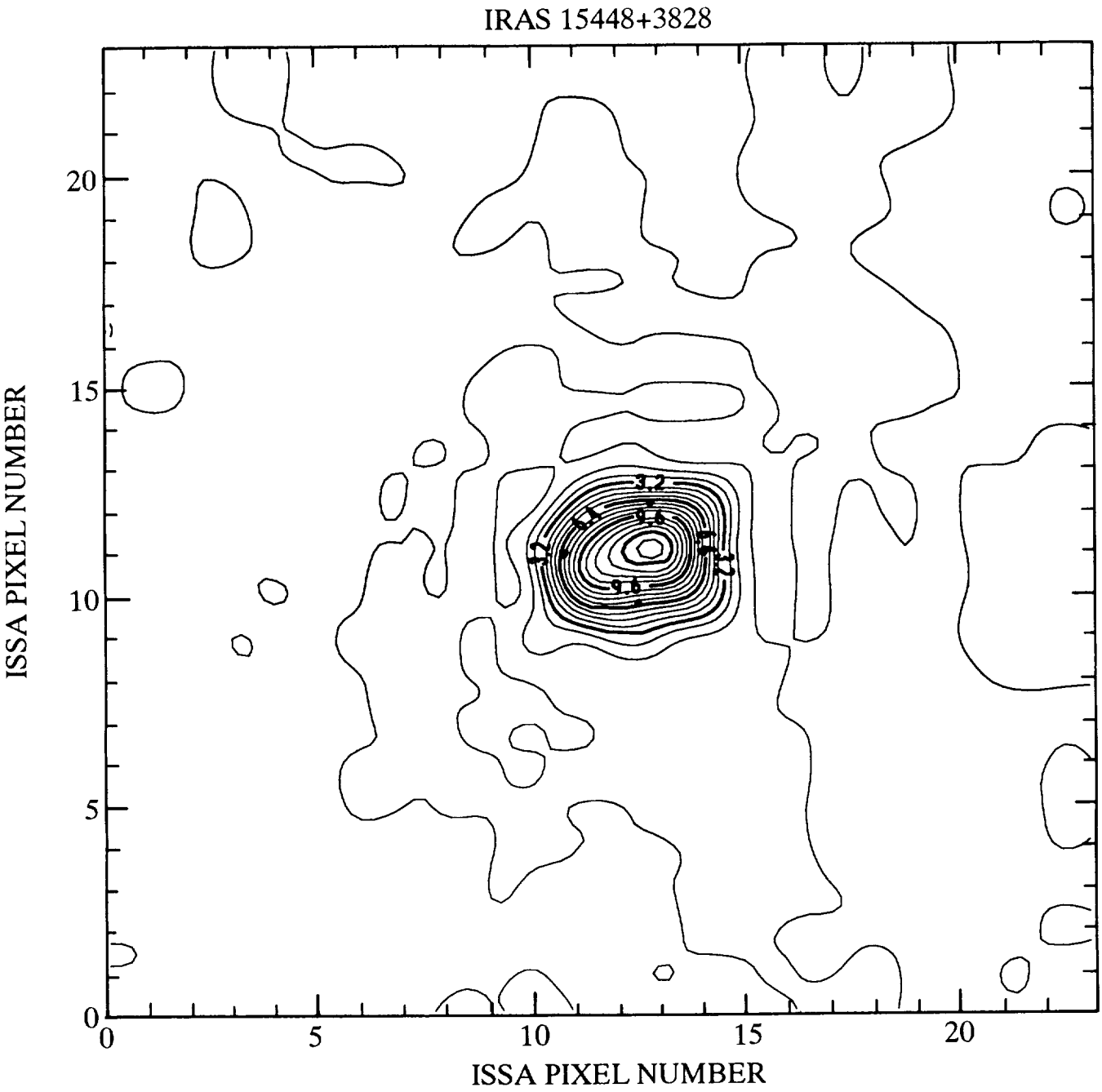

Figure IV.C.1(a) Contour Plot of Point Spread Function for a 12 μm Source, Contoured from 0.0 to 13.6, Interval 0.8

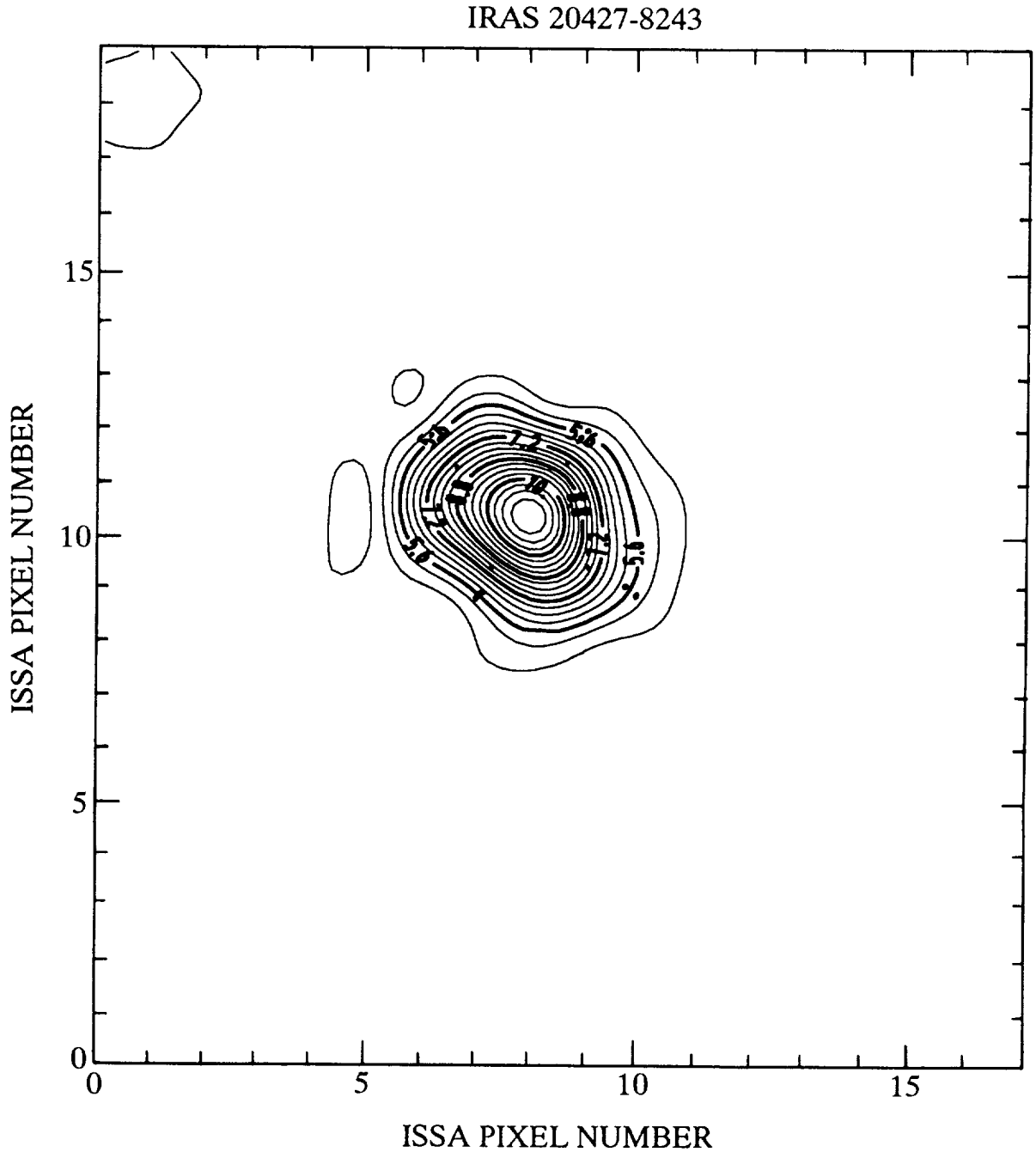

Figure IV.C.1(b) Contour Plot of Point Spread Function for a 25 μm Source, Contoured from 4.0 to 11.6, Interval 0.4

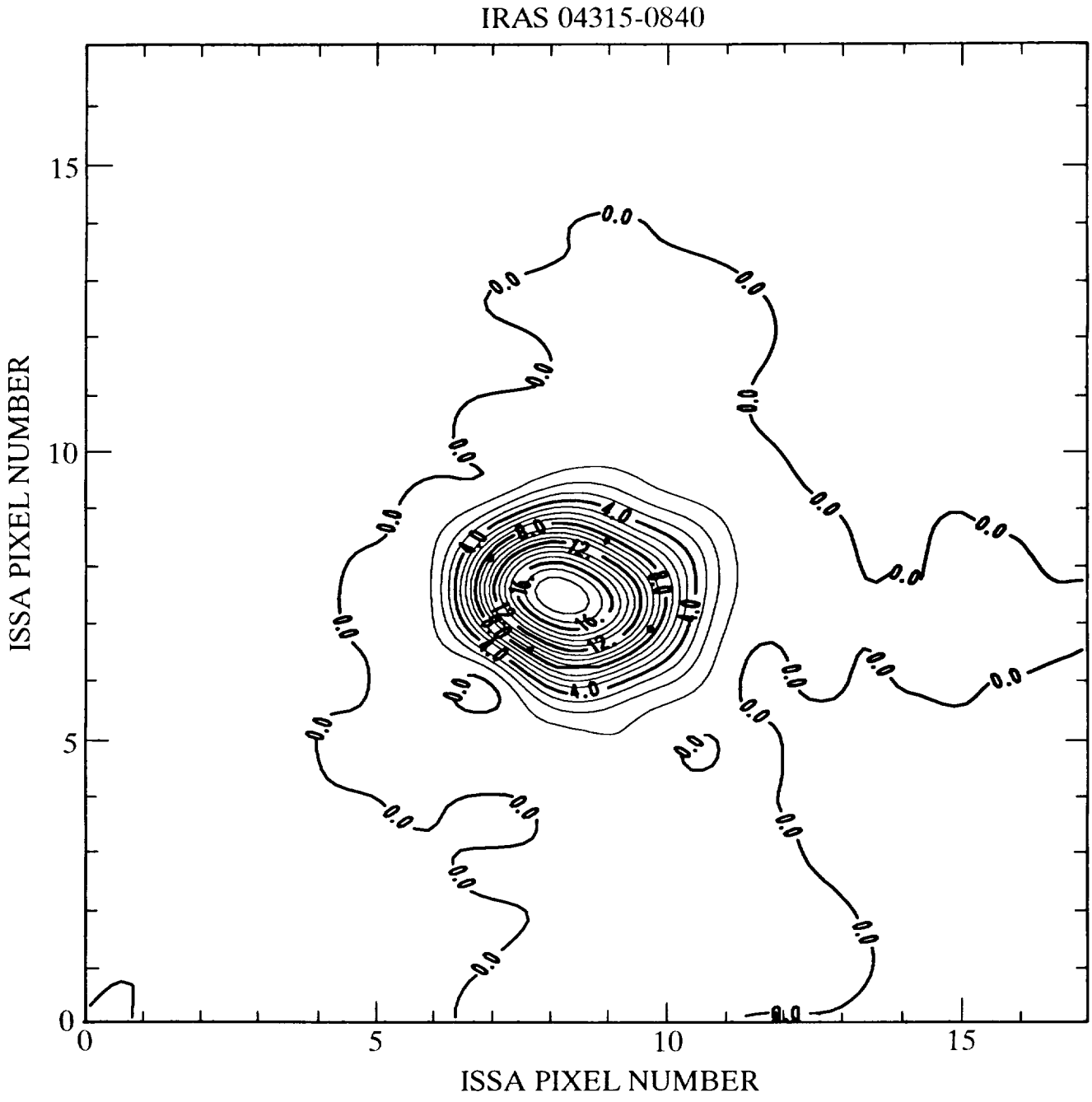

Figure IV.C.1(c) Contour Plot of Point Spread Function for a 60 μm Source, Contoured from 0.0 to 18.0, Interval 1.0

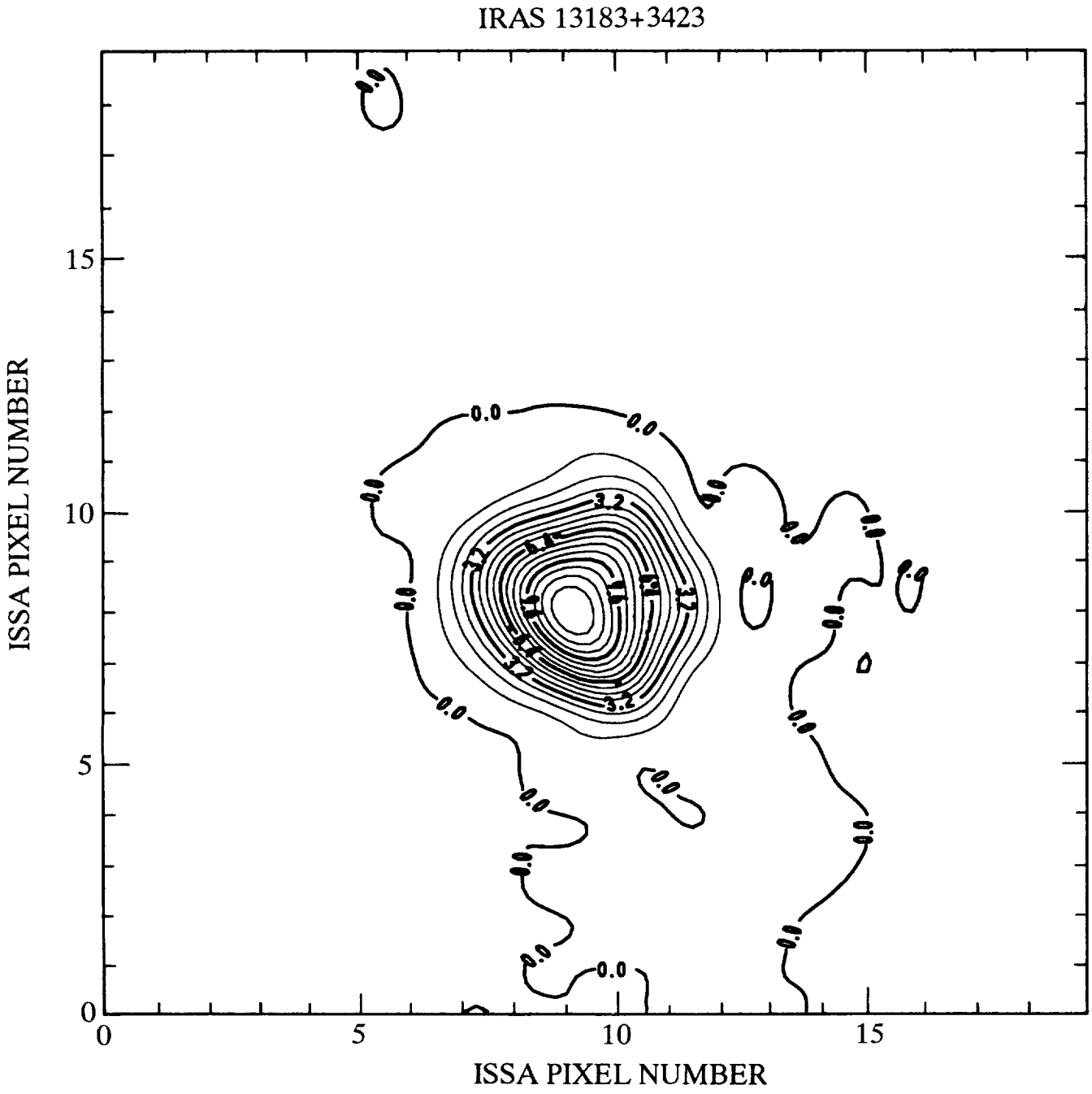

Figure IV.C.1(d) Contour Plot of Point Spread Function for a 100 μm Source, Contoured from 0.0 to 12.0, Interval 0.8

D. Photometric Consistency

The ISSA images were checked to verify their photometric consistency with other IRAS data products; namely, the *IRAS Point Source Catalog* and the *IRAS Zodiacal History File* (ZOHF) (Appendix H). Preparation of the ISSA maps from the IRAS survey scan data was a complex process involving removal of variable zodiacal emission, readjustment of zero points, projection and resampling of the scan data into the ISSA maps and averaging the several survey sky coverages together. Many opportunities to disturb the calibration of the data presented themselves.

Comparison of the IRAS calibration to other measurements is a separate issue and is briefly addressed in §IV.D.3. No adjustments were made to the IRAS photometric calibration based on the results from these comparisons.

D.1. *Point Sources*

Whereas the ISSA is not designed for efficient analysis of celestial point sources, the filter used to smooth the full resolution IRAS data to effectively 2′ samples for the ISSA input data conserves the point source flux to within 10%. Since the basic calibration of the IRAS data is based on point source measurements, testing the fidelity of the reproduction of *IRAS Point Source Catalog* fluxes in ISSA is an important check on the calibration consistency of ISSA. Point sources for analysis were the same as for position accuracy (§IV.B) and are listed in Table IV.B.1. The integrated flux densities of the selected point sources were measured within circular apertures ranging in size from 2.5′ to 9′ radius using an annular area from the outer radius of the measuring aperture to a radius of 10′ as a background reference. The appropriate AC/DC factor was applied to the extracted point source fluxes (§II.B.2). Plots of the PSC flux vs. the AC-adjusted ISSA flux were made for each aperture size and each wavelength. Fits to the data give the ratio of ISSA flux density to PSC flux density for each aperture size. A plot of the ISSA/PSC flux density ratio vs. aperture size gives the encircled flux density as a function of aperture size for the ISSA data. Assuming a Gaussian shape for the ISSA PSF, the flux density ratio should flatten to a value of 1.00 at an aperture diameter about 3.1 times the FWHM of the ISSA point spread function.

Figures IV.D.1 and IV.D.2 display the plots and the encircled flux density curves for the four ISSA wavelengths. The shape of the encircled flux density curve is consistent with the measured size of about 4.5′ (FWHM) for the ISSA point spread function. A circular Gaussian PSF would have 90% encircled flux density at a radius of 1.1 times its FWHM. The level of the flat portion of the curve gives the ratio of ISSA to PSC flux densities as $1.11 \pm .09$ at 12 μm, $1.05 \pm .10$ at 25 μm, $0.92 \pm .05$ at 60 μm and $0.93 \pm .05$ at 100 μm. Two known effects contributing to this difference are point source tails at 12 and 25 μm, which add about 6% to the flux within a 7′ radius aperture, and noise induced by the convolution filter, about 4%, which was used to resample the full resolution IRAS data to 2′ samples (Appendix B). The 60 and 100 μm ISSA fluxes are less than 1 by about 1.5σ. We know of no reason why they should be less than 1.

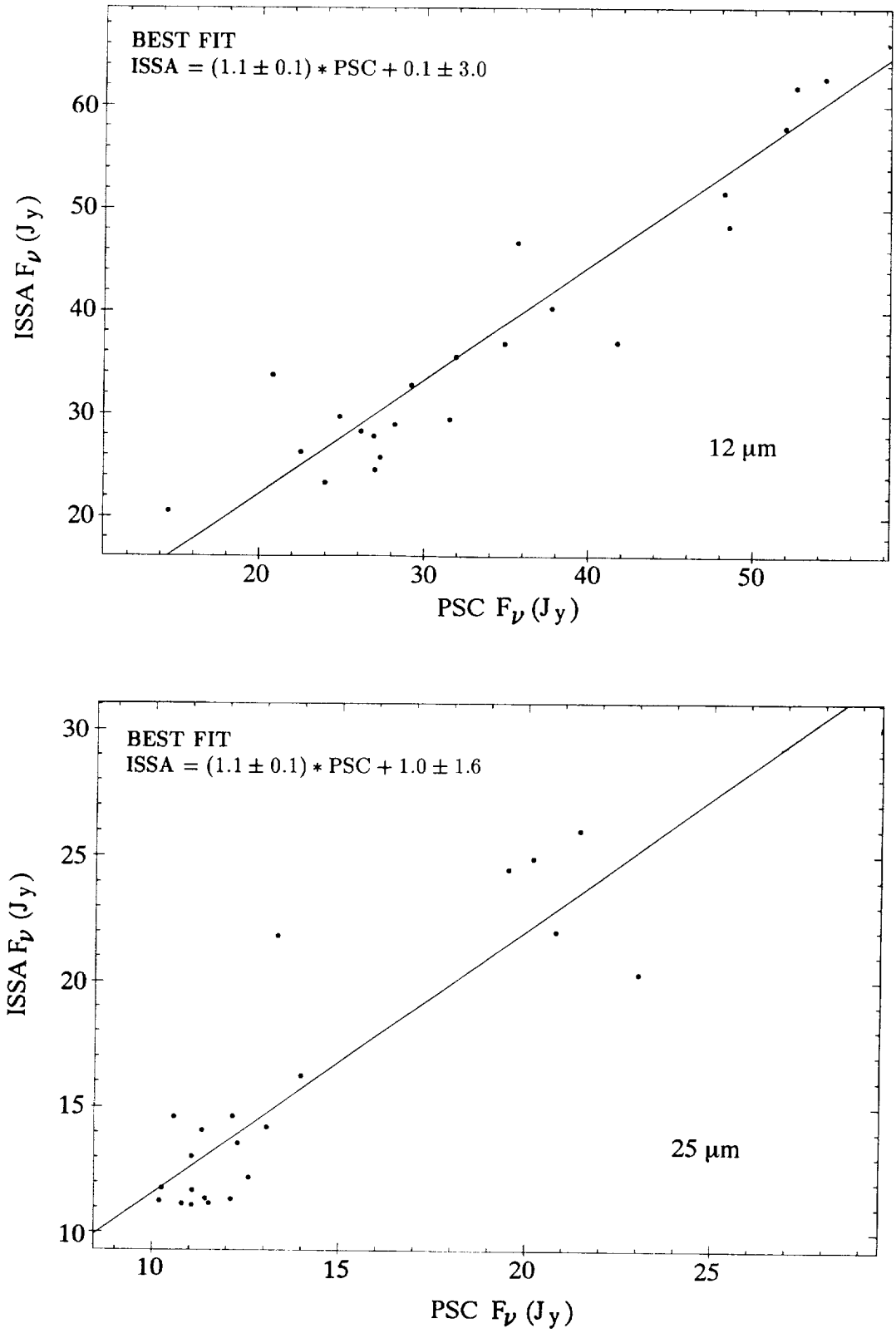

Figure IV.D.1 Scatter Plots of PSC vs. ISSA Point Source Fluxes Measured with a 9′ Aperture (continued next page)

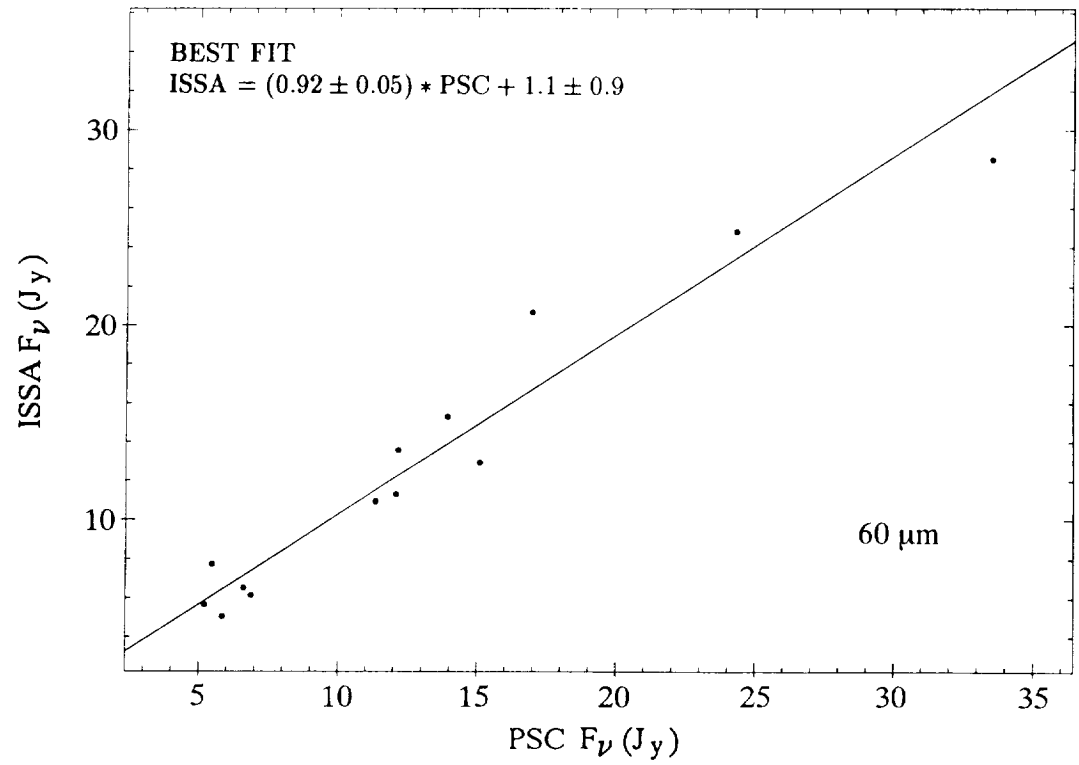

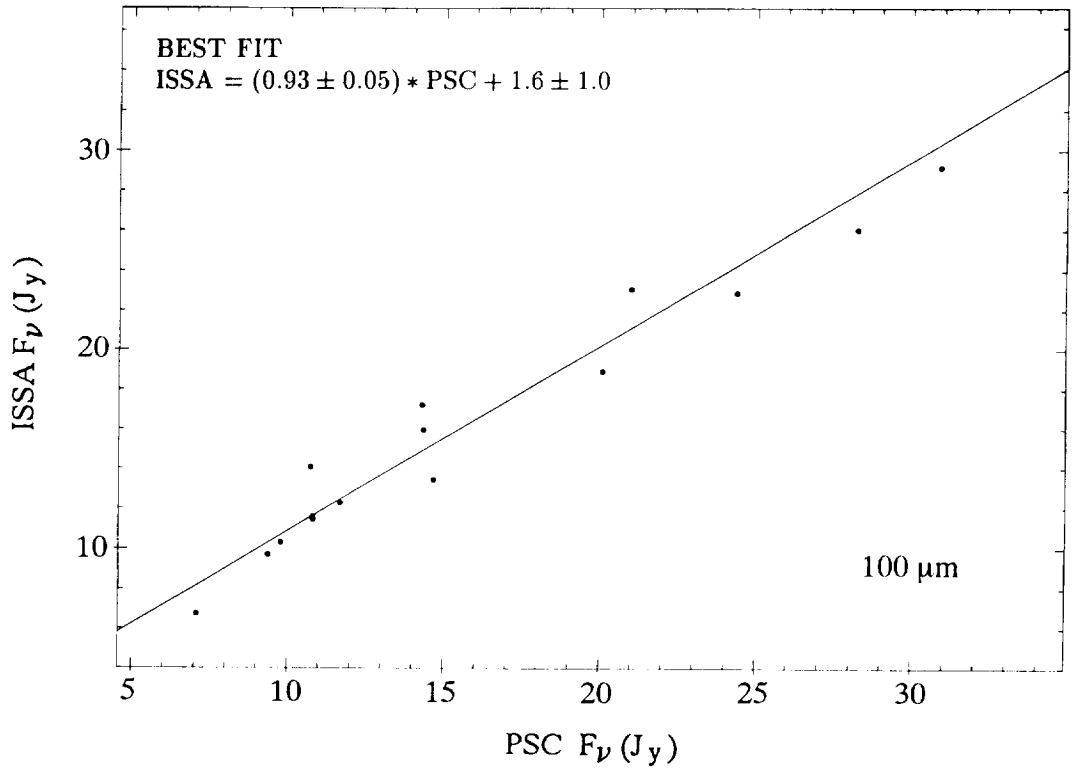

Figure IV.D.1 (cont'd) Scatter Plots of PSC vs. ISSA Point Source Fluxes Measured with a 9′ Aperture

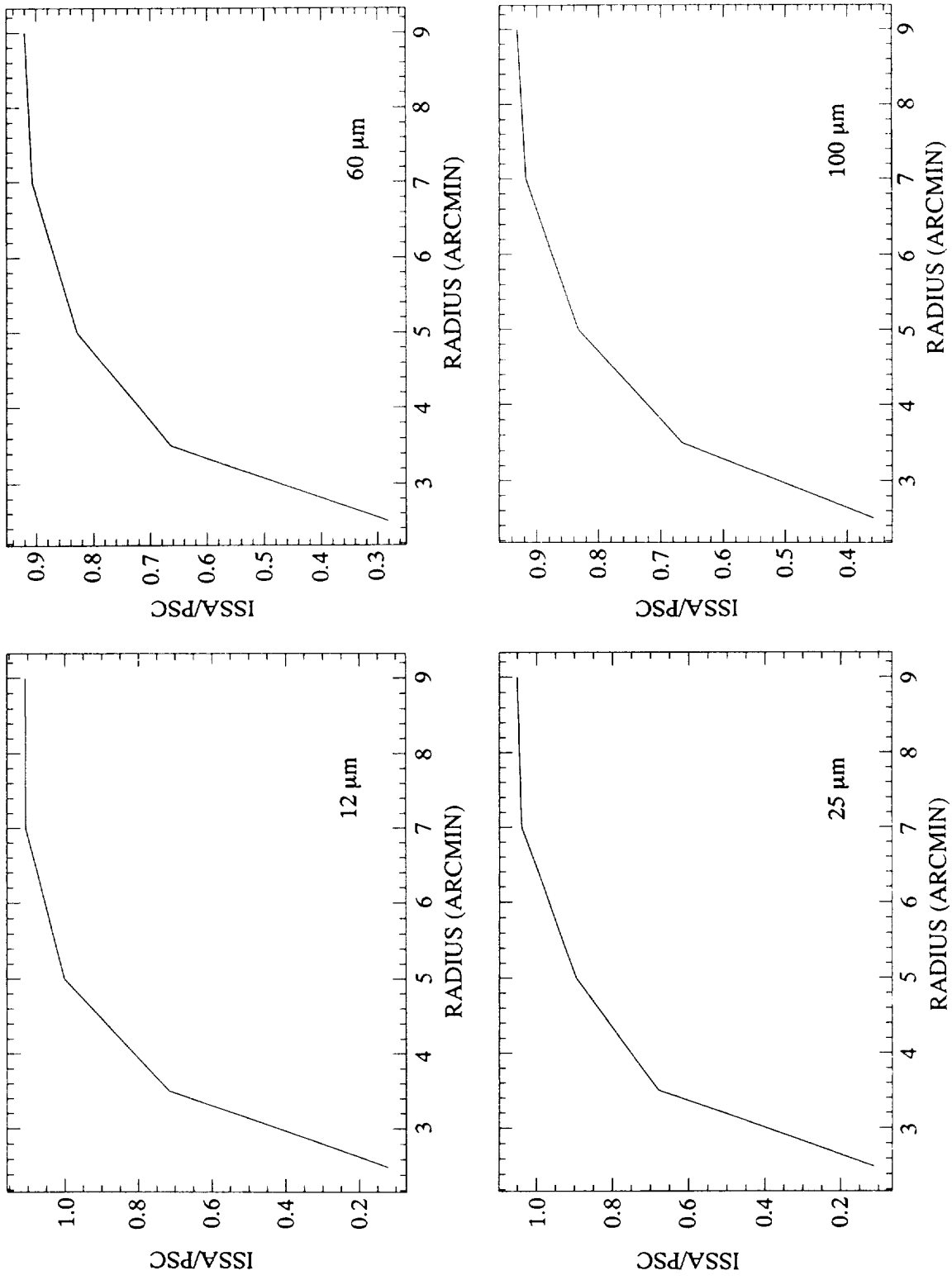

Figure IV.D.2 Flux Density vs. Aperture Diameter. Reference Diameter was 10′

D.2. *Extended Sources*

ISSA extended source photometric consistency was checked by comparing ISSA data smoothed to approximately 1° resolution to a version of the *IRAS Zodiacal History File* (ZOHF) from which the ISSA zodiacal light model (see Appendix G) was removed. The ZOHF is the time-ordered record of the entire IRAS survey in which all the detector signals in each band were averaged to synthesize a 0.5° × 0.5° square beam. The ZOHF includes all calibration and pointing improvements used in producing the ISSA and is the best estimate of the absolute sky surface brightness made by IRAS. ISSA and the ZOHF were derived from the same set of IRAS measurements calibrated and processed in the same way up to the point of averaging the ZOHF to a 0.5° beam and removing the zodiacal emission model from the ISSA data. If the ISSA zodiacal emission model is removed from the ZOHF data and the ISSA data are smoothed to ZOHF resolution the resulting brightness should be the same.

Comparison with the ZOHF reveals the effects of the ISSA destripers and binner at spatial scales larger than about 1°. No cross-check of the ISSA data was possible at spatial scales between 1° and 5′. ISSA and the ZOHF were compared by preparing all-sky maps with both data sets and producing scatter plots of a pixel by pixel correlation of the two maps. The maps used the Aitoff projection in Galactic coordinates with 0.5° × 0.5° square pixels at the projection center. The ZOHF has a 0.5° × 0.5° square beam and required no additional averaging to produce the map. ISSA data were smoothed to a 0.5° circular beam before binning into the Aitoff map. Both the ZOHF and ISSA maps were further smoothed by convolution with a 1.5° × 1.5° rectangle function to reduce differences in the point spread functions. The comparison was done with the first ISSA release which covered only the high-ecliptic-latitude, $|\beta| > 50°$, sky.

Plots of the ISSA vs. ZOHF were produced for the northern cap of the ISSA map. Trend lines were fit subjectively to the data, with care being taken to assure that the overwhelming number of low surface brightness points would not bias the trend line away from the data at high surface brightness. The slopes of the best-fit trend lines for the data are 0.99 ± .01, 0.98 ± .01, 0.97 ± .02 and 1.00 ± .02 for the 12, 25, 60 and 100 μm data, respectively.

The slopes from the data indicate that calibration scale factors of ISSA and the ZOHF are the same to within 2% at all IRAS wavelengths. The destriping and binning procedures used in ISSA production had little or no effect on the gain calibration of the data. Examination of the polar mosaics revealed no evidence of field boundary discontinuities larger than 0.1 MJy sr^{-1}, indicating satisfactory performance of the local destriper.

D.3 *Absolute Photometry*

Checks on the IRAS absolute calibration, which sets the ISSA absolute photometry, generally must be done against other space-based measurements. A few such checks are possible. The Zodiacal Infrared Project (ZIP) (Murdock and Price, 1985) measured the zodiacal light in 15 spectral bands between 2 and 30 μm with a rocket-borne instrument. Comparison of IRAS and ZIP data at 12 and 25 μm showed the same shape for zodiacal

emission but the ZIP observations are a factor of about 1.5 dimmer than IRAS. This discrepancy remains unresolved.

The Diffuse Infrared Background Experiment (DIRBE) on the Cosmic Background Explorer satellite (COBE) has made absolute surface brightness measurements of the sky in a 0.7° square beam at wavelengths from 1.3 μm to 240 μm (Hauser *et al.*, 1991). Since the IRAS mission was primarily designed to measure point sources and DIRBE was primarily designed for measuring extended emission, we believe the COBE-DIRBE calibration is valid and the DIRBE results provide a check on the large-scale performance of IRAS. The COBE/DIRBE Explanatory Supplement (19 July 1993) presents a preliminary linear transformation between IRAS and DIRBE data, which is shown in Table IV.D.1 below. This linear transformation was derived based on carefully selected DIRBE data compared to IRAS (HCON-1 and HCON-2) scan data. The constants given below are average values for the duration of HCON-1 and HCON-2. The transformations are applicable to spatial scales on the order of an IRAS scan but there is *no certainty as to their applicability at smaller spatial scales down to* 0.7°. The IRAS point source calibration is *not* affected by these numbers.

The offset term is relevant to the total intensity IRAS product, the *IRAS Zodiacal History File* (ZOHF). It is *not* applicable to the ISSA since the zodiacal emission was subtracted. See Appendix G for details on the zodiacal model. The offset term is known to have a systematic variation with time at 12 and 25 μm. The offsets given below are simply mean values and do not reflect this trend. The user should refer to the COBE-DIRBE Explanatory Supplement to better understand the offsets at 12 and 25 μm.

The gain term is applicable to both the ISSA and the ZOHF and shows the IRAS measurements at 60 and 100 μm were too bright relative to DIRBE at large spatial scales. There is *no* simple prescription for unraveling the varying spatial response of the detectors to effect a more accurate calibration for the ISSA images. The data given in Table IV.D.1 are representative of the comparison of IRAS HCON-1 and HCON-2 scans with DIRBE data based on the current DIRBE calibration. The gains at 12 and 25 μm are consistent with IRAS. The IRAS brightness appears to be 13% and 28% high at 60 μm and 100 μm, respectively. The 60/100 μm color is about 12% too low in IRAS data relative to DIRBE data.

Table IV.D.1
IRAS-DIRBE Transformation

I(DIRBE) = Gain × I(IRAS) + Offset			
Wavelength (μm)	Gain	Offset (MJy sr^{-1})	Fractional Effect*
12	1.06 ± 0.02	-0.48 ± 0.43	$-.04 \pm .03$
25	1.01 ± 0.02	-1.32 ± 0.74	$-.06 \pm .03$
60	0.87 ± 0.05	$+0.13 \pm 0.65$	$+.02 \pm .08$
100	0.72 ± 0.07	-1.47 ± 0.88	$-.15 \pm .09$

* Ratio of offset to IRAS derived average brightness at north ecliptic pole (Table III.A.1).

E. Noise Performance and Sensitivity

Six major sources contribute to the noise in the ISSA data. Detector noise plus photon noise constitute random noise; natural variations in the celestial background contribute confusion noise; drifts in the calibration of the data produce stripe noise; residual zodiacal emission contains gradients and steps; and nonconfirming sources and radiation spikes introduce spurious point sources. The effects of nonconfirming sources and methods for eliminating them are discussed in §I.D.4. Confusion noise in the IRAS data is discussed in Gautier *et al.*, (1992). The remaining noise sources were measured and analyzed as described below to give the user of ISSA an idea of the sensitivity limits of the ISSA data and of the kinds of errors to expect in the data.

The remaining calibration or stripe noise falls into two spatial domains. Variations over several degrees in the scan direction are discussed in §IV.D.2 in terms of large- and medium-scale baseline distortions. Calibration imperfections produce scan-to-scan and detector-to-detector variations in the images. The RMS stripe noise is measured by examining the variations perpendicular to the scan direction. The performance of the ISSA destripers in reducing this noise is detailed in the section below on cross-scan vs. in-scan noise. Random variations due to electronic noise and photon noise set the noise floor and determine the ultimate sensitivity of ISSA as described in the discussion of noise-equivalent surface brightness density (NESB) and dimmest detectable sources. Finally the magnitude and character of the residual zodiacal emission is discussed.

E.1 *Cross-Scan vs. In-Scan Noise*

One of the performance goals of the ISSA destriping procedure was to reduce the cross-scan noise to the same level as the in-scan noise. This goal was substantially achieved. Table IV.E.1 shows typical values for a coadded image of the RMS variation along a $\sim 1^\circ$ cut taken in the cross-scan and in-scan directions. These cuts were confined to flat, low signal regions within each image. Values for the individual HCONs are about 1.6 times higher. There remains a difference in the spatial power spectrum of the noise in the two directions. The in-scan noise spectrum is characteristic of the noise spectrum of an individual IRAS detector. This spectrum is characterized by a power law with a spectral index near -0.75 and contains little power at frequencies near the resolution limit of ISSA. In contrast, the cross-scan spectrum contains substantial power at frequencies up to the free spectral range of the ISSA data at $(3')^{-1}$, because the cross-scan noise is caused by variations between adjacent detectors whose noises are uncorrelated. This difference in spectral distribution leaves stripe-like features in the residual noise, because the period of the noise variation is much longer in the in-scan direction than in the cross-scan direction. The RMS variation over a few degrees is nearly the same in the two directions, however.

E.2 *Noise Equivalent Surface Brightness in ISSA*

Noise equivalent surface brightness (NESB), actually brightness density here, is conveniently expressed in units of Jy $\mathrm{sr}^{-1}\mathrm{sr}^{-0.5}$. Then, for instance, the expected minimum detectable surface brightness for an object of size Ω sr can be calculated as NESB$\sqrt{\Omega}$. NESBs for the ISSA images can be estimated from Table IV.E.1 assuming that the ap-

Table IV.E.1
In-Scan vs. Cross-Scan Noise in ISSA Field 398

	Cross-Scan (MJy sr^{-1})	In-Scan (MJy sr^{-1})
12 μm	0.045	0.033
25 μm	0.048	0.044
60 μm	0.042	0.036
100 μm	0.080	0.063

propriate solid angle is that of the 90% encircled energy contour of the ISSA point spread functions (about 2.4×10^{-6}sr). This calculation yields 51, 68, 56 and 97 Jy $sr^{-1}sr^{-0.5}$ for the 12, 25, 60 and 100 μm bands, respectively. In areas similar to those where the data for Table IV.E.1 was taken, the dimmest discernible features with size about 0.5° have surface brightness above the background of about 0.02 MJy sr^{-1} at 12, 25 and 60 μm and about 0.07 MJy sr^{-1} at 100 μm. Assuming that "dimmest discernible" means about a 3σ detection these dimmest surface brightnesses are consistent with the estimates above except at 100 μm where the higher general cirrus brightness makes selection of features as dim as 3σ more difficult. The estimates of NESB based on Table IV.E.1 are in agreement with estimates based on the average IRAS detector NEFDs shown in Figure IV.A.1 of the Main Supplement.

E.3 *Residual Zodiacal Emission*

Residual zodiacal emission causes gradients and sharp discontinuities in the ISSA images. Discontinuities can occur when adjacent regions of sky were observed at very different zodiacal brightnesses. These discontinuities are small, as seen in Table IV.E.2, but are easily identified because their boundaries are very sharp and align in the scan direction. Residual zodiacal gradients are more subtle and can be harder to detect. The residual gradients in the high-ecliptic-latitude ISSA data are most apparent near the ecliptic poles in the 12 and 25 μm bands. The magnitude of the residual emission is largest compared to other celestial emission at the shorter wavelengths. The spatial scale of variation is small near the poles due to the combination of scanning geometry and modeling errors in the variation of polar brightness with the motion of the Earth in its orbit. Measurements of some prominent residual zodiacal gradients are given in Table IV.E.3.

E.4 *Quality Estimates from Scan-to-Scan Statistics*

Noise and variability statistics were kept for each pixel during the ISSA map generation process. These noise maps were originally intended for use with a confirmation algorithm that failed because the variation of data within a pixel was extremely non-Gaussian. This was presumably caused by zero-point variation from scan to scan due to systematic errors in the zodiacal emission model. As a result, the pixel statistics did not reveal much about the actual noise levels in the ISSA data.

Table IV.E.2
Residual Zodiacal Emission Discontinuities

Field	12 μm (MJy sr^{-1})	25 μm (MJy sr^{-1})
376	0.3	0.5
397	0.2	0.7
352	0.3	0.4
404	0.5	0.8
341	1.2	2.4
175	0.4	0.5
012	0.6	1.0
133	0.6	1.1
024	0.3	0.7

Table IV.E.3
Residual Zodiacal Emission Gradients

Field	12 μm (MJy sr^{-1}rad^{-1})	25 μm (MJy sr^{-1}rad^{-1})
352	2.6	2.4
381	3.0	2.3
382	3.2	5.2

F. ISSA Reject Set Background Analysis

The *ISSA Reject* images, covering the part of the sky within 20° of the ecliptic plane, are of reduced quality compared to the rest of the ISSA data. The zodiacal dust bands and residuals from the removal of the broad zodiacal emission make significant contributions to the ISSA surface brightness at low ecliptic latitudes, especially at 12 and 25 μm, and can interfere with photometry. This section presents some measures of the magnitude of the problems that might be encountered while using the *ISSA Reject* data for photometric measurements and gives some suggestions for background estimation techniques to minimize photometric problems. *The user is advised to read this section carefully prior to using the ISSA Reject images.*

The magnitude of photometric error which might be encountered during the use of the *ISSA Reject Set* was estimated by processing the reject images with special first and second derivative filters that simulate the procedure of background subtraction in aperture photometry measurements with the ISSA images. In these procedures the background to be subtracted from the object plus background measurement is typically derived from one or more measurements of the sky near the object of interest. If the background is not perfectly flat and featureless this method does not give a perfect background subtraction. If a single background measurement is used, the residual background will be proportional to the first derivative of the background. Similarly, if two symmetrically placed background

measurements are made, the residual will be proportional to the second derivative of the background.

The special feature of the derivative filters used for this error estimation is that the derivative was combined with a boxcar average to pixel sizes of 0.5° and 2.0°. The 0.5° and 2.0° pixel sizes are appropriate for background measurements taken about 0.5° and 2.0° away, respectively. These two separations were chosen to cover approximately the range of separations that might be used in actual practice. The derivatives were taken in two directions, perpendicular to and parallel to the ecliptic plane, since residual zodiacal emission in the reject fields is seen to produce bands roughly parallel to the ecliptic plane. The kernels for the two derivative filters were

$$\begin{pmatrix} 0 & 0 & 0 \\ 0 & -1 & 0 \\ 0 & 1 & 0 \end{pmatrix}$$

for the perpendicular derivative and

$$\begin{pmatrix} 0 & 0 & 0 \\ 0 & -1 & 1 \\ 0 & 0 & 0 \end{pmatrix}$$

for the parallel derivative. The second derivative was obtained by application of the filter twice. These derivative filters were applied to ISSA data that had been reprojected into ecliptic coordinates with a nongeometric projection in which longitude runs linearly with pixel number in one direction and latitude runs linearly with pixel number in the other direction. This projection has the effect of underestimating the derivative by the cosine of latitude, a 10% error at 30°.

Tables IV.F.1 through IV.F.4 summarize the results of the uncertainty analysis. The derivatives have been converted to units of residual signal as discussed above for the two methods of background subtraction. The SNR is the ratio of the flux expected from minimum visible cirrus structures to the residual signal. Values for parts of the nonreject ISSA data ($\beta > 20°$ and $-20° > \beta$) are given for comparison. The tabulated values are averages of the absolute value of the background residual over 6° × 6° squares in the projection described above. Compact bright sources generate derivatives of very large absolute value. The use of background references containing such sources should naturally be avoided in actual measurements of the ISSA data, so the averages over the 6° × 6° squares excluded the extreme upper 1% and lower 1% of the samples, or the upper and lower sample in the case of the averages over the 2° pixels. The tables also include the ratio of the flux expected from the minimum visible cirrus structure to the mean absolute residual. The minimum visible cirrus surface brightness is estimated to be 0.1 MJy sr^{-1} at 12 and 25 μm, which gives predicted fluxes of 7.6 Jy and 122 Jy for the 0.5° and 2.0° beams, respectively.

Several useful hints about background subtraction techniques can be read from Tables IV.F.1 through IV.F.4. First, as expected, residual background errors can be up to ten

times worse in the ISSA reject region than at higher ecliptic latitudes in the nonrejected region. Also as expected, two symmetrically placed reference regions provide a better estimate of the background than a single reference. The generally smaller difference between the parallel and perpendicular components of the derivative at high latitudes indicates that the orientation of the placement of the reference apertures is not critical at high ecliptic latitudes. Conversely, the larger difference between components at low latitude, especially at 25 μm, indicate that better background estimates can be expected from references placed at the same latitude as the object of interest. Clearly the optimum placement of reference areas can best be determined from examination of the actual area being measured, both at low and high ecliptic latitude. The banding of the residual zodiacal features parallel to the ecliptic plane will generally favor parallel placement of reference areas at low latitudes.

Table IV.F.1
Parallel Error Analysis
Pixel Size = 0.5°

12 μm

ecl lat	ecl lon	Derivative			
		First		Second	
		Jy*	SNR†	Jy*	SNR†
0	135	3.0	2.5	1.5	5.1
0	0	2.3	3.3	1.7	4.5
−27	135	3.4	2.2	1.8	4.2
−27	0	1.7	4.5	1.3	5.8
27	135	1.8	4.2	1.1	6.9
27	0	2.6	2.9	1.8	4.2

25 μm

ecl lat	ecl lon	Derivative			
		First		Second	
		Jy*	SNR†	Jy*	SNR†
0	135	3.8	2.0	2.1	3.6
0	0	3.3	2.3	1.8	4.2
−27	135	3.5	2.2	1.9	4.0
−27	0	2.4	3.2	1.5	5.1
27	135	1.8	4.2	1.0	7.6
27	0	2.7	2.8	1.6	4.8

* Mean absolute residual for 0.5° pixel over a 6° square area as described in text.

† SNR is the ratio of the flux expected from the minimum visible cirrus structures to the mean absolute residual, see text §IV.F.

Table IV.F.2
Parallel Error Analysis
Pixel Size = 2.0°

12 μm

ecl lat	ecl lon	Derivative			
		First		Second	
		Jy*	SNR†	Jy*	SNR†
0	135	166	0.7	83	1.5
0	0	56	2.2	49	2.5
−27	135	163	0.7	90	1.4
−27	0	32	3.8	22	5.5
27	135	61	2.0	34	3.6
27	0	73	1.7	83	1.5

25 μm

ecl lat	ecl lon	Derivative			
		First		Second	
		Jy*	SNR†	Jy*	SNR†
0	135	151	0.8	100	1.2
0	0	144	0.8	97	1.3
−27	135	195	0.6	168	0.7
−27	0	93	1.3	61	2.0
27	135	76	1.6	68	1.8
27	0	137	0.9	80	1.5

* Mean absolute residual for 2.0° pixel over a 6° square area as described in text.

† SNR is the ratio of the flux expected from the minimum visible cirrus structures to the mean absolute residual, see text §IV.F.

Table IV.F.3
Perpendicular Error Analysis
Pixel Size = 0.5°

12 μm

ecl lat	ecl lon	Derivative			
		First		Second	
		Jy*	SNR†	Jy*	SNR†
0	135	6.1	1.2	1.7	4.5
0	0	6.1	1.2	2.0	3.8
−27	135	1.9	4.0	1.2	6.3
−27	0	1.2	6.3	0.9	8.4
27	135	1.1	6.9	0.7	11.
27	0	2.5	3.0	1.5	5.1

25 μm

ecl lat	ecl lon	Derivative			
		First		Second	
		Jy*	SNR†	Jy*	SNR†
0	135	17.5	0.4	5.0	1.5
0	0	16.8	0.5	5.7	1.3
−27	135	2.3	3.3	1.1	6.9
−27	0	1.7	4.5	1.1	6.9
27	135	1.5	5.1	0.5	15.
27	0	2.9	2.6	1.6	4.8

* Mean absolute residual for 0.5° pixel over a 6° square area as described in text.

† SNR is the ratio of the flux expected from the minimum visible cirrus structures to the mean absolute residual, see text §IV.F.

Table IV.F.4
Perpendicular Error Analysis
Pixel Size = 2.0°

12 μm

ecl lat	ecl lon	Derivative			
		First		Second	
		Jy*	SNR†	Jy*	SNR†
0	135	297	0.4	188	0.6
0	0	341	0.4	210	0.6
−27	135	88	1.4	34	3.6
−27	0	32	3.8	14	8.7
27	135	36	3.4	16	7.6
27	0	71	1.7	46	2.7

25 μm

ecl lat	ecl lon	Derivative			
		First		Second	
		Jy*	SNR†	Jy*	SNR†
0	135	1050	0.1	682	0.2
0	0	1100	0.1	707	0.2
−27	135	134	0.9	58	2.1
−27	0	80	1.5	22	5.5
27	135	58	2.1	21	5.8
27	0	85	1.4	54	2.3

* Mean absolute residual for 2.0° pixel over a 6° square area as described in text.

† SNR is the ratio of the flux expected from the minimum visible cirrus structures to the mean absolute residual, see text §IV.F.

V. FORMATS FOR THE IRAS SKY SURVEY ATLAS (ISSA)

The *IRAS Sky Survey Atlas*, ISSA, and the *ISSA Reject Set* are machine-readable images in Flexible Image Transport System (FITS) (Wells, D.C. *et al.* 1981) image format. Each 500 × 500-pixel image covers a 12.5° × 12.5° field of sky with pixel size of 1.5′. For each field and wavelength, intensity images were produced for separate HCONs plus the co-add of all HCONs. Coverage and standard deviation images were also produced and can be obtained from IPAC by special request.

FITS image format restrictions require that image samples be either 16 or 32 bits. The dynamic range of the intensity values in each ISSA image drove the choice of sample size. The resolution is 5% of median pixel noise. Intensity images are either 0.5 or 1.0 Mbytes. Sample FITS headers for intensity images are shown in Tables V.1 and V.2. Table V.3 provides a brief description of some FITS header keywords.

Table V.1

A Sample FITS Header for Intensity Images:
(4 byte format)

```
SIMPLE  =                    T / STANDARD FITS FORMAT
BITPIX  =                   32 / 4 BYTE TWOS-COMPL INT
NAXIS   =                    3 / # OF AXES
NAXIS1  =                  500 / # SAMPLES PER LINE
NAXIS2  =                  500 / # LINES IN IMAGE
NAXIS3  =                    1 / # WAVELENGTHS
BSCALE  =    2.540508887E-03   / TRUE = TAPE*BSCALE+BZERO
BZERO   =    3.795743940E+02   /
BUNIT   = 'MJY/SR'             / INTENSITY
BLANK   =          -2000000000 / TAPE VALUE FOR EMPTY PIXEL
CRVAL1  =    1.560000000E+02   / RA AT ORIGIN (DEGREES)
CRPIX1  =    2.500000000E+02   / SAMPLE AXIS ORIGIN (PIXEL)
CTYPE1  = 'RA---TAN'           / DECREASES IN VALUE AS SAMPLE
        =                      / INDEX INCREASES (GNOMONIC)
CDELT1  =   -2.500000000E-02   / COORD VALUE INCR DEG/PIXEL
        =                      / AT ORIGIN ON SAMPLE AXIS
CRVAL2  =    7.000000000E+01   / DEC AT ORIGIN (DEGREES)
CRPIX2  =    2.500000000E+02   / LINE AXIS ORIGIN (PIXEL)
CTYPE2  = 'DEC--TAN'           / DECREASES IN VALUE AS LINE
        =                      / INDEX INCREASES (GNOMONIC)
CDELT2  =    2.500000000E-02   / COORD VALUE INCR DEG/PIXEL
        =                      / AT ORIGIN ON LINE AXIS
CRVAL3  =    6.000000000E-05   / WAVELENGTH IN METERS
CRPIX3  =    1.000000000E+00   /
CTYPE3  = 'LAMBDA'             /
CDELT3  =    0.000000000E+00   /
DATAMAX =    7.604891303E+02   / MJY/SR (TRUE VALUE)
DATAMIN =   -1.340342276E+00   / MJY/SR (TRUE VALUE)
EPOCH   =    1.950000000E+03   / EME50
DATE-MAP = '90/11/15'          / MAP RELEASE DATE (YY/MM/DD)
DATE    = '91/10/28'           / DATE TAPE WRITTEN(YY/MM/DD)
ORIGIN  = 'JPL-IPAC'           / INSTITUTION
TELESCOP = 'IRAS'              /
INSTRUME = 'ISSA-FLD'          / IRAS SKY SURVEY ATLAS
OBJECT  = 'f414h003'           / FIELD NUMBER-HCON
PROJTYPE = 'GNOMONIC'          / PROJECTION TYPE
EDITED  =                    T / SCANS EDITED
APPCAL  =                    T / CALIBRATION CORRECTION 25 MICRON
```

Table V.1, continued

```
DE-ZODY  =                    T    / DE-ZODIED IMAGE
GLBL-D   =                    T    / APPLIED GLOBAL PARAMETERS
LOCAL-D  =                    T    / LOCAL DESTRIPER
ASBLANK  =                    T    / ASTEROID BLANKING
COMMENT
COMMENT
COMMENT
COMMENT
COMMENT
COMMENT
COMMENT
END
```

Table V.2

A Sample FITS Header for Intensity Images:
(2 byte format)

```
SIMPLE  =                    T / STANDARD FITS FORMAT
BITPIX  =                   16 / 2 BYTE TWOS-COMPL INT
NAXIS   =                    3 / # OF AXES
NAXIS1  =                  500 / # SAMPLES PER LINE
NAXIS2  =                  500 / # LINES IN IMAGE
NAXIS3  =                    1 / # WAVELENGTHS
BSCALE  =     8.622583455E-05 / TRUE = TAPE*BSCALE+BZERO
BZERO   =     2.175757902E+00 /
BUNIT   = 'MJY/SR'            / INTENSITY
BLANK   =                -32768 / TAPE VALUE FOR EMPTY PIXEL
CRVAL1  =     2.730000000E+02 / RA AT ORIGIN (DEGREES)
CRPIX1  =     2.500000000E+02 / SAMPLE AXIS ORIGIN (PIXEL)
CTYPE1  = 'RA---TAN'          / DECREASES IN VALUE AS SAMPLE
        =                     / INDEX INCREASES (GNOMONIC)
CDELT1  =    -2.500000000E-02 / COORD VALUE INCR DEG/PIXEL
        =                     / AT ORIGIN ON SAMPLE AXIS
CRVAL2  =     4.000000000E+01 / DEC AT ORIGIN (DEGREES)
CRPIX2  =     2.500000000E+02 / LINE AXIS ORIGIN (PIXEL)
CTYPE2  = 'DEC--TAN'          / DECREASES IN VALUE AS LINE
        =                     / INDEX INCREASES (GNOMONIC)
CDELT2  =     2.500000000E-02 / COORD VALUE INCR DEG/PIXEL
        =                     / AT ORIGIN ON LINE AXIS
CRVAL3  =     6.000000000E-05 / WAVELENGTH IN METERS
CRPIX3  =     1.000000000E+00 /
CTYPE3  = 'LAMBDA'            /
CDELT3  =     0.000000000E+00 /
DATAMAX =     4.978097525E+00 / MJY/SR (TRUE VALUE)
DATAMIN =    -6.265817208E+03 / MJY/SR (TRUE VALUE)
EPOCH   =     1.950000000E+03 / EME50
DATE-MAP = '91/05/15'         / MAP RELEASE DATE (YY/MM/DD)
DATE    = '91/10/28'          / DATE TAPE WRITTEN(YY/MM/DD)
ORIGIN  = 'JPL-IPAC'          / INSTITUTION
TELESCOP = 'IRAS'             /
INSTRUME = 'ISSA-FLD'         / IRAS SKY SURVEY ATLAS
OBJECT  = 'f358h001'          / FIELD NUMBER-HCON
PROJTYPE = 'GNOMONIC'         / PROJECTION TYPE
EDITED  =                    T / SCANS EDITED
APPCAL  =                    T / CALIBRATION CORRECTION 25 MICRON
DE-ZODY =                    T / DE-ZODIED IMAGE
GLBL-D  =                    T / APPLIED GLOBAL PARAMETERS
```

Table V.2, continued

```
LOCAL-D  =                    T    / LOCAL DESTRIPER
ASBLANK  =                    T    / ASTEROID BLANKING
COMMENT
COMMENT
COMMENT
COMMENT
COMMENT
COMMENT
COMMENT
END
```

Table V.3

FITS Keywords

Keyword	Description
BITPIX	Indicates number of bits to represent the sample in two's complement. Intensity maps are either 16 or 32 bits per sample. Coverage and standard deviation images are 16 bits per sample.
BUNIT	Intensity and standard deviation of the mean are in MJy sr^{-1}. Coverage images are dimensionless.
BLANK	Value assigned to empty pixels.
DATE	Date the image was made at IPAC.
INSTRUME	Indication that image is an *IRAS Sky Survey Atlas* or *ISSA Reject* product. ISSA-I or ISSA-FLD indicates the ISSA image was processed for the first release in 1991, the $\|\beta\| > 50°$ sky. ISSA-II indicates the ISSA image was processed for the second release, the $\|\beta\| < 50°$ sky. ISSA-REJ indicates the image is part of the *ISSA Reject Set*.
OBJECT	Gives field and HCON number as fxxxhnnn where xxx is a three-digit field number and nnn is either 001,002 or 003 for individual HCON or 000 for the co-add.
CRVAL3	Wavelength in meters.
True/false indicators:	
EDITED	If TRUE, the field had some initial scans edited based on a list of known anomalies.
APPCAL	If TRUE, calibration corrections were applied to the 25 μm detectors.
DE-ZODY	If TRUE, the image has had the zodiacal foreground removed.
GLBL-D	If TRUE, the image has been globally destriped.
LOCAL-D	If TRUE, the image has been locally destriped.
ASBLANK	If TRUE, the image has had asteroids removed from the co-added image

VI. REFERENCES

Aumann H.H. and R.G. Walker 1987, *Astron. J*, **94**, 1088.

Boulanger F. and M. Pérault 1988, *Ap. J.*, **330**, 64.

Dermott, S.F., S. Jayaraman, Y.L. Xu, J.C. Liou 1994, "A circumsolar ring of asteroidal dust in resonant lock with the Earth" Nature (1994, submitted).

DIRBE Explanatory Supplement 19 July 1993, distributed by National Space Science Data Center (NSSDC).

Emerson D.T. and R. Gräve 1988, *Astron. Astrophys.*, **190**, 353.

Gautier T.N., F. Boulanger, M. Perault, J.L. Puget 1992, *Astron. J.*, **103**, 1313.

Hamming R.W. 1977, Digital Filters, Prentice-Hall, Inc., Englewood Cliffs, NJ.

Hauser M.G. *et al.* 1991, "After the First Three Minutes," *AIP Conference Proceedings* 222, (S.S. Holt, C.L. Bennett and V. Trimble, eds.), 161.

IRAS Asteroids and Comet Survey: Explanatory Supplement Preprint Version 1, 1986, ed. D.L. Matson (Pasadena:JPL D–3698 (internal document)).

IRAS Catalogs and Atlases: Explanatory Supplement 1988, ed. C.A. Beichman, G. Neugebauer, H.J. Habing, P.E. Clegg, and T.J. Chester (Washington, D.C.:GPO).

Moshir, M. *et al.* 1992, Explanatory Supplement to the IRAS Faint Source Survey Version 2, JPL D-10015 8/92 (Pasadena:JPL).

Murdock T.L. and S.D. Price 1985, *Astron. J.*, **90**, 375.

Soifer B.T., D.B. Sanders, B.F. Madore, G. Neugebauer, G.E. Danielson, J.H. Elias, C.J. Lonsdale and W.L. Rice 1987, *Ap. J.*, **320**, 238.

Sykes M.V. and R.G. Walker 1992, *Icarus*, **95**, 180.

Wells D.C., E.W. Greisen and R.H. Harten 1981, *Astronomy and Astrophysics Supplement Series*, **44**, 363.

VII. ACKNOWLEDGMENTS

The concept of creating the *IRAS Sky Survey Atlas* from the IRAS data came from the U.S. IRAS Science Team. We acknowledge their guidance throughout this project, as well as their direct efforts in specific aspects. The U.S. IRAS Science Team consists of G. Neugebauer, Chairman, H.H. Aumann, C.A. Beichman, T.J. Chester, T.N. Gautier, F.C. Gillett, M.G. Hauser, G. Helou, J.R. Houck, C.J. Lonsdale, F.J. Low, B.T. Soifer, R.G. Walker, and E.T. Young.

The *IRAS Sky Survey Atlas* is one of the many products of the IRAS Extended Mission funded by NASA. We thank N. Boggess, F.C. Gillett, C. Hartman, C. Pellerin, and G. Riegler of NASA for their support over the last four years.

We thank M.G. Hauser, L.J. Rickard and J. Vrtilek for their assistance in the calibration analysis.

We thank J. Good for the use of his zodiacal model which greatly enhanced the quality of the ISSA images.

We also acknowledge R. Benson for his overall contributions to ISSA and especially for his contributions to the calibration analysis of the IRAS data.

The *IRAS Sky Survey Atlas* would not have been produced in a timely manner and with such high quality without the efforts of the Data Management Team at IPAC. The Data Management Team consists of G. Lairmore (former supervisor), G. Smith (former supervisor), R. Beck, R. Abihai, R. Bailey, D. Engler, E. Erwin, R. Frayre, H. Hanson, G. Johnson, J. Lampley, Leslie Lloyd, P. Lynn, G. Pate, and R. Urban.

The visual verification and quality checking of each *IRAS Sky Survey Atlas* image was performed by G. Johnson. We greatly appreciate her perseverance and hard work in performing this task. The quality of the images reflects the excellence of her work.

The management of the database and the production coordination was performed by R. Beck. We thank him for the valuable skills he brought to this task, for his cooperative spirit and for his patience.

Production of color mosaics and images was performed by G. Laughlin. We thank her for her skill and enthusiasm in creating these pictures.

Other members of the IPAC staff provided important support. D. Wittman and N. Chiu wrote the programs to position order the IRAS database. N. Chiu wrote the programs to convert the data from IBM format into Cyber format. D. Wittman and N. Maksoudian provided systems support. We thank the library staff consisting of R. Scholey, IPAC Librarian and Supervisor, H. Hope, C. Lague, Larry Lloyd, C. Kelley and E. Scholey. We thank C. Lague and H. Hope for maintaining and filing information for the Atlas.

R. Stagner wrote the original software used to produce the resampled, compressed, time-ordered input data. We also thank B. Narron for his valuable inputs and experience in the area of binning and projection algorithms.

We have benefited from those who have used the *IRAS Sky Survey Atlas* images and provided feedback. We would like specifically to thank Drs. M.V. Sykes, W. Rice, S. Terebey and R. Laureijs for their comments.

This supplement was typed in TeX by D. Milton. Her expertise and enthusiasm contributed greatly to the timely production of this document.

APPENDIX A

Center Positions for IRAS Sky Survey Atlas

Field#	RA	DEC	Field #	RA	DEC
1	00h00m,	−90d00m	41	21h32m,	−60d00m
2	00h00m,	−80d00m	42	22h48m,	−60d00m
3	03h00m,	−80d00m	43	00h00m,	−50d00m
4	06h00m,	−80d00m	44	01h00m,	−50d00m
5	09h00m,	−80d00m	45	02h00m,	−50d00m
6	12h00m,	−80d00m	46	03h00m,	−50d00m
7	15h00m,	−80d00m	47	04h00m,	−50d00m
8	18h00m,	−80d00m	48	05h00m,	−50d00m
9	21h00m,	−80d00m	49	06h00m,	−50d00m
10	00h00m,	−70d00m	50	07h00m,	−50d00m
11	01h44m,	−70d00m	51	08h00m,	−50d00m
12	03h28m,	−70d00m	52	09h00m,	−50d00m
13	05h12m,	−70d00m	53	10h00m,	−50d00m
14	06h56m,	−70d00m	54	11h00m,	−50d00m
15	08h40m,	−70d00m	55	12h00m,	−50d00m
16	10h24m,	−70d00m	56	13h00m,	−50d00m
17	12h08m,	−70d00m	57	14h00m,	−50d00m
18	13h52m,	−70d00m	58	15h00m,	−50d00m
19	15h36m,	−70d00m	59	16h00m,	−50d00m
20	17h20m,	−70d00m	60	17h00m,	−50d00m
21	19h04m,	−70d00m	61	18h00m,	−50d00m
22	20h48m,	−70d00m	62	19h00m,	−50d00m
23	22h32m,	−70d00m	63	20h00m,	−50d00m
24	00h00m,	−60d00m	64	21h00m,	−50d00m
25	01h16m,	−60d00m	65	22h00m,	−50d00m
26	02h32m,	−60d00m	66	23h00m,	−50d00m
27	03h48m,	−60d00m	67	00h00m,	−40d00m
28	05h04m,	−60d00m	68	00h52m,	−40d00m
29	06h20m,	−60d00m	69	01h44m,	−40d00m
30	07h36m,	−60d00m	70	02h36m,	−40d00m
31	08h52m,	−60d00m	71	03h28m,	−40d00m
32	10h08m,	−60d00m	72	04h20m,	−40d00m
33	11h24m,	−60d00m	73	05h12m,	−40d00m
34	12h40m,	−60d00m	74	06h04m,	−40d00m
35	13h56m,	−60d00m	75	06h56m,	−40d00m
36	15h12m,	−60d00m	76	07h48m,	−40d00m
37	16h28m,	−60d00m	77	08h40m,	−40d00m
38	17h44m,	−60d00m	78	09h32m,	−40d00m
39	19h00m,	−60d00m	79	10h24m,	−40d00m
40	20h16m,	−60d00m	80	11h16m,	−40d00m

C-2

Field#	RA	DEC	Field #	RA	DEC
81	12h08m,	−40d00m	121*	19h56m,	−30d00m
82	13h00m,	−40d00m	122*	20h42m,	−30d00m
83	13h52m,	−40d00m	123*	21h28m,	−30d00m
84	14h44m,	−40d00m	124*	22h14m,	−30d00m
85*	15h36m,	−40d00m	125	23h00m,	−30d00m
86*	16h28m,	−40d00m	126	23h46m,	−30d00m
87*	17h20m,	−40d00m	127*	00h00m,	−20d00m
88*	18h12m,	−40d00m	128	00h42m,	−20d00m
89*	19h04m,	−40d00m	129	01h24m,	−20d00m
90*	19h56m,	−40d00m	130	02h06m,	−20d00m
91	20h48m,	−40d00m	131	02h48m,	−20d00m
92	21h40m,	−40d00m	132	03h30m,	−20d00m
93	22h32m,	−40d00m	133	04h12m,	−20d00m
94	23h24m,	−40d00m	134	04h54m,	−20d00m
95	00h00m,	−30d00m	135	05h36m,	−20d00m
96	00h46m,	−30d00m	136	06h18m,	−20d00m
97	01h32m,	−30d00m	137	07h00m,	−20d00m
98	02h18m,	−30d00m	138	07h42m,	−20d00m
99	03h04m,	−30d00m	139	08h24m,	−20d00m
100	03h50m,	−30d00m	140	09h06m,	−20d00m
101	04h36m,	−30d00m	141	09h48m,	−20d00m
102	05h22m,	−30d00m	142	10h30m,	−20d00m
103	06h08m,	−30d00m	143	11h12m,	−20d00m
104	06h54m,	−30d00m	144*	11h54m,	−20d00m
105	07h40m,	−30d00m	145*	12h36m,	−20d00m
106	08h26m,	−30d00m	146*	13h18m,	−20d00m
107	09h12m,	−30d00m	147*	14h00m,	−20d00m
108	09h58m,	−30d00m	148*	14h42m,	−20d00m
109	10h44m,	−30d00m	149*	15h24m,	−20d00m
110	11h30m,	−30d00m	150*	16h06m,	−20d00m
111	12h16m,	−30d00m	151*	16h48m,	−20d00m
112*	13h02m,	−30d00m	152*	17h30m,	−20d00m
113*	13h48m,	−30d00m	153*	18h12m,	−20d00m
114*	14h34m,	−30d00m	154*	18h54m,	−20d00m
115*	15h20m,	−30d00m	155*	19h36m,	−20d00m
116*	16h06m,	−30d00m	156*	20h18m,	−20d00m
117*	16h52m,	−30d00m	157*	21h00m,	−20d00m
118*	17h38m,	−30d00m	158*	21h42m,	−20d00m
119*	18h24m,	−30d00m	159*	22h24m,	−20d00m
120*	19h10m,	−30d00m	160*	23h06m,	−20d00m

* ISSA Reject fields.

Field#	RA	DEC	Field #	RA	DEC
161*	23h48m,	−20d00m	201*	02h00m,	+00d00m
162*	00h00m,	−10d00m	202*	02h40m,	+00d00m
163*	00h40m,	−10d00m	203*	03h20m,	+00d00m
164*	01h20m,	−10d00m	204*	04h00m,	+00d00m
165*	02h00m,	−10d00m	205	04h40m,	+00d00m
166	02h40m,	−10d00m	206	05h20m,	+00d00m
167	03h20m,	−10d00m	207	06h00m,	+00d00m
168	04h00m,	−10d00m	208	06h40m,	+00d00m
169	04h40m,	−10d00m	209	07h20m,	+00d00m
170	05h20m,	−10d00m	210*	08h00m,	+00d00m
171	06h00m,	−10d00m	211*	08h40m,	+00d00m
172	06h40m,	−10d00m	212*	09h20m,	+00d00m
173	07h20m,	−10d00m	213*	10h00m,	+00d00m
174	08h00m,	−10d00m	214*	10h40m,	+00d00m
175	08h40m,	−10d00m	215*	11h20m,	+00d00m
176	09h20m,	−10d00m	216*	12h00m,	+00d00m
177*	10h00m,	−10d00m	217*	12h40m,	+00d00m
178*	10h40m,	−10d00m	218*	13h20m,	+00d00m
179*	11h20m,	−10d00m	219*	14h00m,	+00d00m
180*	12h00m,	−10d00m	220*	14h40m,	+00d00m
181*	12h40m,	−10d00m	221*	15h20m,	+00d00m
182*	13h20m,	−10d00m	222*	16h00m,	+00d00m
183*	14h00m,	−10d00m	223	16h40m,	+00d00m
184*	14h40m,	−10d00m	224	17h20m,	+00d00m
185*	15h20m,	−10d00m	225	18h00m,	+00d00m
186*	16h00m,	−10d00m	226	18h40m,	+00d00m
187*	16h40m,	−10d00m	227	19h20m,	+00d00m
188*	17h20m,	−10d00m	228*	20h00m,	+00d00m
189*	18h00m,	−10d00m	229*	20h40m,	+00d00m
190*	18h40m,	−10d00m	230*	21h20m,	+00d00m
191*	19h20m,	−10d00m	231*	22h00m,	+00d00m
192*	20h00m,	−10d00m	232*	22h40m,	+00d00m
193*	20h40m,	−10d00m	233*	23h20m,	+00d00m
194*	21h20m,	−10d00m	234*	00h00m,	+10d00m
195*	22h00m,	−10d00m	235*	00h40m,	+10d00m
196*	22h40m,	−10d00m	236*	01h20m,	+10d00m
197*	23h20m,	−10d00m	237*	02h00m,	+10d00m
198*	00h00m,	+00d00m	238*	02h40m,	+10d00m
199*	00h40m,	+00d00m	239*	03h20m,	+10d00m
200*	01h20m,	+00d00m	240*	04h00m,	+10d00m

* ISSA Reject fields.

Field#	RA	DEC	Field #	RA	DEC
241*	04h40m,	+10d00m	281*	07h42m,	+20d00m
242*	05h20m,	+10d00m	282*	08h24m,	+20d00m
243*	06h00m,	+10d00m	283*	09h06m,	+20d00m
244*	06h40m,	+10d00m	284*	09h48m,	+20d00m
245*	07h20m,	+10d00m	285*	10h30m,	+20d00m
246*	08h00m,	+10d00m	286*	11h12m,	+20d00m
247*	08h40m,	+10d00m	287*	11h54m,	+20d00m
248*	09h20m,	+10d00m	288*	12h36m,	+20d00m
249*	10h00m,	+10d00m	289	13h18m,	+20d00m
250*	10h40m,	+10d00m	290	14h00m,	+20d00m
251*	11h20m,	+10d00m	291	14h42m,	+20d00m
252*	12h00m,	+10d00m	292	15h24m,	+20d00m
253*	12h40m,	+10d00m	293	16h06m,	+20d00m
254*	13h20m,	+10d00m	294	16h48m,	+20d00m
255*	14h00m,	+10d00m	295	17h30m,	+20d00m
256	14h40m,	+10d00m	296	18h12m,	+20d00m
257	15h20m,	+10d00m	297	18h54m,	+20d00m
258	16h00m,	+10d00m	298	19h36m,	+20d00m
259	16h40m,	+10d00m	299	20h18m,	+20d00m
260	17h20m,	+10d00m	300	21h00m,	+20d00m
261	18h00m,	+10d00m	301	21h42m,	+20d00m
262	18h40m,	+10d00m	302	22h24m,	+20d00m
263	19h20m,	+10d00m	303	23h06m,	+20d00m
264	20h00m,	+10d00m	304*	23h48m,	+20d00m
265	20h40m,	+10d00m	305	00h00m,	+30d00m
266	21h20m,	+10d00m	306	00h46m,	+30d00m
267	22h00m,	+10d00m	307*	01h32m,	+30d00m
268*	22h40m,	+10d00m	308*	02h18m,	+30d00m
269*	23h20m,	+10d00m	309*	03h04m,	+30d00m
270*	00h00m,	+20d00m	310*	03h50m,	+30d00m
271*	00h42m,	+20d00m	311*	04h36m,	+30d00m
272*	01h24m,	+20d00m	312*	05h22m,	+30d00m
273*	02h06m,	+20d00m	313*	06h08m,	+30d00m
274*	02h48m,	+20d00m	314*	06h54m,	+30d00m
275*	03h30m,	+20d00m	315*	07h40m,	+30d00m
276*	04h12m,	+20d00m	316*	08h26m,	+30d00m
277*	04h54m,	+20d00m	317*	09h12m,	+30d00m
278*	05h36m,	+20d00m	318*	09h58m,	+30d00m
279*	06h18m,	+20d00m	319*	10h44m,	+30d00m
280*	07h00m,	+20d00m	320	11h30m,	+30d00m

* ISSA Reject fields.

Field#	RA DEC	Field #	RA DEC
321	12h16m,+30d00m	361	20h48m,+40d00m
322	13h02m,+30d00m	362	21h40m,+40d00m
323	13h48m,+30d00m	363	22h32m,+40d00m
324	14h34m,+30d00m	364	23h24m,+40d00m
325	15h20m,+30d00m	365	00h00m,+50d00m
326	16h06m,+30d00m	366	01h00m,+50d00m
327	16h52m,+30d00m	367	02h00m,+50d00m
328	17h38m,+30d00m	368	03h00m,+50d00m
329	18h24m,+30d00m	369	04h00m,+50d00m
330	19h10m,+30d00m	370	05h00m,+50d00m
331	19h56m,+30d00m	371	06h00m,+50d00m
332	20h42m,+30d00m	372	07h00m,+50d00m
333	21h28m,+30d00m	373	08h00m,+50d00m
334	22h14m,+30d00m	374	09h00m,+50d00m
335	23h00m,+30d00m	375	10h00m,+50d00m
336	23h46m,+30d00m	376	11h00m,+50d00m
337	00h00m,+40d00m	377	12h00m,+50d00m
338	00h52m,+40d00m	378	13h00m,+50d00m
339	01h44m,+40d00m	379	14h00m,+50d00m
340	02h36m,+40d00m	380	15h00m,+50d00m
341	03h28m,+40d00m	381	16h00m,+50d00m
342*	04h20m,+40d00m	382	17h00m,+50d00m
343*	05h12m,+40d00m	383	18h00m,+50d00m
344*	06h04m,+40d00m	384	19h00m,+50d00m
345*	06h56m,+40d00m	385	20h00m,+50d00m
346*	07h48m,+40d00m	386	21h00m,+50d00m
347	08h40m,+40d00m	387	22h00m,+50d00m
348	09h32m,+40d00m	388	23h00m,+50d00m
349	10h24m,+40d00m	389	00h00m,+60d00m
350	11h16m,+40d00m	390	01h16m,+60d00m
351	12h08m,+40d00m	391	02h32m,+60d00m
352	13h00m,+40d00m	392	03h48m,+60d00m
353	13h52m,+40d00m	393	05h04m,+60d00m
354	14h44m,+40d00m	394	06h20m,+60d00m
355	15h36m,+40d00m	395	07h36m,+60d00m
356	16h28m,+40d00m	396	08h52m,+60d00m
357	17h20m,+40d00m	397	10h08m,+60d00m
358	18h12m,+40d00m	398	11h24m,+60d00m
359	19h04m,+40d00m	399	12h40m,+60d00m
360	19h56m,+40d00m	400	13h56m,+60d00m

* ISSA Reject fields.

Field#	RA	DEC
401	15h12m,	+60d00m
402	16h28m,	+60d00m
403	17h44m,	+60d00m
404	19h00m,	+60d00m
405	20h16m,	+60d00m
406	21h32m,	+60d00m
407	22h48m,	+60d00m
408	00h00m,	+70d00m
409	01h44m,	+70d00m
410	03h28m,	+70d00m
411	05h12m,	+70d00m
412	06h56m,	+70d00m
413	08h40m,	+70d00m
414	10h24m,	+70d00m
415	12h08m,	+70d00m
416	13h52m,	+70d00m
417	15h36m,	+70d00m
418	17h20m,	+70d00m
419	19h04m,	+70d00m
420	20h48m,	+70d00m
421	22h32m,	+70d00m
422	00h00m,	+80d00m
423	03h00m,	+80d00m
424	06h00m,	+80d00m
425	09h00m,	+80d00m
426	12h00m,	+80d00m
427	15h00m,	+80d00m
428	18h00m,	+80d00m
429	21h00m,	+80d00m
430	00h00m,	+90d00m

APPENDIX B

Compression Algorithm

The first step in processing the IRAS time-ordered scan data into the ISSA images was to smooth and resample the time-ordered detector data such that all detectors were sampled with a 0.5-second period. This resulted in a spatial sampling period of 1.93′ at the IRAS scan rate of $3.85'\mathrm{s}^{-1}$. A symmetrical Lanczos (1) single smoothed filter kernel was convolved with the full resolution detector streams to produce the smoothed output data.

$$K(\tau)\begin{cases}\left(\dfrac{\sin(\pi\tau)}{\pi\tau}\right)^2, & \text{for } -\frac{1}{2} < \tau < \frac{1}{2} \\ 0\,, & \text{otherwise.}\end{cases} \tag{1}$$

where τ is time in seconds.

The numerical values of the normalized filter kernels are shown in Table B.1. Convolution of these kernels with the 16, 16, 8 and 4 samples per second data from the 12, 25, 60 and 100 μm detectors, respectively, smoothed the data so that every eighth, fourth, or second sample were retained, producing the desired two samples per second output sets at each wavelength.

These compressed detector data were also used to create the *IRAS Zodiacal History File* (ZOHF).

Table B.1
Filter Kernels

τ (sec)	12 μm	25 μm	60 μm	100 μm
$-\frac{7}{16}$	0.00268	0.00268		
$-\frac{3}{8}$	0.01247	0.01247	0.02454	
$-\frac{5}{16}$	0.03065	0.03065		
$-\frac{1}{4}$	0.05611	0.05611	0.11221	0.22384
$-\frac{3}{16}$	0.08515	0.08515		
$-\frac{1}{8}$	0.11223	0.11223	0.22442	
$-\frac{1}{16}$	0.13148	0.13148		
0	0.13845	0.13845	0.27687	0.55231
$\frac{1}{16}$	0.13148	0.13148		
$\frac{1}{8}$	0.11223	0.11223	0.22442	
$\frac{3}{16}$	0.08515	0.08515		
$\frac{1}{4}$	0.05611	0.05611	0.11221	0.22384
$\frac{5}{16}$	0.03065	0.03065		
$\frac{3}{8}$	0.01247	0.01247	0.02454	
$\frac{7}{16}$	0.00268	0.00268		

References

Hamming, R.W. 1977, Digital Filters, Prentice-Hall, Inc., Englewood Cliffs, NJ.

APPENDIX C

Pre-Production Anomalies

Prior to production, a list of anomalies to be removed from the ISSA was assembled from three sources. The list was a composite of the anomalies found in calibration and pointing reconstruction, in the *SkyFlux* image product, and in the *IRAS Faint Source Survey*.

Not all anomalies in the *SkyFlux* images were placed on the list. Only particle hits (p) and radiation hits (r) were removed. Other anomaly types from the *SkyFlux* image product were thought to be salvageable using the calibration and destriping techniques employed in making the *IRAS Sky Survey Atlas*.

The following table summarizes the composite list of anomalies. The anomaly type is given along with the number of seconds removed or number of complete scans removed. An explanation of the anomaly type code is also included. A total of 42 or 0.7% of total number of scans were removed due to calibration problems along with 32,288 seconds or approximately 0.3% of the entire mission due to other problems.

TABLE C.1

Summary of Pre-Production Anomalies Removed from the IRAS Sky Survey Atlas Images

Source of Anomaly Identification	Type	# scans removed	# seconds removed
Calibration and Pointing Reconstruction	lg	25	
	t	7	
	bb	10	
	xs		123
	re		52
Original Image Anomalous Scans	p		13,735
	r		3,170
Faint Source Survey			15,208
SUBTOTAL		42 ≈ 0.7%	32,288 ≈ 0.3%
TOTAL		≈ 1%	

lg = low-gain ao/survey
t = survey following TFCAL (see §III.A.2.b) (not recommended due to bias boost)
bb = bias boost problem
xs = cross-scan excursions (pointing)
re = roll excursions (pointing)
p = particle hits
r = radiation hits

APPENDIX D

Global Destriping

D.1 Introduction

Global destriping for ISSA was accomplished using a BasketWeave DeStriping (BWDS) algorithm (Emerson and Gräve 1988). This algorithm assumes that each detector of the same band sees the same intensity, after removal of the zodiacal emission, when pointed to the same location on the sky at any time during the IRAS mission. Due to the redundancy in the sky coverage, a typical detector scan path crossed hundreds of other detector scan paths occurring at different times. An intensity difference history for each detector scan was generated and fitted with an n^{th} order polynomial. Each scan was adjusted by a portion of the difference between the original scan and the fit. This process was repeated until differences were minimized.

There were a number of difficulties involved in implementing this approach. The contribution of the zodiacal emission to the total intensity at any location on the sky varied throughout the mission. Imperfections in the removal of the zodiacal emission by use of a physical model developed by J. Good at IPAC left residual zodiacal emission, particularly near the ecliptic plane. This effect was most troublesome at 12 and 25 μm. Residual hysteresis remained after the hysteresis removal effort (see §III.A.2). The remaining hysteresis resulted in intensity discrepancies near the Galactic plane, noticeable at 60 and 100 μm. Finally, the detector-to-detector gain discrepancy attributable to uncertainties in individual detector AC-to-DC responsivity scale factors was also noticeable at 60 and 100 μm in the Galactic plane.

D.2 Database Generation

One major consideration was the enormous size of the database required to support a global destriper. There were 1.2 million focal plane crossings in survey observations during the mission. See §II.C.4 of the *IRAS Explanatory Supplement 1988*, hereafter referred to as the *Main Supplement*, for description of the IRAS focal plane. A focal plane crossing occurred when an IRAS scan path crossed the path of another IRAS scan taken at a different time in the mission. Unfortunately these crossings were not evenly distributed. As illustrated in Figure D.1, the focal plane crossings were more numerous near the ecliptic poles. This was due to the scan geometry where each scan maintained a constant cone angle around the sunline. Since the sunline stays in the ecliptic plane, all scans were parallel at the ecliptic plane and no scan crossings occurred. If all the scans had a cone angle of 90°, the only focal plane crossings would have occurred at the ecliptic poles. Fortunately for the global destriper, cone angles varied from 60° to 120°. The more extreme cone angles were used less frequently, with the most extreme angles confined to HCON-3. Non-latitude-dependent density changes in Figure D.1 reflect changes in the cone angles (HCON-3) or changes in coverage density (*Main Supplement* §III.C).

One can determine how the crossing frequency varied through a typical observation by combining the focal plane crossing data from Figure D.1 with information about the

way the survey scans covered the sky. This information is presented in the form of a histogram in Figure D.2. Each scan length was normalized to 1.0 and then divided into an equal number of fractional segments. A bin represents the cumulative number of crossings within that fractional segment for all scans. As expected, there are many more crossings near the end points of the observation (typically near one of the ecliptic poles) than the middle (typically near the ecliptic plane). An even distribution of points would be easier for fitting. Nothing could be done to increase crossings near the ecliptic plane, but a thinning of crossings near the poles was possible. To avoid aliasing, the selection process had to be random. However, no reduction in the crossing density near the ecliptic plane was allowed. To accomplish these two objectives, each scan was divided into 30-second time intervals and as many as four separate focal plane crossings were randomly selected from each of the time intervals.

All detector crossings within the same band were considered separately. This had a major impact on the database size. Only operative detectors 3/4 size or larger (*Main Supplement*, §II.C.4) were used by the global algorithm. The detectors listed in Table D.1 below show that the number used varied with wavelength over a range from 11 to 14.

Table D.1

Detectors for which Global Destripe Parameters were Derived

Wavelength (μm)	Detectors	Total
12	23 24 25 <u>27</u> 28 29 30 48 49 50 51 52 53 <u>54</u>	14
25	16 18 19 21 22 40 41 42 43 44 45	11
60	08 09 10 <u>12</u> 13 14 15 32 33 34 35 37 <u>38</u>	13
100	01 02 03 04 05 06 07 56 57 58 59 60 61	13

Note: Underlined detectors are 3/4 size.

The proliferation of detector crossings is illustrated in Figure D.3. Geometry of a sample 100 μm focal plane crossing is shown. Let "A" refer to the earlier crossing and "B" refer to the later. The point where the middle of the swath laid down by detector 5, scan A crosses the middle of the swath laid down by detector 61 sometime later during scan B is circled as a sample detector crossing point. The 13 detectors used at 100 μm result in 169 detector crossing pairs. The proliferation factor varies with the square of the number of detectors used per band; 196, 121, 169 and 169 at 12, 25, 60 and 100 μm, respectively. Note that as the angle between scans A and B decreases, the detector crossing grid becomes more elongated and detectors on opposite sides of the focal plane cross further from the central point.

The database for each band had one record per node (boresight crossing point). Each record included an n $\times$ n matrix of intensities, where n equals the number of detectors used for that band. In order to minimize the file size, each detector intensity was encoded into a

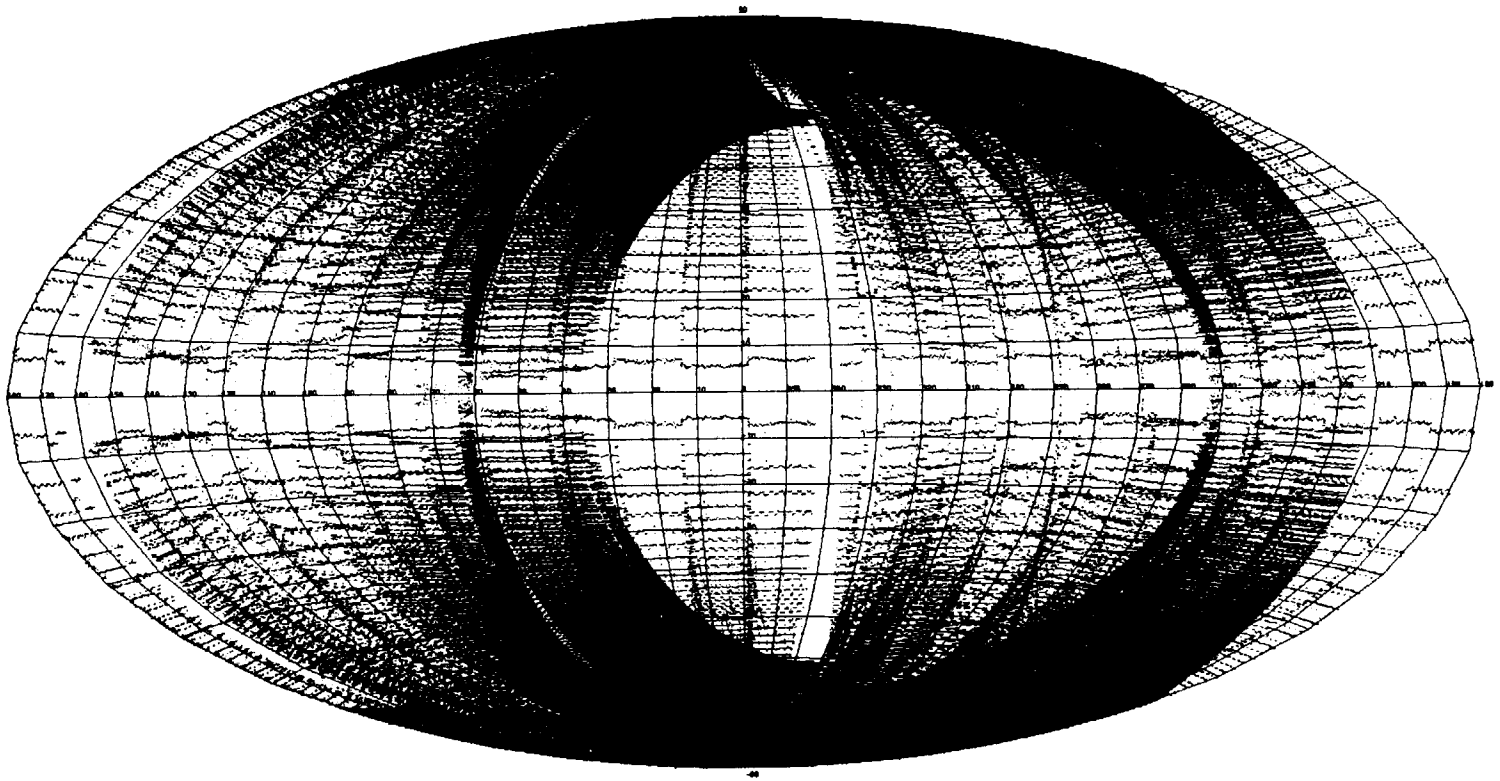

Figure D.1 Distribution of boresight intercepts for the 1.2 million focal plane crossings in the IRAS mission, plotted in ecliptic coordinates.

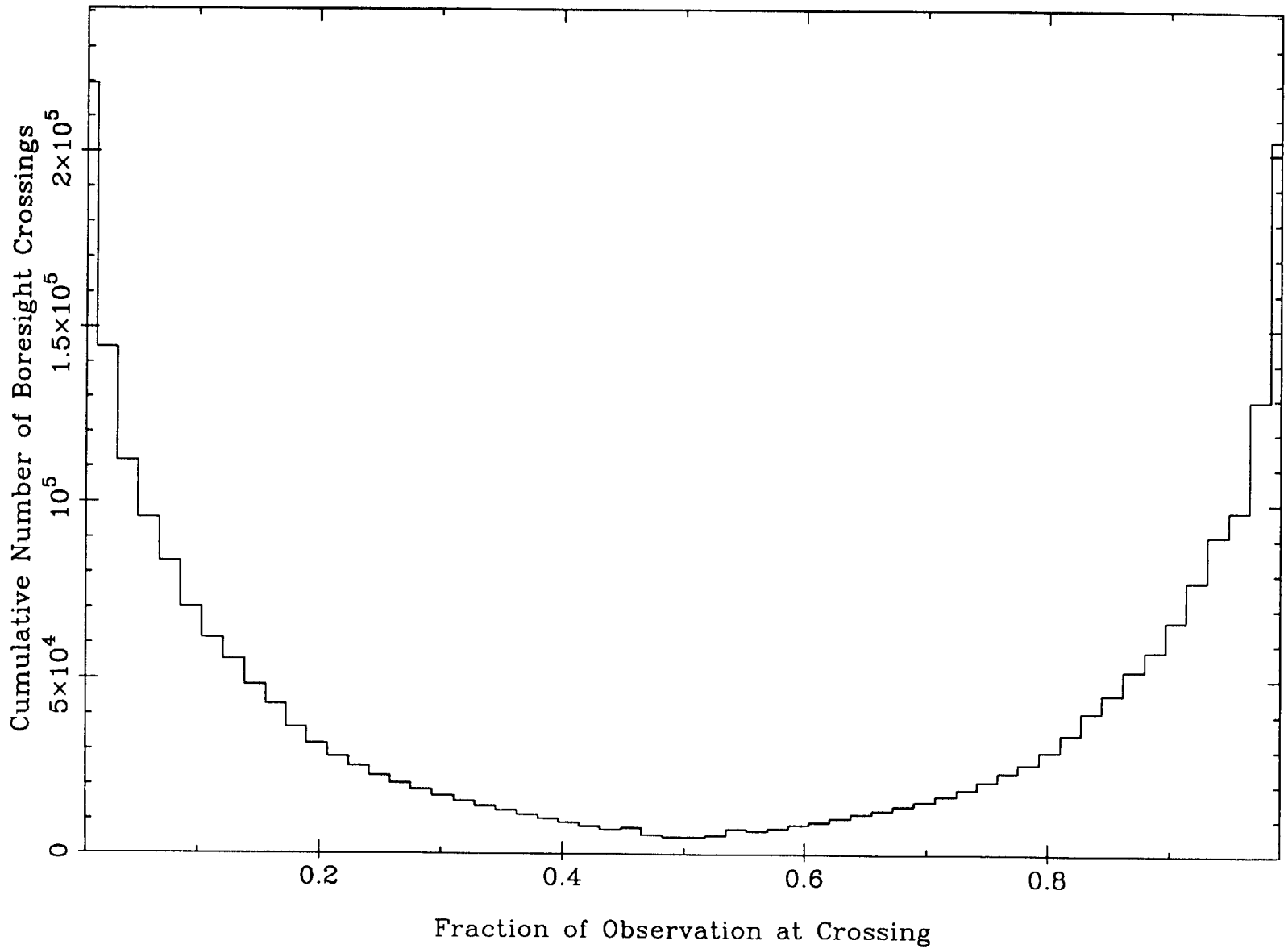

Figure D.2 Histogram of boresight crossing counts per fractional scan segment.

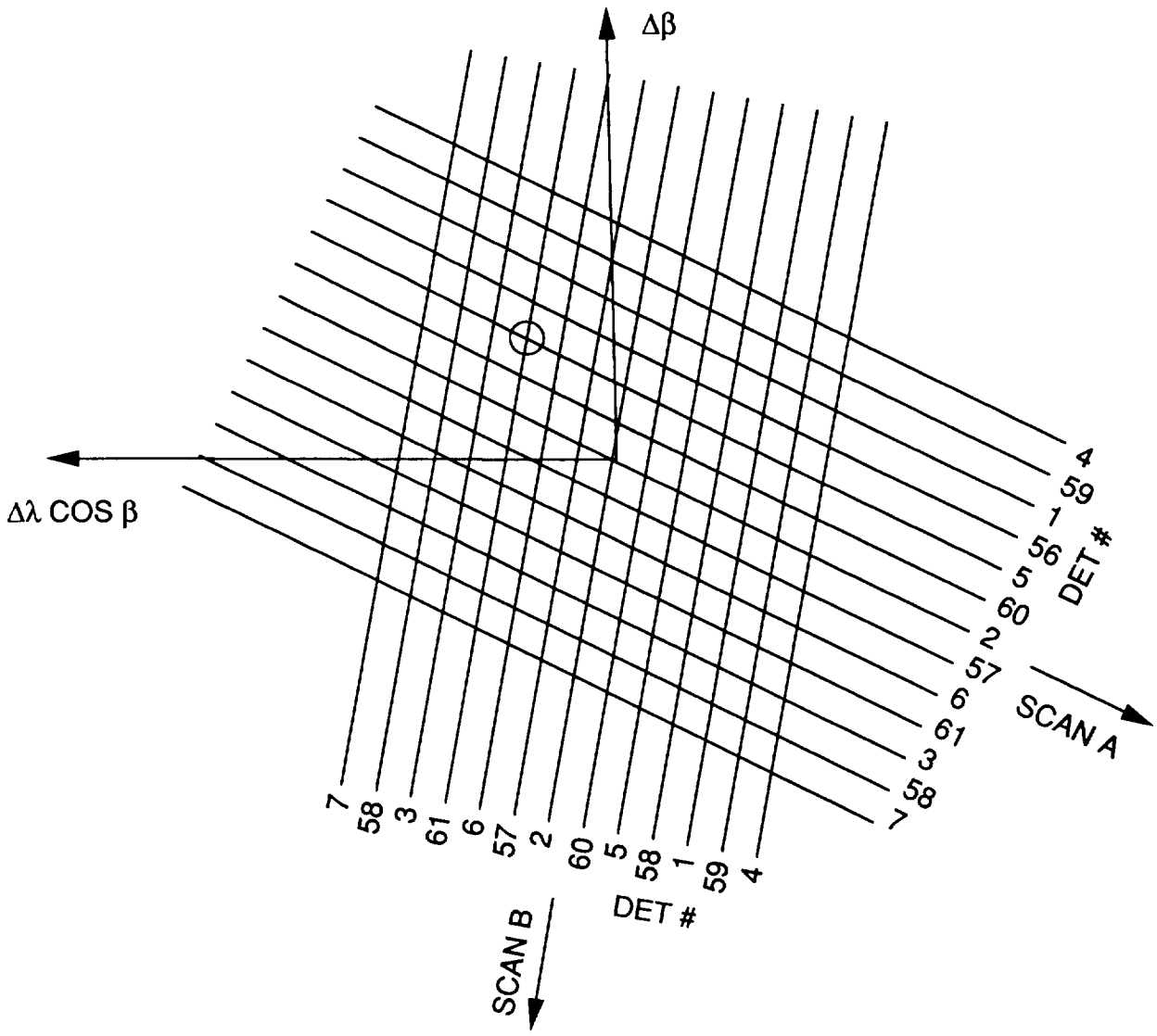

Figure D.3 Proliferation of detector intercepts — 100 μm. This figure illustrates the geometry of a focal plane crossing for 100 μm detectors. A and B represent crossing scan tracks. The point where the path laid down by detector 5, scan A crosses the path laid down by detector 61, scan B is circled as a sample detector crossing point. For the 13 detectors used at 100 μm there are 169 detector crossing pairs. The proliferation factor varies with the square of the number of detectors used per band: 196, 121, 169 and 169 at 12, 25, 60 and 100 μm, respectively.

two-byte integer. The encoding scheme determined a unique scale factor and bias for each of the two focal plane scans crossing through the node. These were chosen to preserve as much intensity information as possible. Only those nodes selected as above made it into the database. For each selected node all detector information, boresight crossing times, scan angles and position data were included. Everything needed to reconstruct the position, time and intensities at each detector crossing was saved.

In order to compute the intensities at a node, the crossing geometry of two scans was used to compute the differences from the boresight crossing times for every pair of crossing detectors. These times were used to interpolate intensities out of the time-ordered detector data. Detector data are phased to adjust for the nominal time differences between when various rows of detectors cross the same spatial point. The phasing had to be removed before the interpolation could be performed. The intensity at the required time was linearly interpolated from the detector data, provided that the quality flags on both sides of the required time indicated good values.

To minimize database size, all necessary information was recorded once per node along with a pointer to the location of the next node. Since node selections were performed independently on each scan, some nodes were used only once. This file structure proved economical but too slow in accessing nodes that were nonsequential. To improve performance, a separate record was entered for each pass through the selected node. If a node was selected on both focal plane scan A and scan B, the node data would be recorded twice. This allowed the file to be sorted so that access was sequential. Since some nodes were selected only once, the disk requirements did not quite double.

As mentioned earlier, the BWDS database contained detector data that had the zodiacal emission removed using a physical model derived at IPAC by J. Good (§III.C.2 and Appendix G). Figure D.4(a) shows a low-resolution intensity map of the entire HCON-1 and HCON-2 sky at 12 μm after removal of the zodiacal dust using the J. Good model. Note the sharp change in overall intensity near ecliptic longitude of 60° and a less pronounced change near 240°. The intensity difference across the discontinuity has a maximum value of about 2.0 MJy sr^{-1}, roughly 7% of the local intensity before removal of the zodiacal component. Similar percentage errors are found at 25 μm. The beginning of the descending leg occurs at 60°, the ascending leg of the HCON-1 and HCON-2 survey occurs at 240°. Six months later the descending leg had progressed to 240° and the ascending leg to 60° point. Thus the data on the right side of each discontinuity were taken six months later than that on the left.

Although these discontinuities reflect imperfect modeling of the zodiacal dust cloud, the residual errors are a small percentage of the total zodiacal emission. Similar discontinuities are not seen in the HCON-3 sky (Figure D.4(b)) because the telescope ran out of liquid helium before the sky coverage came back to the starting point.

D.3 Database Clean-Up

As originally set up, the BWDS database contained a small fraction of anomalous data that could cause problems in downstream processing. These anomalies arise from a

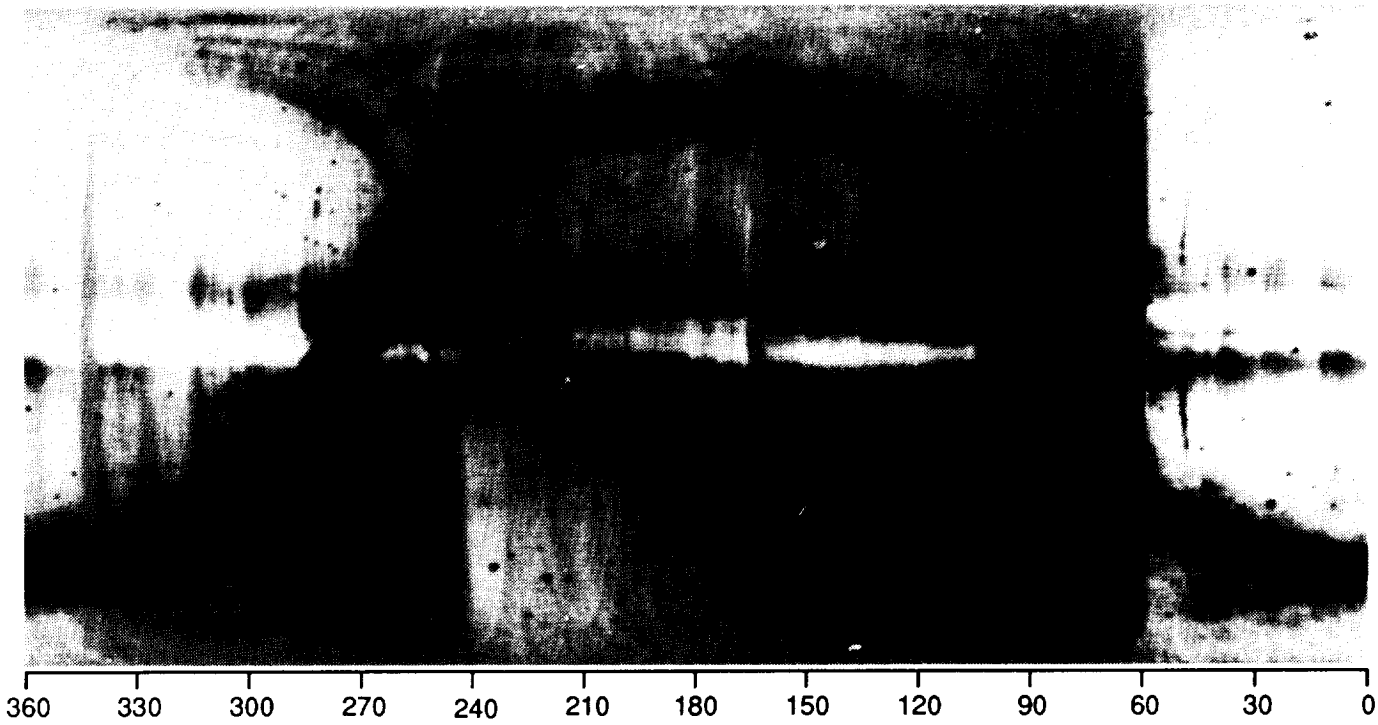

Figure D.4(a) Intensity residuals (HCON-1 and HCON-2) at 12 μm in ecliptic cylindrical coordinates.

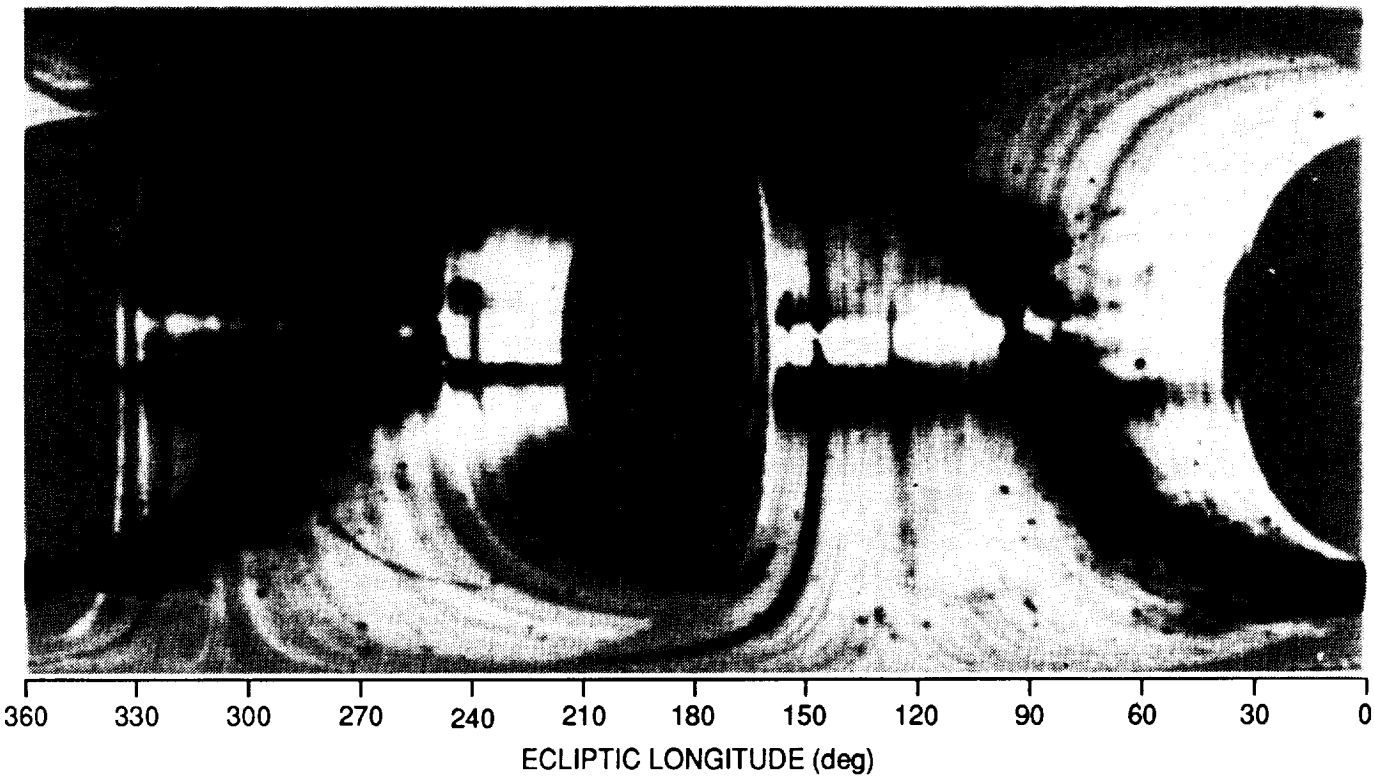

Figure D.4(b) Intensity residuals (HCON-3) at 12 μm in ecliptic cylindrical coordinates. These residual intensity images were made from the *IRAS Zodiacal History File* (ZOHF) Version 3.1 after removing emission due to the zodiacal dust cloud. A zodiacal dust cloud model developed at IPAC by J. Good was used to derive the offset.

myriad of sources, but they can be characterized into three classes. Class I consists of those anomalies introduced into the datastream prior to generation of the BWDS database. This is the largest class of anomalies. Class II is composed of those anomalies introduced during generation of the BWDS database. Finally, Class III consists of those time periods when the global fits are unsatisfactory. Once identified, anomalies of Class I and Class III were included in the Problem Scan Summary File (PSSF). This file was then used to set use flags in the BWDS database prior to the difference fits. It was also used by downstream processors. Class I anomalies are discussed in further detail in Appendix C and Class III anomalies in §D.5.

The one error type known to belong to Class II was inadvertently introduced while encoding detector intensities for inclusion in the BWDS database. For a given band, the range from the lowest to the highest intensity recorded on the detectors of the first scan (Scan A) while passing through a given node (node n) was divided into 65,535 parts. Each intensity was assigned a two-byte integer between -32767 and $+32767$, with -32768 reserved to indicate unreliable data. An appropriate scale factor and bias were determined to allow later decoding. Another scale/bias set was determined in the same manner for the second scan (Scan B) passing through node n, and the intensities were encoded as before. This process was repeated for each node. The problem arose when the difference between the lowest and highest intensities became excessively large, driving down the resolution with which all the intensities could be stored. One extremely bright point in a node would degrade the resolution of all the other intensities from that scan/node.

Since intensity differences large enough to cause obvious difficulties were rare, this problem escaped notice during testing of the database generation software. Once the problem was understood, it became apparent that the nodes with degraded resolution could be quickly identified by their excessively large values of scale factor and bias. Given that the affected nodes were rare, easily identified and would be rather difficult to regenerate, it was decided to drop them from the database. In order not to disturb the existing database indexing, this was accomplished by resetting use flags rather than actually removing the records.

D.4 Intensity Difference Fits

Given the size of the BWDS database, there was only enough disk space to hold one of the four wavelength bands at a time. The intensity difference fits were performed starting with 12 μm and proceeding through 25, 60 and 100 μm. All four bands were fitted using n^{th} order orthogonal polynomials, but the fit technique varied to some extent with band for two reasons. First, each wavelength band is unique and required some tailoring of the approach to achieve the best results. Second, the various bands were done in sequence and more experience could be brought to bear as time went on. The whole process was very time consuming; it was not feasible to reprocess earlier wavelengths.

Before discussing the approach used to fit each band, assumptions and approximations are discussed. As mentioned earlier, the BWDS algorithm is based on the premise that any detector from the same band sees the same intensity when pointed to the same spot

in the sky at any time during the mission after removal of the zodiacal emission. Ideally, each detector should:

1) be centered on the same spot
2) be oriented the same way
3) have the same size and shape
4) have the same responsivity as a function of position
5) see the sky unchanged between observations.

The requirement that two detectors share a common center point at the time of differencing can be met. Pointing reconstruction uncertainties are quite small relative to the size of the detectors. Given accurately known time histories of boresight direction and rotation angle, along with knowledge of the relative focal plane position of each detector, it is possible to precisely determine the time and sky position of each detector crossing. The requirement that they be oriented the same way can only be met near the ecliptic plane and grows increasingly worse moving toward the poles. The size and shape match can usually be met except when a 3/4 size detector crosses a full size. The matched responsivity requirement will never be exactly met except when the same detector crosses itself at a later time.

Due to the large number of intensity differences involved in a typical fit, along with the randomness of detector mix and orientations, the first four requirements are not critical. For any given difference point, errors resulting from the above problems are as likely to be positive as negative. The order of the fit is low compared to the number of differences, resulting in an increase in the dispersion rather than a shift in the mean. For the same reason, point sources do not have to be removed. If a point source is observed by one detector and not the other it will indeed throw off that difference, but the next point source is just as likely to throw it off in the opposite direction. The net effect on the mean, given a large number of differences, is thus negligible.

The requirement that the sky remain unchanged between observations cannot be met so easily. The effects of asteroids and variable stars can be discounted using the arguments outlined in the previous paragraph. Time variations in the residual zodiacal foreground, however, affect extended areas of the sky in a systematic, slowly changing way. If the zodiacal emission is not completely removed prior to fitting, resulting intensities will be affected by the residual emission. Therefore, coverages of the same area made at widely separated times will have different average intensities. The BWDS algorithm performs several iterations converging to a solution that forces all coverages to their mean background. An area covered at three widely separated times will therefore have a different background intensity than an adjacent area covered only twice.

D.4.a *Fits at 12 μm*

The order of the orthogonal polynomial fit for each detector-scan was based on the number of intensity difference points available after questionable points had been removed. The order selected would follow low-frequency detector errors while not introducing or removing sub-field ($< 12.5°$)-sized structure. The relationship between the number of difference points available (N) and the order of fit (O) for 12 μm is given in Table D.2.

Table D.2
Relationship between Number of Difference Points and Order of Fit for 12 μm

Difference Points	Order of Fit
0 – 4	No fit
5 – 50	0
51 – 150	1
151 – 350	2
351 – 750	3
751 – 1500	4
1501 – 2250	5
2251 – 3000	6
$\geq$ 3001	7

Any scans where N was less than five were not fit by this algorithm but were fit by the local destriper (§III.C.3.b).

Fitting the intensity difference history assumes that the detector errors are time-varying bias errors. However, a certain amount of gain error can be removed as well. As the fraction of the intensity difference attributable to gain error increases, it becomes more difficult to derive a fit (of a given order) that works for both the high- and low-intensity regions of the scan.

Differences due to gain errors will naturally be greater in high intensity regions. If every point is weighted equally, these regions will dominate the fit. To compensate for this effect at 12 μm, each difference point was inverse-intensity weighted. The weighting intensity was the larger of the two intensities being differenced. Weights were not allowed to exceed 25 times the average.

As each intensity difference was computed, the best estimate of the truth was taken to be halfway between the two. It was actually the difference between the intensity readout from the current scan and the best estimate of the truth that was loaded into the difference history to be fitted. The algorithm corrected the intensities after all the scans had been fitted. This was a better approach than trying to make corrections to crossing scans as they became available. The latter course would make the results dependent on the order of processing and would make restarting in midstream difficult.

Observations beginning or ending near the ecliptic plane were difficult to fit due to the paucity of detector crossings near the plane. A large percentage of these scans were actually continued on the other side of the ecliptic plane under a different observation number. These observations were broken near the ecliptic plane due to avoidance maneuvers. These included avoidance of Jupiter, the Moon and the South Atlantic Anomaly (SAA). The broken scans were knit together for purposes of the BWDS fit. Because of time lost during the avoidance maneuver, time adjustments had to be made. When a fit on part A of a

broken scan was desired, the part B times were adjusted and vice versa. The additional difference points that were not part of the scan were referred to as "ghost" points.

The 12 μm fits were done a total of four times, with all updates being made after each iteration. In order to prevent spurious differences from unduly affecting the fit, differences with magnitudes greater than an input threshold value were not used.

The threshold used for the first iteration was 0.5×10^{-6} $Wm^{-2}sr^{-1}$. For subsequent iterations the threshold was tightened to 0.33×10^{-6} $Wm^{-2}sr^{-1}$. The number and distribution of rejects were carefully monitored. Difference histories for scans with excessive rejects were plotted and manually inspected (§D.5).

D.4.b *Fits at 25 μm*

The 25 μm BWDS fit started with the same procedure outlined for 12 μm. The first four iterations used the 12 μm criteria to select the order of fit and to determine the best estimate from which to compute the intensity difference.

Inverse intensity weighting was also used. Rejection thresholds were raised to 0.75×10^{-6} $Wm^{-2}sr^{-1}$ for the first iteration and 0.5×10^{-6} $Wm^{-2}sr^{-1}$ for subsequent iterations.

The 25 μm data differed from 12 μm in one significant way. The magnitudes of the intensity differences near the ecliptic plane were much more pronounced at 25 μm. This was probably due to gain errors being driven by the higher zodiacal foreground intensity at 25 μm. The steep rise near the ecliptic was difficult to fit, which threw off the fit in the low-intensity regions near the poles. The problem is illustrated in Figure D.5(a), which shows the intensity difference history for a detector in one scan with a sixth-order fit superimposed. Intensity differences were computed by differencing the intensities along the desired detector-scan path with the intensities of crossing detectors. To improve the fit, the algorithm was modified to allow fits as high as 12^{th} order. This improved the fit but was not totally satisfactory.

Finally, the northern and southern ecliptic hemispheres were fitted separately and then knitted together. To facilitate the knitting, an overlap region at the ecliptic plane 20° wide was considered to be part of both hemispheres. Fits were limited to 10^{th} order, with the relationship between the number of difference points available (N) and the order of fit (O) established, shown in Table D.3.

The northern solution was used in the north and the southern solution in the south. Near the ecliptic plane the northern and southern components of each scan were knitted together by linearly changing the weighting used to combine the two solutions over the effective overlap interval. Thus on an ascending scan the southern solution would be weighted 1.0 and the northern weighted 0.0 at the beginning of the overlap interval, 0.5 and 0.5 at the midpoint and 0.0 and 1.0 at the end, respectively.

The overlap interval for a given scan is defined to extend from the earliest to the latest detector crossing contained within the 20° overlap region. It should be noted that for any given scan the effective overlap could be less than 20° if there was a sparsity of crossing

Table D.3
Relationship between Number of Difference Points and Order of Fit for 25 μm

Difference Points	Order of Fit
0 – 4	No fit
5 – 50	0
51 – 150	1
151 – 350	2
351 – 600	3
601 – 850	4
851 – 1100	5
1101 – 1350	6
1351 – 1600	7
1601 – 1850	8
1851 – 2100	9
$\geq$ 2101	10

points. Fits were never extrapolated before the first or after the last detector crossing. The dual-hemispheres-with-overlap approach was used in the fifth iteration of the 25 μm parameters and proved to work well, as seen in Figure D.5(b). Because this approach fit the high- and low-intensity regions equally well, equal weighting was used.

The difference histories for the fifth iteration were computed assuming the best estimate of truth to be the crossing scan intensity. Thus a full step rather than a half step was taken, allowing the final iteration to be more effective. This effectiveness was particularly important since the fifth iteration also had to remove fitting errors caused by anomalous "ghost" points inadvertently introduced in iterations one through four. The use of "ghost" points was dropped from the fifth iteration at 25 μm as well as for all iterations at 60 and 100 μm.

A number of factors were monitored as indicators of scans for which the dual-hemisphere approach might be inappropriate. If any one of these indicators exceeded a given threshold, a full-scan fit was used for that scan. Full-scan fits used the same crossing count vs. fit order detailed in Table D.3. Any one of the following conditions would trigger a full-scan fit for the affected detector-scan.

1) Insufficient points for southern hemisphere fit
2) Insufficient points for northern hemisphere fit
3) All southern hemisphere points contained in overlap
4) All northern hemisphere points contained in overlap
5) Effective overlap less than 100 seconds of time
6) Difference between north and south solutions greater than 0.125×10^{-6} $Wm^{-2}sr^{-1}$ at midpoint or 0.25×10^{-6} $Wm^{-2}sr^{-1}$ at either end of effective overlap
7) Ratio of north/south intensity difference over effective overlap time greater than 0.5×10^{-9} $Wm^{-2}sr^{-1}s^{-1}$ at midpoint or 1.0×10^{-9} $Wm^{-2}sr^{-1}s^{-1}$ at either end.

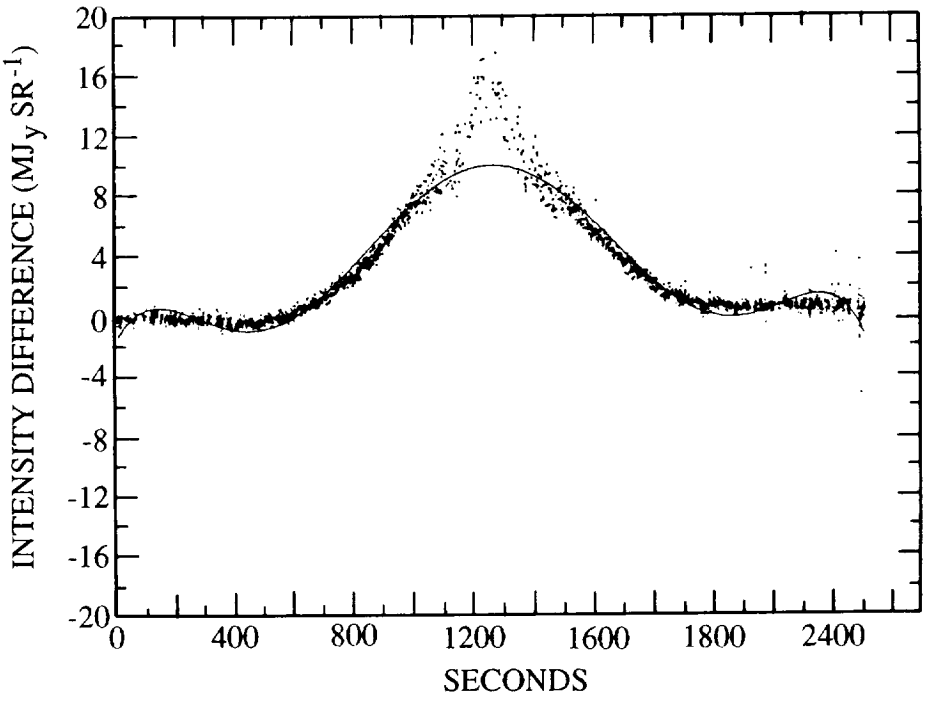

Figure D.5(a) Intensity differences along a single detector-scan track with a sixth order fit.

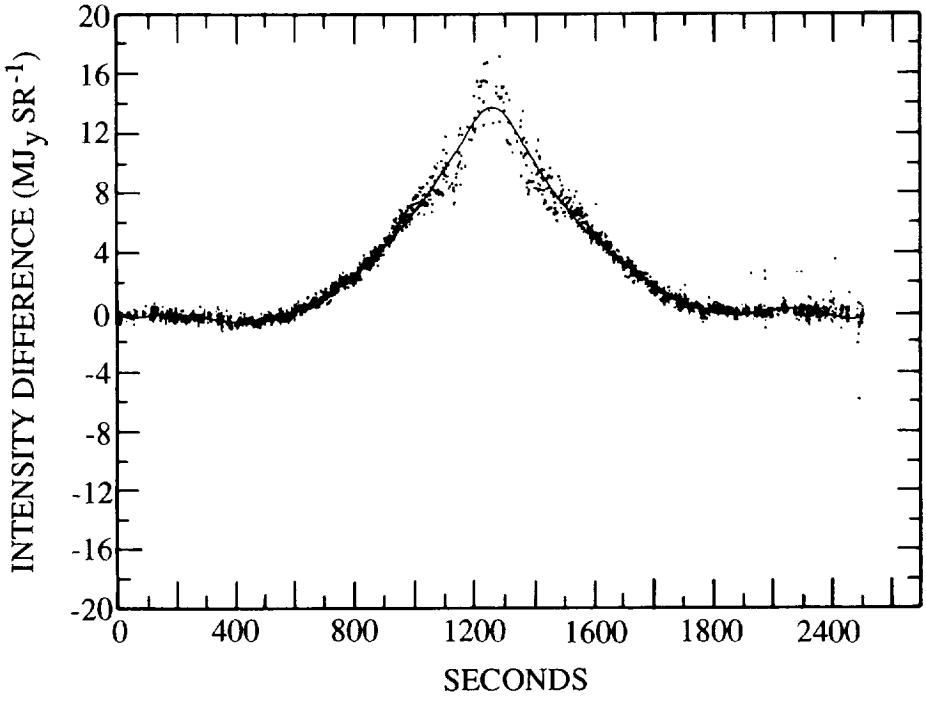

Figure D.5(b) Intensity differences along a single detector-scan track with a fit derived with the dual-hemisphere-with-overlap algorithm.

As at 12 μm, the 25 μm fits were carefully monitored (§D.5). All 25 μm scans for which "ghosts" points were used prior to iteration five were manually checked with intensity difference plots. This verified that iteration five had successfully removed the adverse effects resulting from the anomalous "ghost" points.

D.4.c *Fits at 60 μm*

The 60 μm fits used the same order-of-fit scheme outlined for iteration five at 25 μm (Table D.3). The fraction of the difference, α, between the path intensity and the crossing intensity taken to be the best estimate of the truth varied with iteration. Increasing α with each iteration provided a more rapid convergence. Only three iterations were needed for 60 μm; α was set at 0.5, 0.75, and 1.0. Reject thresholds were set at 0.75×10^{-6}, 0.5×10^{-6} and 0.5×10^{-6} $\mathrm{Wm^{-2}sr^{-1}}$.

Intensity difference increases near the ecliptic plane were not significant for the 60 μm fits. However, the problem was significant near the Galactic plane. The cause was gain error, driven by the higher Galactic plane intensity at 60 μm. A modified version of the dual- hemisphere approach using Galactic hemispheres was considered and rejected.

The intensity difference increases at the Galactic plane could only be handled by fitting the gain errors directly. This option was investigated (see Appendix E) but, since applying a gain correction would compromise the point source calibration, it was not used. The gain fitting investigation showed that the increased intensity differences near the Galactic plane are due to two effects: an error in the DC response of each detector and residual hysteresis. Both gain errors would have to be addressed to get good fits near the Galactic plane. No attempt was made to fit this region accurately at 60 μm. The inverse intensity weighting coupled with the higher order polynomials allowed for good fits everywhere except for within 1° to 2° of the Galactic plane.

D.4.d *Fits at 100 μm*

The 100 μm fit procedure was similar to the 60 μm procedure with the exception that the magnitudes of the intensity differences near the Galactic plane at 100 μm were much greater. They were so large that even fits up to tenth order caused fitting problems in the low intensity regions. Inverse-intensity-squared weighting resulted in considerable improvement. Inverse-intensity-cubed worked even better and was adopted for 100 μm. Letting I^p represent the path intensity and I^x the crossing intensity, the weighting factor (W) is defined as follows:

$$W = 1/(I^{max}/I^{bar})^3$$

$$I^{max} = \mathrm{MAX}(|I^p|, |I^x|)$$
$$I^{bar} = 2.5 \times 10^{-7}\ \mathrm{Wm^{-2}sr^{-1}}$$
$$W < .01 \rightarrow W = .01$$
$$W > 10. \rightarrow W = 10$$

The 100 μm fit was done in three iterations with the order-of-fit table, rejection thresholds and α settings the same as at 60 μm. All the comments regarding gain errors and residual hysteresis made about the 60 μm fit are even more applicable to the 100 μm.

As with the 60 μm fits, the 100 μm fits should be considered questionable within 1° to 2° of the Galactic plane.

D.5 Monitoring

Algorithm performance was carefully monitored throughout the fitting process. The global RMS values of intensity differences as a function of iteration number are tabulated in Table D.4 for each wavelength. The RMS is reduced with each iteration but the amount of reduction is less each time. The RMS value after the last iteration at each wavelength is an extrapolated rather than a measured value. This is because the considerable computer time required to obtain the difference statistics was not significantly less than required to do another iteration.

Table D.4

RMS of Intensity Differences as a Function of Iteration

Wavelength (μm)	Iteration	RMS Difference (MJy sr^{-1})	% Reduction
12	0	0.616	—
	1	0.410	33.4
	2	0.334	45.8
	3	0.306	50.3
	4	[0.296]	[51.9]
25	0	1.178	—
	1	0.717	39.1
	2	0.541	54.1
	3	0.476	59.6
	4	0.435	63.0
	5	[0.404]	[65.7]
60	0	0.672	—
	1	0.437	35.0
	2	0.295	56.1
	3	[0.242]	[64.0]
100	0	1.785	—
	1	1.117	37.4
	2	0.900	49.6
	3	[0.811]	[54.6]

Note: Items within brackets are results from extrapolation of previous values.

Intensity difference plots, some of which have already been shown, provided good visibility on a scan-by-scan basis. Comprehensive checking using plots alone was not feasible due to the prohibitive number of detector/scan combinations. Instead, a program was written that computed a set of parameters that served as indicators of possible fitting problems. The following parameters proved most useful:

1) variance of fit for detector-scan
2) absolute value of fit at each extreme point
3) absolute value of fit slope midway between each extreme point pair as well as at each end point
4) absolute value of 2^{nd} derivative of fit at each extreme point
5) number of points rejected in detector-scan.

Histograms were generated for each parameter and detector-scan with extreme parameter values written into the Problem Scan Summary File (PSSF). Detector-scans identified as anomalous from other sources (see Appendix C) were written into the PSSF as well. The file was then used to establish namelists for making large numbers of intensity difference plots. The plots were manually inspected and the scans actually causing difficulties were identified. For the identified scans, problem type, severity and affected time interval were determined and loaded back into the PSSF.

During the fitting process a file of rejected intensity differences was generated. Using this file, all-sky maps like the one in Figure D.6 were plotted to show the global position of rejects. It was found that rejects were concentrated in high-intensity regions. The Galactic plane is prominent in all four bands; exceptionally bright areas such as found in Orion, Cygnus and Ophiuchus also show up. The rejects scattered over the sky are associated with bright point sources. The long strings of rejects are due to problem scans which had to be corrected or eliminated.

Problems identified from the intensity difference plots were divided into different types based on characteristic signatures. The types can be grouped into three categories, which map as follows into two of the three broad anomaly classes previously discussed (§D.3):
1) problems introduced into the data stream prior to BWDS processing that could distort the BWDS fits (Class IA)
2) problems introduced into the data stream prior to BWDS processing which would not distort the BWDS fits (Class IB)
3) time intervals identified when the global BWDS fits should not be used for downstream processing (Class III).

Class II anomalies were eliminated prior to fitting. Residual effects from incompletely removed Class II anomalies were apparently small; none were identified on the intensity difference plots checked. It is possible that some of the scattering attributed to other causes may have resulted from incompletely removed Class IIs. Class IA anomalies which could be identified beforehand were also eliminated prior to fitting. Pre-fit identification of these anomalies came from the original images as well as the latest calibration and pointing reconstruction processing.

Figure D.7 illustrates a serious Class IA anomaly. This particular anomaly affects all detectors in all bands and is believed to be the result of a paint flake passing in front of the focal plane. If not removed, it would not only distort the fit (solid line in figure) for the observation in which it occurs but could also adversely affect the crossing scan fits. This

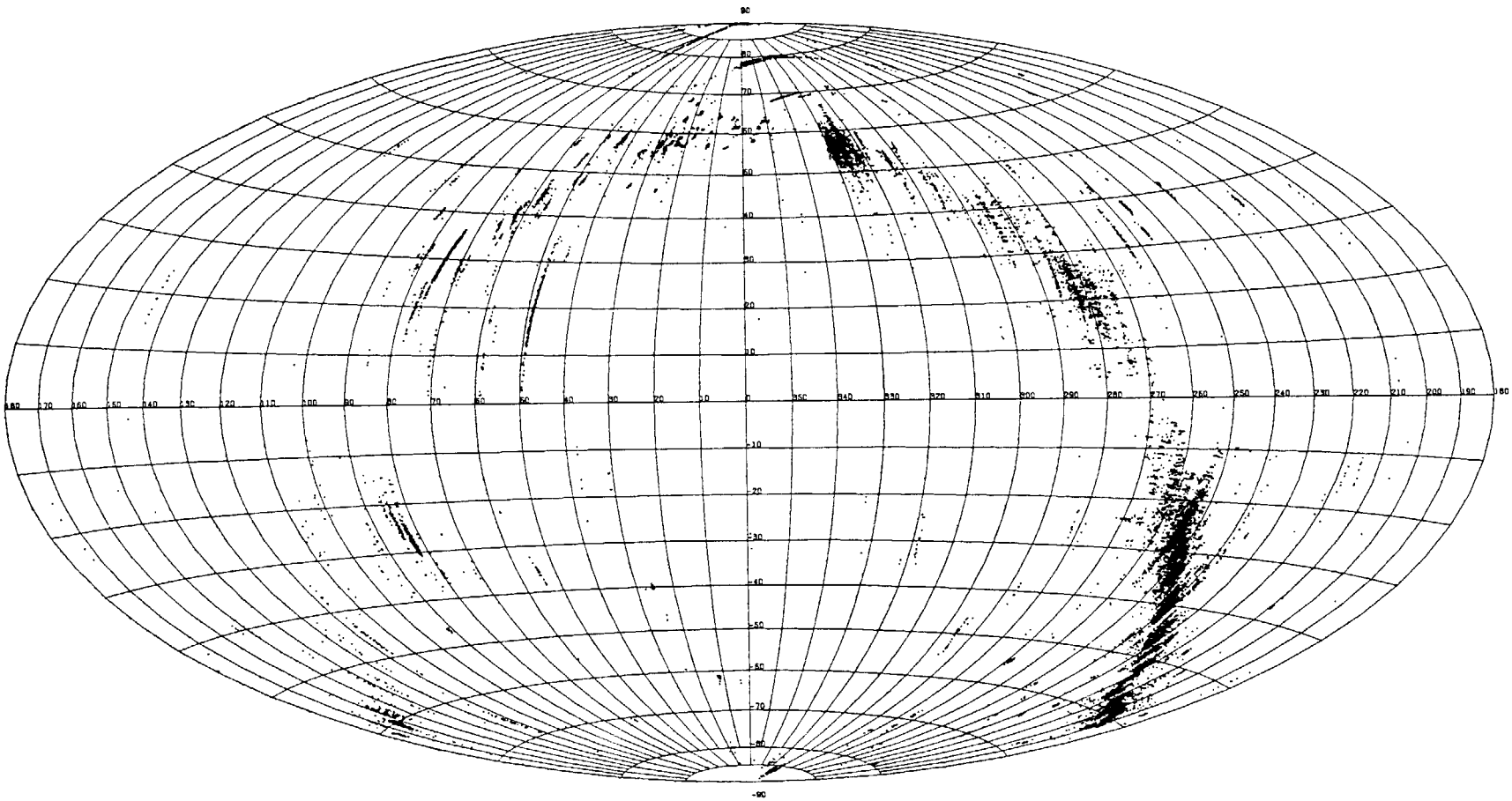

Figure D.6 Plot in ecliptic coordinates of points rejected by the global destriper for detector 42 (25 μm).

type of anomaly, once identified, was flagged for non-use not only in the BWDS database but for all downstream processors as well.

Figure D.8 illustrates a typical Class IB anomaly. It is caused by incompletely removed hysteresis as the affected scan crosses a very bright point source. This type of anomaly sometimes shows up as a double spike with positive and negative components on either side of the point source crossing. Since the crossing scans may also be affected by the point source, the signature on the intensity difference plots depends on the mix of ascending and descending scans. These anomalies were not removed from the BWDS database because they have too high a spatial frequency to appreciably affect the fit. It should be remembered by the user, however, that intensities in areas immediately surrounding bright sources are suspect.

A typical Class III anomaly was shown in Figure D.5(a). Had it not been possible to improve the fit with a combination of higher order and dual-hemisphere techniques, the time periods where the fit differed appreciably from the intensity differences would have gone into the PSSF as Class III anomalies. As illustrated by the figure, there is a tendency for the polynomial fits occasionally to flair off near the ends when heavily stressed elsewhere. To help locate potential problems of this type, fits having an extreme point within a plate width of an end point (start or finish) were identified and the intensity difference between the two saved. Time intervals where the magnitude of intensity difference exceeded 14.0 MJy sr^{-1} or the end point slope exceeded 0.2 MJy sr^{-1} were flagged for local fit only.

Another type of Class III anomaly is illustrated in Figure D.9. This type of problem can occur when there is a large internal gap in crossing times within a detector-scan. Since there are no crossing points to constrain the fit within the gap, it is possible for large excursions to occur within that region. Whether it happens depends not only on the size of the gap, but also on how stressed the fit is outside the gap.

An automated approach was developed to help identify detector-scans with the potential for this type of problem. First, the longest gap in each detector-scan was identified. Second, those detector-scans whose polynomial fits contained an extreme point within the gap period were marked. Next, the polynomial fit was evaluated at each end of the gap to provide the end points needed for a linear interpolation across the gap. Differences between the actual fit values at the marked extreme points and the linearly interpolated values were computed.

Those gap times with difference-from-linear magnitudes greater than 1.0 MJy sr^{-1} were flagged for local destriper only. The one exception to this was in the dual-hemisphere overlap region at 25 μm where the near-linear assumption does not apply.

In order to maintain relative photometry across a plate, the frequency of the fits had to remain low. The intent was that it should not be possible to introduce artifacts or to remove real structure smaller than 12.5°. Order-of-fit criteria were selected so that extreme points would be separated by more than a field width. There is, of course, nothing to prevent an individual polynomial fit from having rapid fluctuations over a portion of

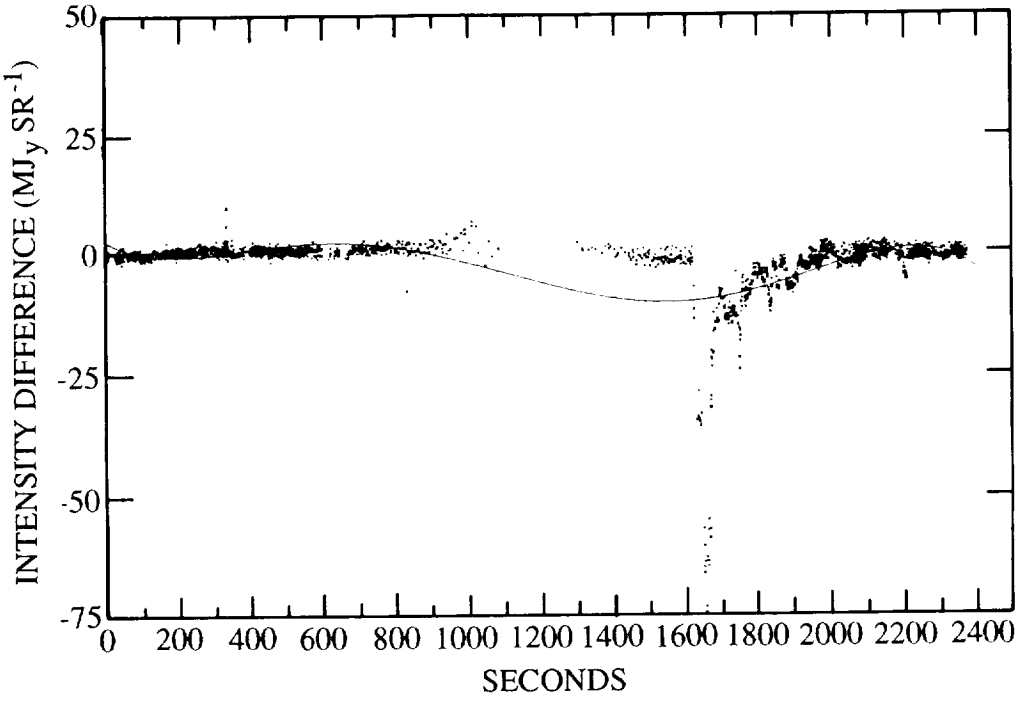

Figure D.7 Intensity differences along a detector-scan track illustrating a class IA anomaly.

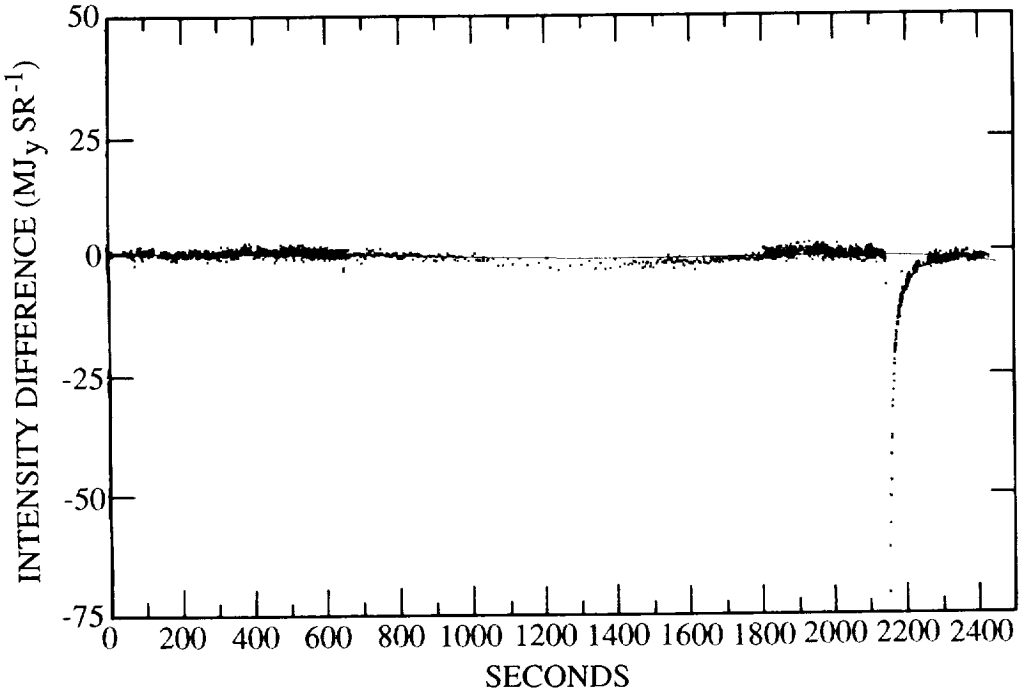

Figure D.8 Intensity differences along a detector-scan track illustrating a class IB anomaly.

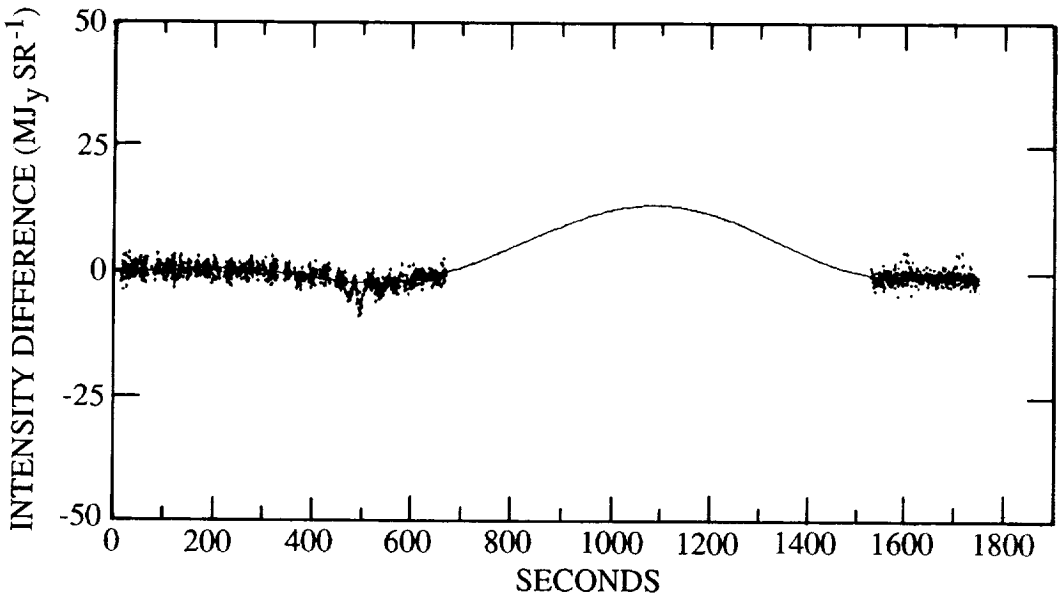

Figure D.9 Intensity differences along a detector-scan track illustrating a class III anomaly.

the scan. The real question is whether the individual scans involved combine in such a way as to introduce artifacts or remove real structure. In order to address this question, those fits with extreme point pairs closer than a plate width having intensity differences greater than 1.0 MJy sr^{-1} were identified. The global positions of the scan legs between the identified extreme point pairs are plotted for the 100 μm fits in Figure D.10.

In areas with many identified close extreme point pairs, the global BWDS contribution to the image was subtracted out and manually inspected for adverse effects.

As has been previously described, every effort was made to identify fit problems through the method of automated checking of indicator parameters coupled with manual inspection of indicated scans. However, some problem fits will have slipped through the screen. We can be confident that the individual problem fits slipping through the BWDS monitoring were not severe in nature. The greater danger is that a number of small fitting errors slipped through which were systematically wrong in the same direction and sky position. By far the most likely place for this to happen is at the scan end points, which occur near the ecliptic poles. To guard against these dangers, images of every plate were checked manually (§III.D). In areas where there are many scan ends, the global BWDS contribution to the image was subtracted out and manually inspected for such effects.

References

Emerson, D. T. and R. Gräve 1988, *Astron. Astrophys.*, **190**, 353.

IRAS Catalogs and Atlases: Explanatory Supplement 1988, ed. C. A. Beichman, G. Neugebauer, H. J. Habing, P. E. Clegg, and T. J. Chester (Washington, D.C.:GPO).

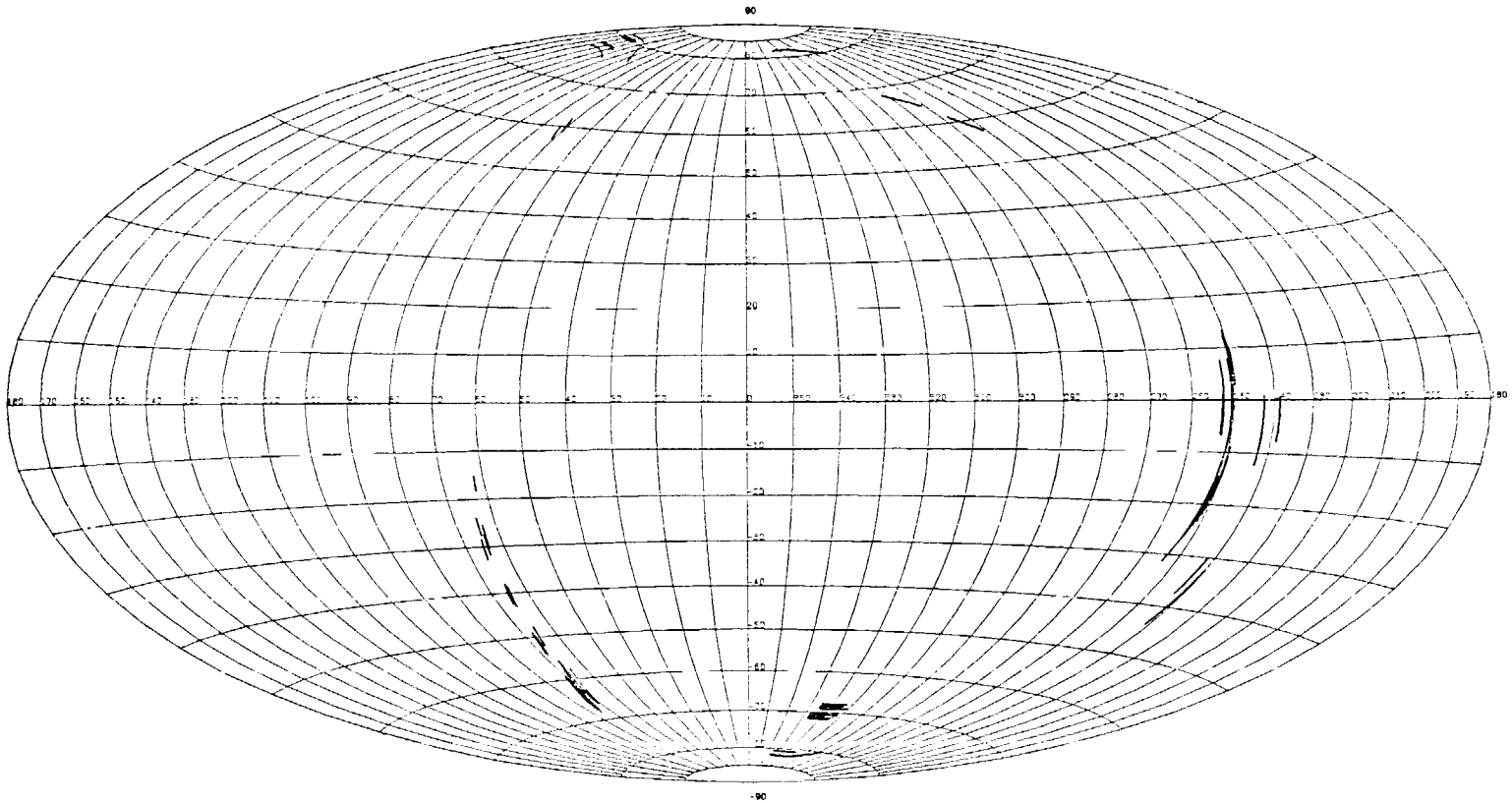

Figure D.10 Scan segments that have close extreme point pairs for 100 μm fits plotted in ecliptic coordinates.

APPENDIX E

Gain Errors

As discussed in Appendix D, the BasketWeave DeStriper (BWDS) makes use of intensity difference histories. These histories were generated by comparing the intensities from a given detector with the intensities of all other detectors of the same band which cross the path of the first detector at any time during the mission.

These intensity difference histories revealed a correlation between the magnitude of differences and intensity, suggesting gain errors. The average percentage gain error was computed from intensity difference data for each detector at 100 μm. This was done by using the intensity-weighted differences which, at 100 μm, gave more importance to the detector differences near the Galactic plane. The intensity differences were converted to percentage gain errors using the intensities from the crossing detectors. Only intensities with the zodiacal foreground removed were readily available. This was considered viable for 60 and 100 μm since the emission due to the zodiacal dust is a small percentage of total emission near the Galactic plane at these wavelengths.

The average gain errors and associated population sigmas at 100 μm, broken down by detector, were computed as shown in Table E.1. A positive sign suggests that the intensities for that detector are too large relative to other detectors in the band and should be reduced by the indicated percentage. A negative sign suggests that the intensities for that detector are too small relative to other detectors in the band and should be increased by the given percentage. These adjustments were *not* applied to the IRAS data.

Table E.1

100 μm Gain Errors

Detector	01	02	03	04	05	06	07	56	57	58	59	60	61
Gain Err (%)	+11	+01	+06	-05	+11	+04	+15	-01	+02	-01	-20	-05	00
Pop. Sig (%)	8.0	5.1	5.5	6.2	7.8	5.2	7.1	6.2	5.5	6.1	5.0	7.1	6.9

The analysis was repeated for 60 μm using a subset of the IRAS survey data known as the mini-survey (*IRAS Explanatory Supplement 1988* §III.C.11). Results are tabulated in Table E.2.

Table E.2

60 μm Gain Errors

Detector	08	09	10	12	13	14	15	32	33	34	35	37	38
Gain Err (%)	+10	-02	-09	+09	+02	-06	+13	+08	+03	-05	+09	-03	-23
Pop. Sig (%)	3.8	3.2	3.3	9.2	2.9	5.0	5.9	3.0	4.0	3.4	4.2	3.9	5.2

These values do not fluctuate with Galactic longitude, which suggests that they are *not* a function of photon exposure and therefore are *not* due to hysteresis. The values

presented above are expected to approximate DC gain errors. To a lesser extent, they may also reflect errors in determination of the detector solid angles.

Residual hysteresis effects were also noted in all bands. These were relatively short-lived with time constants roughly of the order of 10 to 20 seconds.

References

IRAS Catalogs and Atlases: Explanatory Supplement 1988, ed. C. A. Beichman, G. Neugebauer, H. J. Habing, P. E. Clegg, and T. J. Chester (Washington, D.C.:GPO).

APPENDIX F

Gain and Offset Corrections

F. Boulanger

A file containing corrections, gains and DC offsets, accompanies the *IRAS Zodiacal History File* (ZOHF) Version 3.0. A description of how the corrections were derived is presented below along with statistics on the corrections.

Version 3.0 ZOHF was used to compute average profiles of the zodiacal emission versus inclination (azimuth angle about the Earth-Sun axis) for the entire IRAS dataset following the method described in Boulanger and Pérault 1988. A zodiacal light profile was computed for each scan by linear interpolation of the nearest average profiles. It was assumed that the zodiacal light dependence on elongation and time was linear between two consecutive average profiles. Gain and DC offset corrections were obtained for each scan by deriving a linear correction that forced the lower envelope of the scan to match the zodiacal light profile computed for that scan. This fitting process was iterated three times, discarding all points with residuals larger than 5σ from one iteration to the next. These corrections force the scan to match the average zodiacal light measured by all scans with the same SOP (Survey Observing Plan, roughly a half day of observations) and elongation.

This procedure is valid only if the correction fit is made over data points for which the Galactic emission is negligible compared to the magnitude of the corrections, which are typically a few percent of the zodiacal emission. This condition was satisfied by using only points at high Galactic latitude ($|b| \geq 25°$), where a good correlation exists between the IR and H I emission (Boulanger and Pèrault 1988). The Galactic emission in this region is negligible compared to the zodiacal light at 12 and 25 μm and the Galactic contribution at 60 μm was removed using H I data (Boulanger and Pèrault 1988). No correction factors were derived at 100 μm due to the variations in the IR-H I correlation across the sky, which prevented subtraction of the Galactic emission with sufficient accuracy.

Correction factors were measured only for scans for which at least 60 data points (30° of scan length) satisfy the selection criteria for low Galactic emission described in the previous paragraph. Therefore, no gain and offset corrections were obtained for short scans and scans which have too few points in regions of low Galactic emission. The file gives correction factors for about 80% of the scans longer than 30°. Statistics on the gain and offset corrections are presented in Tables F.1 and F.2. Table F.1 gives the average value and the root mean square dispersion of the gain and offset corrections. At all wavelengths the average gain and offset corrections are close to one and zero, respectively. This shows that the corrections do not change the overall calibration of the data. The root mean square dispersion of the gain corrections is about 3% for each of the three wavelengths. Table F.2 gives a histogram of the gain corrections. The gain and offset corrections are plotted against SOP and elongation in Figures F.1(a) – (c). These figures show that there is no systematic effect in the corrections with respect to elongation and SOP.

References

Boulanger, F. and M. Pérault 1988, *Ap. J.*, **330**, 64.

Table F.1
Statistics of Correction Factors

λ (μm)	Number of Scans			Offsets (MJy sr^{-1})		Gains		Residuals (MJy sr^{-1})
	(1)	(2)	(3)	(4)	(5)	(6)	(7)	(8)
12	3616	2133	0	-0.105	0.482	1.004	0.030	0.114
25	3617	2132	0	-0.125	0.835	1.001	0.032	0.172
60	3384	2295	70	0.036	0.403	0.994	0.036	0.162

(1) number of scans with a good fit (correlation coefficient larger than 0.96)

(2) number of scans without a fit; most of these are short scans

(3) number of scans with a poor fit (correlation coefficient smaller than 0.96)

(4) average offset correction

(5) standard deviation of offset corrections

(6) average gain correction

(7) standard deviation of gain corrections

(8) average amplitude of residuals (RMS dispersion) after subtraction of the fit

Table F.2
Histogram of Gains

Range	Number of Gains		
	12 μm	25 μm	60 μm
<0.955	69	196	330
0.955–0.965	79	158	166
0.965–0.975	141	173	220
0.975–0.985	324	308	360
0.985–0.995	670	564	474
0.995–1.005	854	665	606
1.005–1.015	628	546	538
1.015–1.025	356	448	358
1.025–1.035	184	248	134
1.035–1.045	81	118	59
>1.045	230	193	139
Total	3616	3617	3384

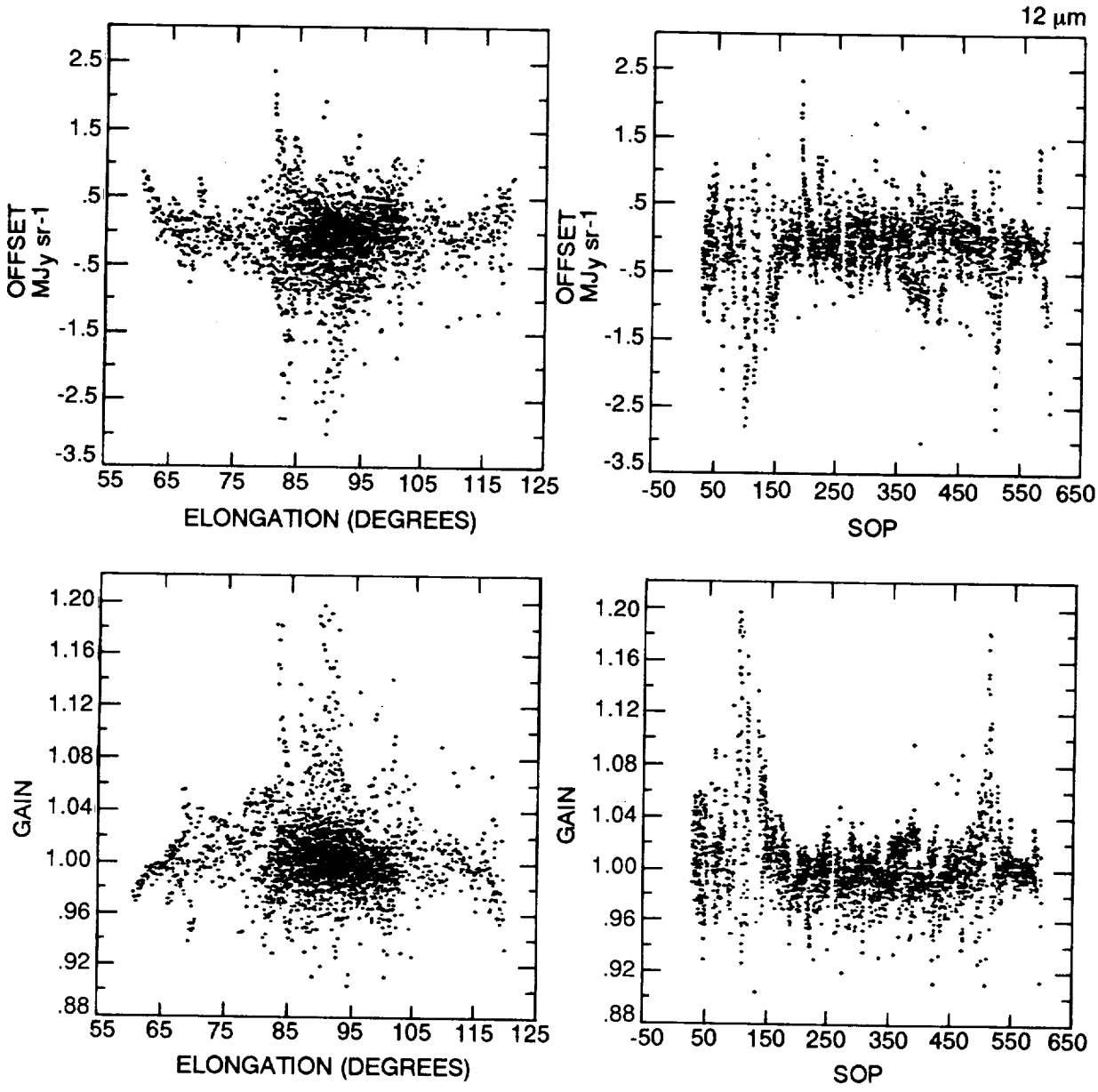

Figure F.1(a) Gain and offset corrections versus elongation and SOP, 12 μm

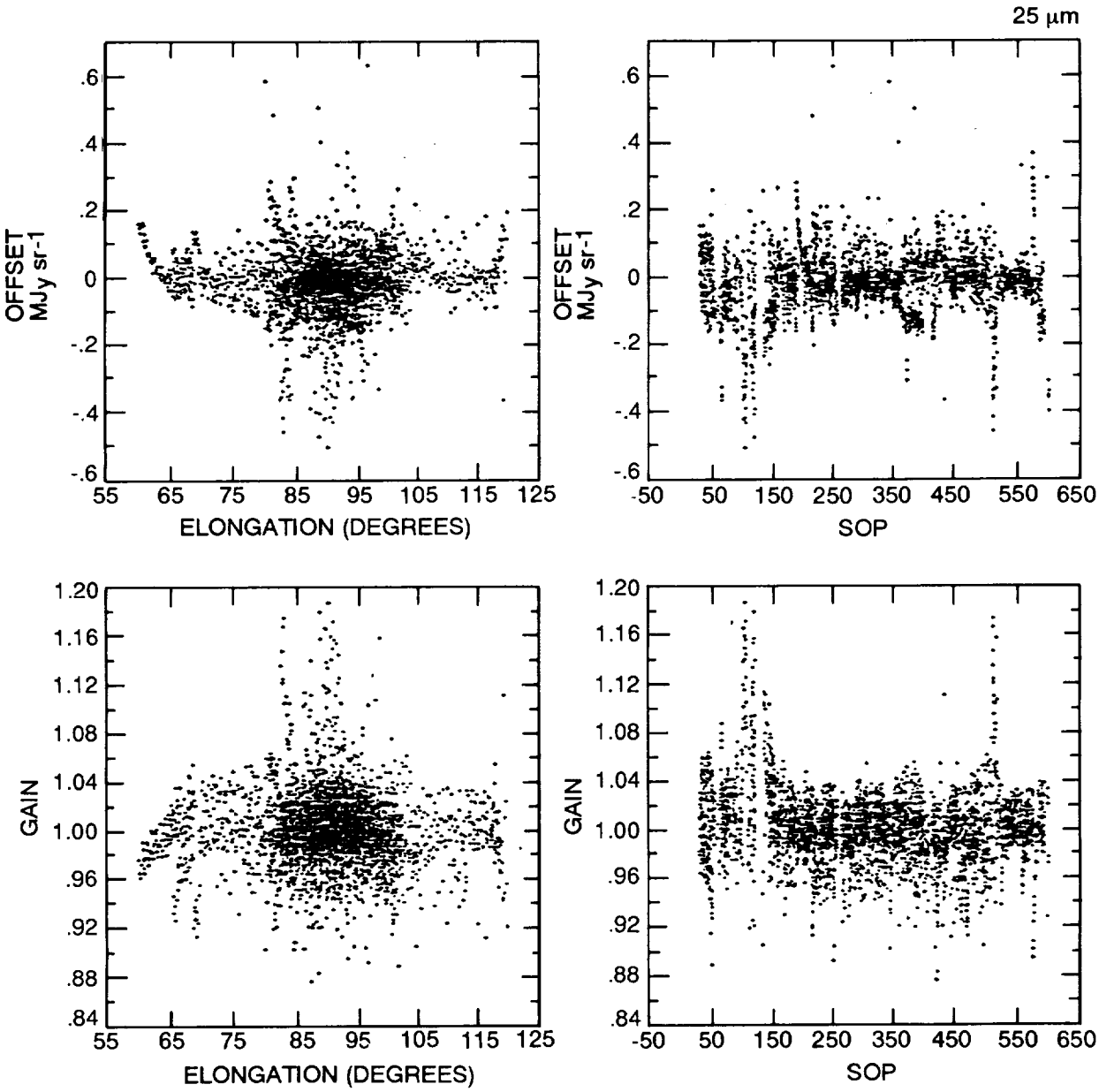

Figure F.1(b) Gain and offset corrections versus elongation and SOP, 25 μm

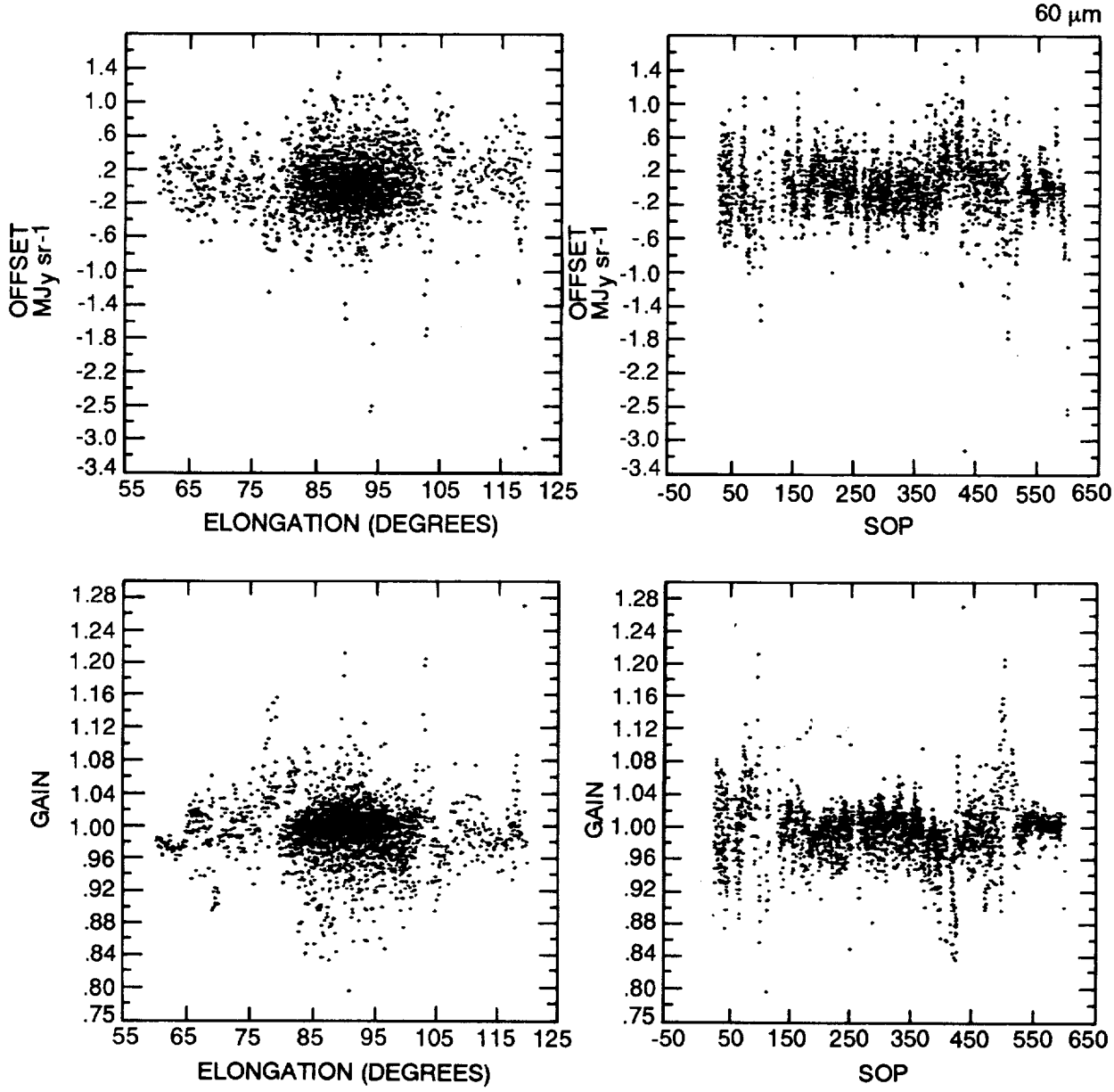

Figure F.1(c) Gain and offset corrections versus elongation and SOP, 60 μm

APPENDIX G

Zodiacal Dust Cloud Modeling Using IRAS Data

J. Good

G.1 Overview

A physical model for the interplanetary dust cloud was fit to the IRAS data. This model consists of spatial distributions for the dust volumetric emissivity and temperature, an inclination and line of nodes for the cloud, and a simple parameterization of the dust emissivity as a function of wavelength. The volumetric emissivity was found to vary as $r^{-1.8} \times \exp[-4.97(|z|/r)^{1.26}]$ and the temperature as $R^{-0.36}$, where R is the radial distance from the Sun in spherical coordinates, r is the radial distance from the Sun in cylindrical coordinates and z is the distance from the plane of symmetry of the dust. This density drop-off differs from the $r^{-1.3}$ power law for the dust density deduced from Helios measurements of scattered sunlight, but the discrepancy can be explained if the albedo of the dust decreases with heliocentric distance.

The IRAS data are limited to solar elongation angles between 60° and 120° and consequently are not sensitive to material closer to the Sun than about 0.9 AU. However, comparison of the predicted model flux and Zodiacal Infrared Project (ZIP) data (Murdock and Price 1985) which looked to within 22° of the Sun at 10 and 20 μm shows excellent agreement in shape (Figure G.1), though there is a calibration scale discrepancy. It also implies that the $r^{-1.8}$ power law is good to 0.4 AU. The inclination of the zodiacal dust cloud is 1.7° and its line of ascending nodes is at 69° ecliptic longitude, substantially different from the 3.4° and 87° deduced from the Helios measurements. However, since the Helios measurements were made between 0.3 and 1 AU and the IRAS data is primarily sensitive to material outside 0.9 AU, we attribute these differences to variation of the cloud symmetry plane with heliocentric distance.

The model presented here is based on the IRAS data as understood after the final calibration. Preliminary comparisons of IRAS data with the COBE-DIRBE data suggests that the IRAS gains and offsets require small change (§IV.D.3 and DIRBE Explanatory Supplement, 19 July 1993). Consequently, the physical parameters determined for the zodiacal dust cloud need reinterpretation. However, the purpose here is to represent accurately the variability of the infrared background and the current model does that quite well.

G.2 Data

The IRAS data provide us with an unprecedented opportunity to investigate the zodiacal dust cloud. First, the sheer volume of data makes it possible to fit for a large number of dust cloud parameters unambiguously. Furthermore, the extremely high signal-to-noise allows differentiation and exclusion of Galactic IR structure. Finally, the spectral coverage (7–140 μm in four bands) allows concurrent extraction of temperature and emissivity information.

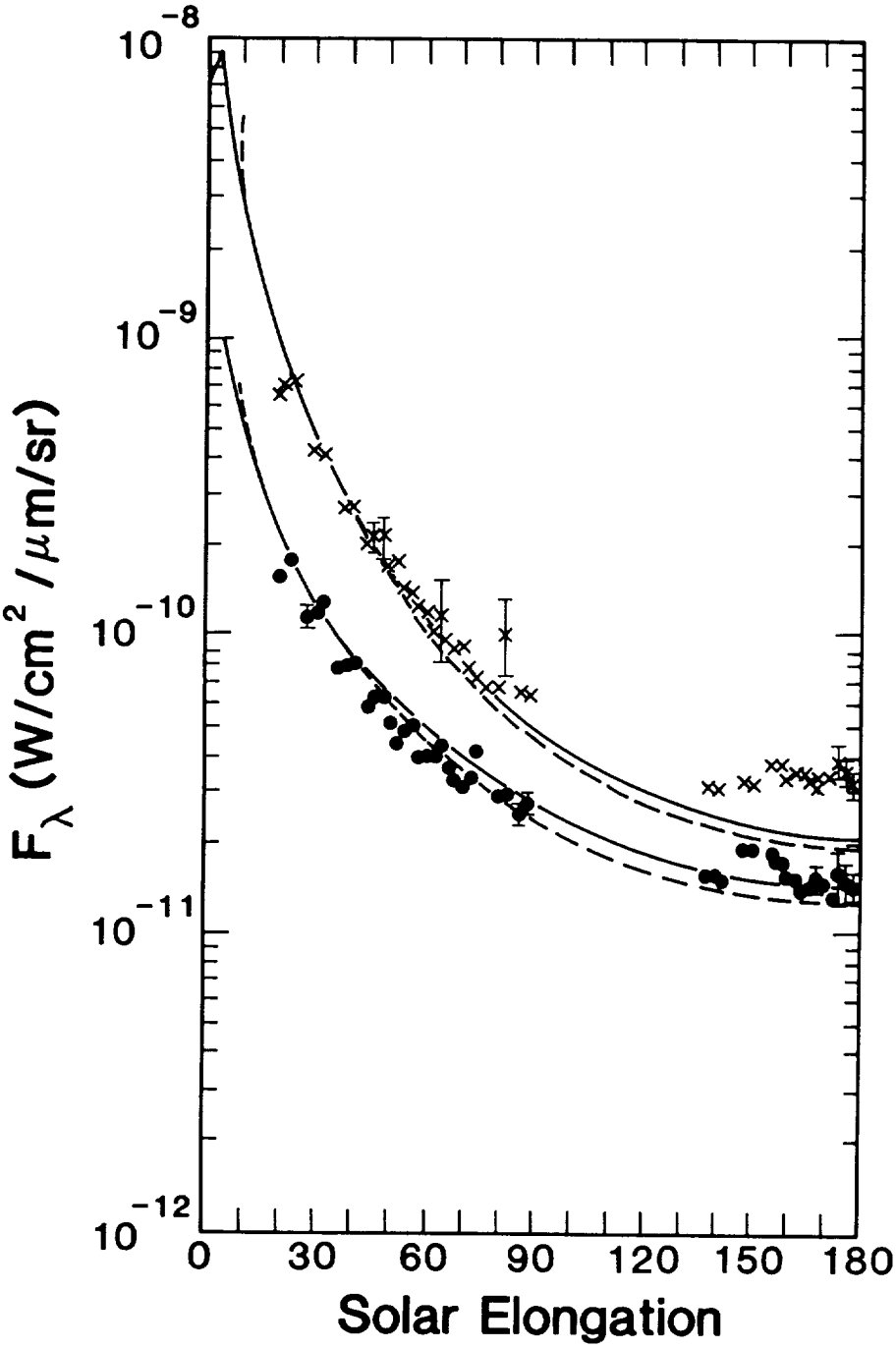

Figure G.1 ZIP data (Murdock and Price 1985) showing zodiacal brightness in the ecliptic plane as a function of solar elongation. The dashed curve represents the predicted flux (scaled by a factor of 1.5) from the zodiacal dust cloud model.

The IRAS satellite was placed in a near-polar orbit of 99° inclination oriented with the orbital plane roughly normal to the Sun-Earth vector (Figure G.2). The orbit precessed through the year to maintain constant orientation to the Sun. Thus the nominal scan path during an orbit pointed directly away from the Earth and traced a line from ecliptic pole to ecliptic pole in a plane 90° away from the Sun. In practice, however, during any given half orbit (i.e., from one pole to the other) the satellite was tilted either toward or away from the Sun by varying amounts. It then swept out a cone on the sky at a constant angle from the Sun (the solar elongation angle) and with a constant azimuthal rate ($3.84'$ s^{-1}). The solar elongation varied by as much as $\pm 30°$ from normal but was usually within $\pm 10°$.

The azimuth angle (referred to as the inclination angle) is arbitrarily defined to be $-90°$ when the satellite passes the north ecliptic pole and increases in the direction of the scan. Since the descending part of the orbit occurred on the side of the Earth opposite the Earth's direction of motion (see Figure G.2), an inclination of 0° looks in the Earth's orbital plane back in the direction from which the Earth has come. Many of the coordinate angle references in this appendix (particularly on the plots) will be given in this solar elongation/inclination system.

The sky was observed through four wide bandpass filters, nominally centered at 12, 25, 60, and 100 μm (Figure G.3) (*IRAS Explanatory Supplement 1988*, §II.C). It is important for the modeling to use the exact bandpass shape, since temperature variations with heliocentric distance play an important role in the observed infrared flux. Consequently, fluxes will often be given in in-band $Wm^{-2}sr^{-1}$ and only converted to MJy sr^{-1} when appropriate.

Almost 6000 scans were made during the mission, about 1700 of which went from pole to pole. Of these, 200 scans were chosen which were representative of the range of solar elongations and which uniformly covered the time period of the mission. A typical scan is shown in Figure G.4.

The major portion of the flux seen at 12, 25, and 60 μm is due to the zodiacal emission we wish to model. The small local variations that are left are due to Galactic sources, which become dominant at 100 μm. It is important to note that these fluctuations are not noise (the noise is too small to show on these plots; the typical SNR is about 1,000). This proved to be a major problem in the fitting since it implied that the model should be fit to the local minima in a kind of "lower envelope" rather than the data as a whole. The method devised to handle this problem will be discussed in the section on fitting. At 100 μm there was almost no zodiacal emission on the sky that was not contaminated by a large amount of Galactic flux.

G.3 Description of Model

G.3.a *Density*

An adequate representation for the spatial distribution of the zodiacal dust is the most important factor in modeling of the observed infrared flux. A simple model for the variation of dust density with heliocentric distance (where the dust spirals in due to the Poynting-Robertson effect) would produce a radial distribution proportional to r^{-1} (Briggs

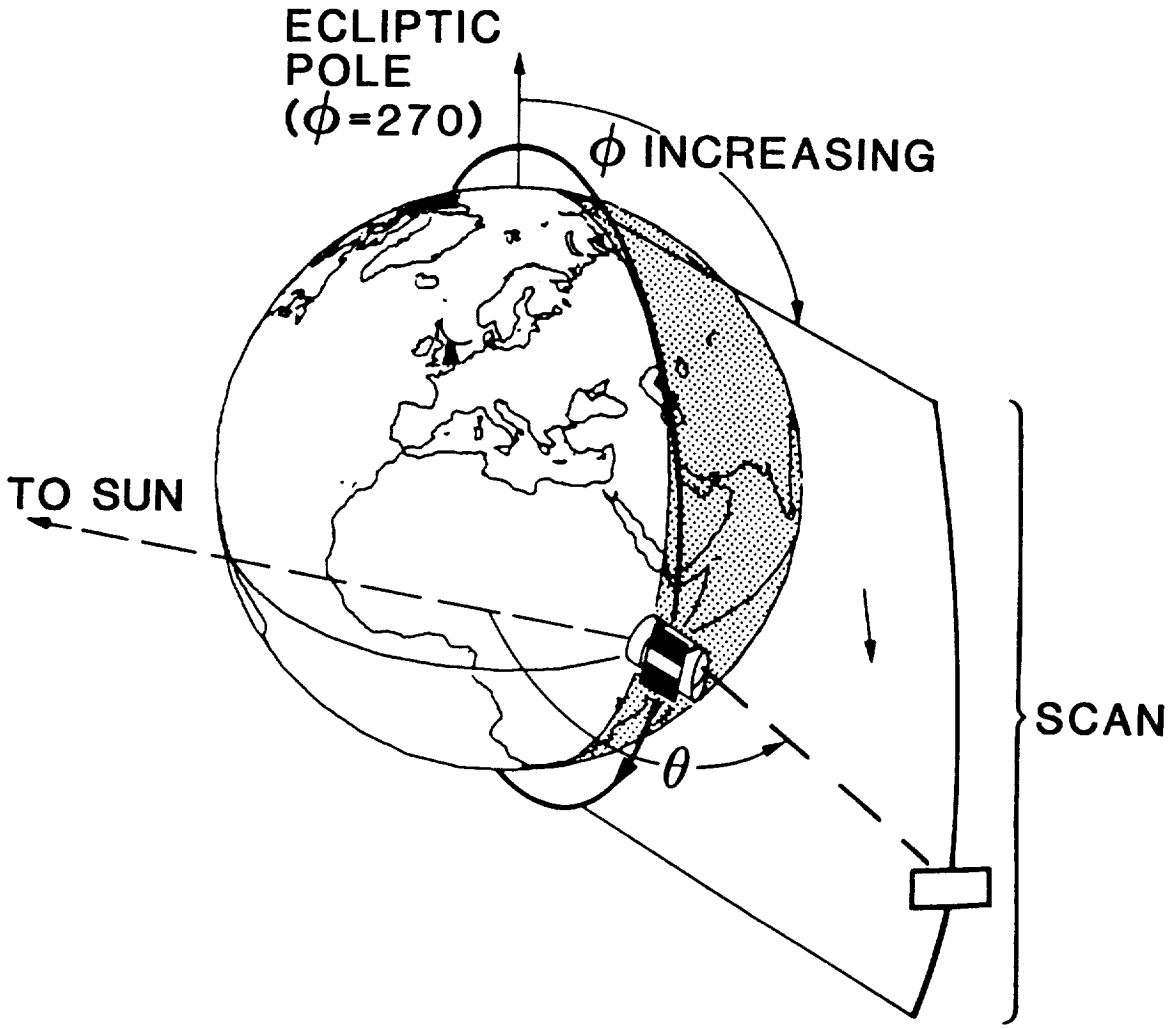

Figure G.2 The scanning geometry of the IRAS satellite is illustrated. The scan coordinate system is defined by the solar elongation angle θ, which remains fixed for a scan, and the inclination angle ϕ, which changes at a constant rate.

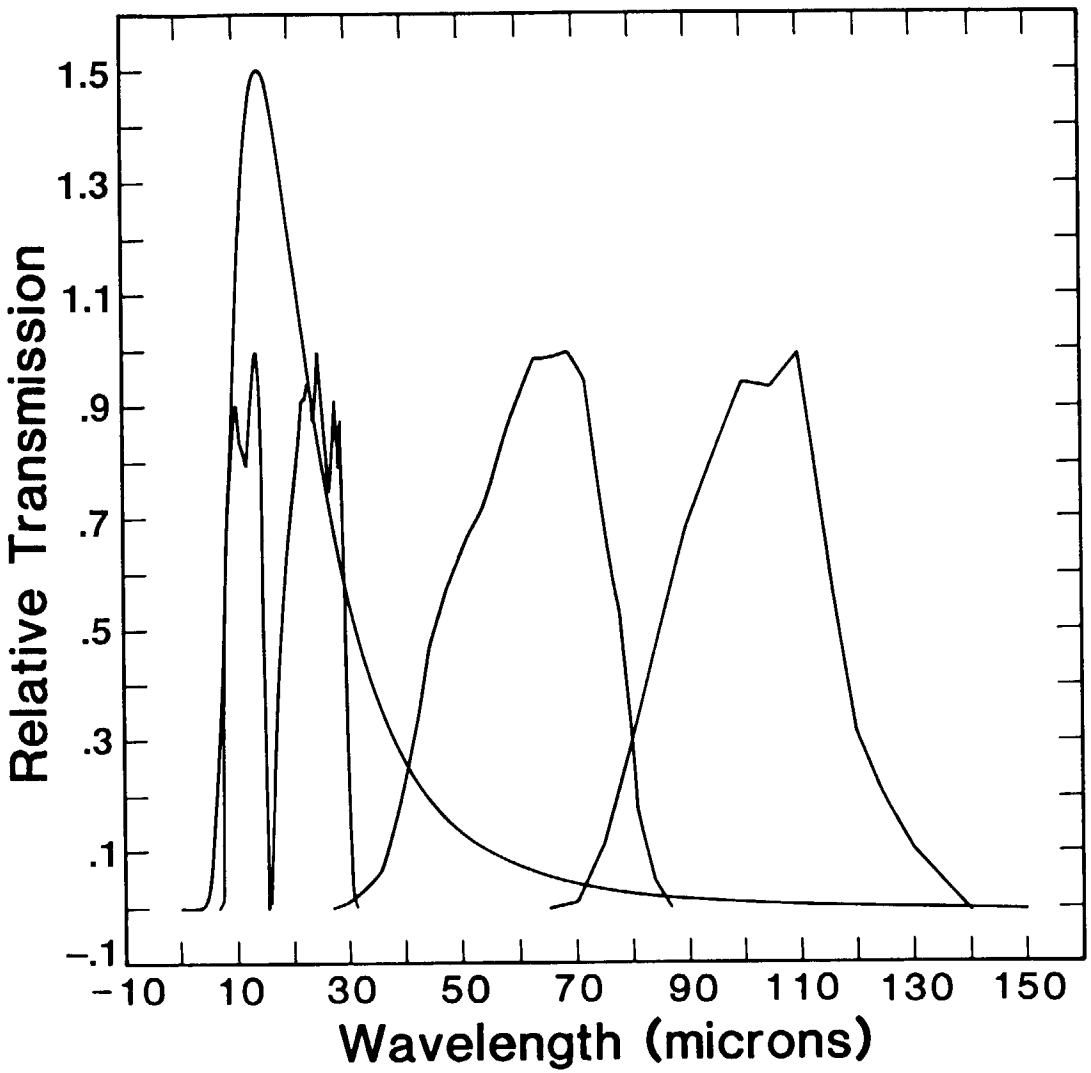

Figure G.3 The IRAS bandpasses and a 200 K blackbody, for reference.

1962). Models that include mutual collisions (Trulsen and Wikan 1980; Leinert *et al.* 1981) and perhaps Lorentz forces (Mukai and Giese 1984) produce distributions that vary as r^{-k} where $k > 1$. In this study the radial part of the density distribution is assumed to vary as $r^{-\alpha}$ where α is a free parameter (r is the radial component of the distance from the Sun in cylindrical coordinates).

The variation of density out of the plane of the ecliptic is less clear. To fit Helios data, Leinert *et al.*, (1978a) used a z-dependence of $\exp[-2.1(|z|/r)]$. Collision models (Trulsen and Wikan 1980) indicate that $\exp[-\beta r^2]$ might be more appropriate. In this study the z-dependence is assumed to be of the form $\exp[-\beta(|z|/r)^\gamma]$ where β and γ are free parameters.

In practice, we model not the density but the volumetric absorption cross-section $\rho(r,z)$. We will assume that the same functional form can be used, however, and complete our description of $\rho(r,z)$ with a reference value $\rho_o = \rho(R_o = 1\text{AU}, z = 0)$.

The complete description of the volumetric absorption cross-section is then

$$\rho(r,z) = \rho_0(R_0/r)^\alpha \times \exp[-\beta(|z|/r)^\gamma] \qquad \text{cm}^{-1} \tag{1}$$

where ρ_0, α, β, and γ are free parameters, $R_0 = 1$ AU, and (r,z) are cylindrical coordinates.

G.3.b *Temperature*

Gray particles (with diameters $\gg$ wavelength and constant albedo with heliocentric distance) when heated by the Sun will give rise to an equilibrium temperature that varies as $R^{-0.5}$. However, variation of properties with distance or wavelength will disturb this ideal case. Consequently, in this study we allow the temperature to vary as $R^{-\delta}$ where δ is a free parameter. The temperature at 1 AU (T_0) is also free. It is assumed that a constant δ with heliocentric distance is sufficient to deal with local dust properties.

The complete description of the temperature is

$$T = T_0(R_0/R)^\delta \qquad \text{K} \tag{2}$$

where T_0 and δ are free parameters (and R is the radial distance from the Sun).

G.3.c *Emissivity*

The emission behavior of solid particles in the infrared is complex and the breadth of the IRAS band passes precludes making any definitive statements about composition. However, it became clear from the fitting that a long wavelength emissivity drop-off was necessary to attenuate the 60 and 100 μm model predictions (a flat emissivity produced too much flux in these bands). Models of dust grain properties (Roser and Staude 1978) indicate that typical materials are reasonably constant in the 10 to 25 μm region but fall off as $\lambda^{-\eta}$ (where $\eta = 1 - 3$) for longer wavelengths. Consequently, this study has used an emissivity that is constant out to some cutoff (λ_0) and then drops as $\lambda^{-\eta}$. In practice, even this is a level of complication unwarranted by the data and the two parameters, λ_0 and η,

cannot be fit simultaneously (they are too strongly correlated). We therefore arbitrarily chose to let $\eta = 1$ (Mie theory for spherical particles). This approximation will be shown to have no effect on any of the parameters other than λ_0.

The complete description of our model for the emissivity is

$$\epsilon = \begin{cases} \epsilon_o & \lambda \leq \lambda_0 \\ \epsilon_0(\lambda/\lambda_0)^{-1} & \lambda > \lambda_0 \end{cases} \tag{3}$$

where λ_o is a parameter. In practice, ϵ_0 is an unknown and will be subsumed by n_o, the volumetric absorption cross-section.

G.3.d *Cloud Orientation*

The zodiacal dust cloud is assumed to be azimuthally symmetric but is allowed to have an inclination relative to the ecliptic. This introduces two more free parameters: the inclination angle i and the line of ascending nodes Ω. The assumption of azimuthal symmetry will be in error if the cloud is warped and thus has different inclinations/lines of nodes in different parts of the solar system (Misconi 1980). We should, however, be able to detect the presence of such discrepancies in the residuals to the fit as a function of solar elongation.

G.3.e *Constant Background*

It became apparent during the fitting that the shape of the zodiacal emission could only be fit if a baseline offset were introduced in each band. The origin of this extra flux is unclear; it could be a calibration offset, or it might represent an isotropic background component on the sky. A detailed comparison with the ZIP (Murdock and Price 1985) or COBE data may resolve this uncertainty.

G.3.f *Model Parameters*

There are thus a total of fourteen free parameters in our model (four for the density, two each for the temperature, the emissivity, and the cloud orientation, and four for the background). However, as mentioned previously, it is impossible to derive values for both of the emissivity parameters simultaneously and, therefore, the total number of parameters is reduced to 13. Although this number of parameters may seem excessive, the number of degrees of freedom is large [$\approx$ 200 (scans)$\times$360 (samples)$\times$4 (bands)]. It will be shown that these parameters are sufficiently uncorrelated to make a unique solution possible.

G.4 Fitting Procedure

It is relatively simple to generate a model that is capable of fitting one wavelength of one scan. Such a fit gives a moderately good estimate of the parameters defining the z-dependence of the density but does not do well on the radial dependence of density or temperature and is insensitive to the cloud inclination and line of nodes.

To determine the cloud orientation parameters requires several scans spread out over the full time range of the mission (equivalently, the range of Earth orbital longitudes).

In addition, to determine accurately the radial dependence of density and temperature requires the use of the full range of solar elongation angles. Finally, to constrain fully the temperature and to estimate the emissivity properties we must fit all four bands at once. Preliminary fitting with a subset of our model and of the data (Good, Hauser and Gautier 1986) gave credible values for those parameters fit but with much higher uncertainties than the present effort and with a poorer fit (further emphasizing the need for the full parameter set).

In addition to its inability to constrain all the model parameters, a single scan is contaminated by some unknown amount of Galactic light. It is impossible to separate out a smooth Galactic component in one scan, but if two scans covering the same position on the celestial sphere are observed at different times (i.e., through different amounts of the zodiacal dust cloud), fitting to both scans simultaneously will implicitly be sensitive to time variability, which can only be due to the cloud.

We are therefore forced to the conclusion that an accurate derivation of the cloud parameters requires simultaneous fitting to the full subset of scans described above. The procedure used in the fitting is a) to generate model estimates of all 200 scans using a given set of model parameters, and b) to adjust the parameters using the method of least squares until the best fit is achieved.

The flux integral along any line-of-sight is given by

$$F_{\lambda_0}(\theta,\phi,t) = \int_{\lambda_{\min}}^{\lambda_{\max}} R_{\lambda_0}(\lambda) \left[\int_0^{\ell_\infty} \rho(r_c, z_c) B_\lambda\big(T(R)\big) d\ell \right] d\lambda \qquad (4)$$

where θ and ϕ are the elongation and inclination of the observation, $\rho(r,z)$ and $T(R)$ are as described above [with $(r_c, z_c$ in cloud coordinates, not ecliptic)]. $B_\lambda(T)$ is the Planck function, $R_{\lambda o}(\lambda)$ is the spectral response of the detector/filter combination with nominal wavelengths λ_o = (12, 25, 60 or 100 μm) and ℓ is the unit vector in the direction (θ,ϕ) at time t. Positions in (r_c, z_c)-space are calculated from (ℓ,θ,ϕ) taking into account the orbital position of the Earth at time t (including eccentricity of the Earth's orbit) and the orientation of the dust cloud.

To generate the model scans, the flux from the model cloud was integrated along several lines of sight and over the bandpass. Thirteen reference points were used for each scan, spread out between inclination angles $-90°$ and $+90°$ but concentrated toward the ecliptic plane where the variation was most extreme. The resultant flux for the reference points was interpolated, using a cubic spline under tension, to give model fluxes for each of the real data points. The difference between this interpolated function and a full flux integration is typically less than 0.05%.

Each parameter in the model (the thirteen described above) was then perturbed slightly. The variations of the model with respect to these perturbations and the differences between the nominal model and the real data were then combined to generate updates to the estimated model parameters. This procedure was iterated until the parameters converged.

As mentioned previously, the fluctuations above the zodiacal background are not noise but Galactic structure. Consequently, those points that are strong positive excursions from the model (when the model has become reasonably accurate) should be given a very low weight to exclude the galaxy and the zodiacal dust bands. Such a weighting can be incorporated into the least-squares process since an uncertainty for each point is part of the scheme. Without this "lower envelope" approach the fit would be biased, especially at the longer wavelengths, by the Galactic emission.

G.4.a *Model Results*

The results of fitting our model to the 200 scans are shown in Table G.1 and the coefficients of correlation between the parameters are shown in Table G.2. Representative scans (for several elongations and times) are shown in Figures G.4, G.5 and G.6. Considering the number of parameters, even the highest of the correlations (0.91, between the power law exponents on ρ and T) is quite small. We therefore conclude that the inclusion of all the free parameters in our model is justified and, moreover, that they are all required to fit the data properly.

Table G.1

Model Parameter Values and Uncertainties

Class of Parameter	Values of Parameters	Units
Density	$\rho_0 = 1.439 \pm 0.004 \times 10^{-20}$	cm^{-1}
	$\alpha = 1.803 \pm 0.014$	unitless
	$\beta = 4.973 \pm 0.024$	unitless
	$\gamma = 1.265 \pm 0.003$	unitless
Temperature	$T_0 = 266.20 \pm 0.18$	Kelvin
	$\delta = 0.359 \pm 0.004$	unitless
Emissivity	$\lambda_0 = 37.75 \pm 0.09$	μm
	$\eta = 1$	(fixed)
Orientation	$O = 68.61 \pm 0.03$	degrees
	$i = 1.73 \pm 0.01$	degrees
Offsets	12 μm $= 35.53 \pm 0.15 \times 10^{-8}$	$Wm^{-2}sr^{-1}$
	25 μm $= 49.97 \pm 0.14 \times 10^{-8}$	$Wm^{-2}sr^{-1}$
	60 μm $= 2.19 \pm 0.03 \times 10^{-8}$	$Wm^{-2}sr^{-1}$
	100 μm $= 5.24 \pm 0.07 \times 10^{-8}$	$Wm^{-2}sr^{-1}$

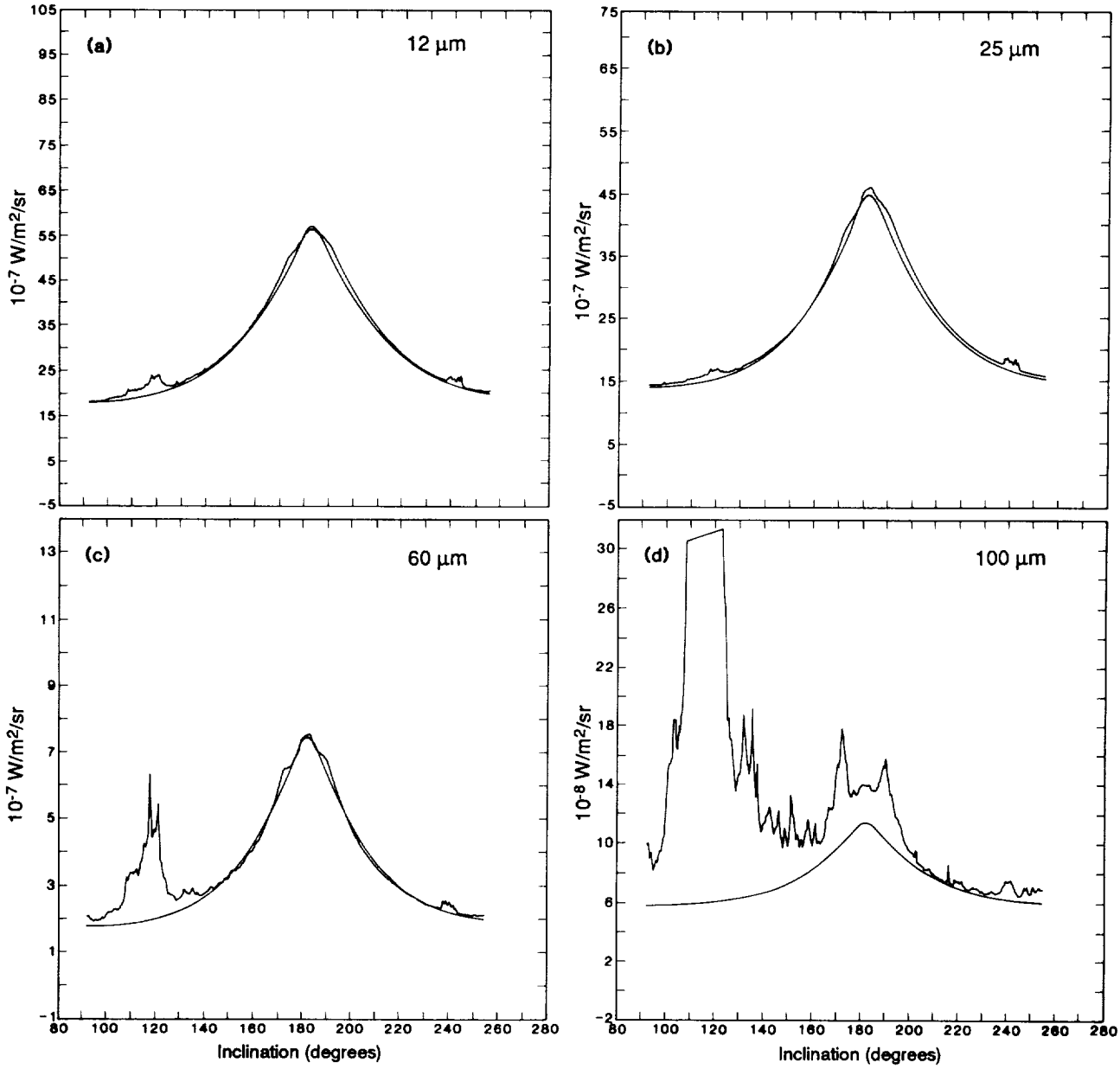

Figure G.4 A typical IRAS pole-to-pole scan with the zodiacal dust cloud model fit (solid line). This scan was at a solar elongation of 90°. The zodiacal dust bands are visible as bumps at the ecliptic plane (inclination 180°) and at $\pm \approx 10°$. The remaining structure is Galactic emission.

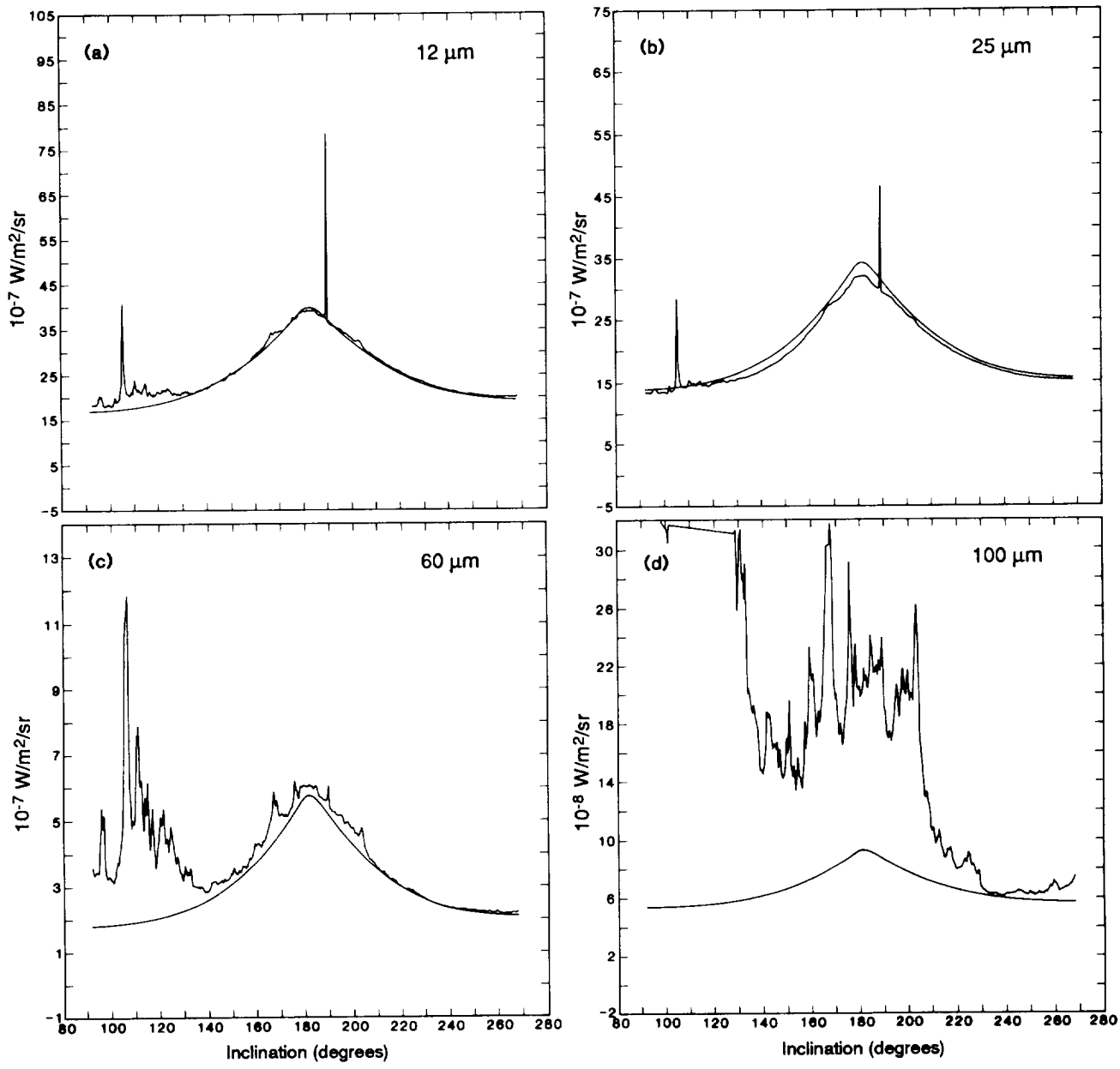

Figure G.5 Data and zodiacal dust cloud model prediction for a scan at solar elongation of 112°. The profiles are broader and less intense than those in Figure G.4 since this scan is looking through material farther from the Sun, which is both cooler and has a larger z scale height.

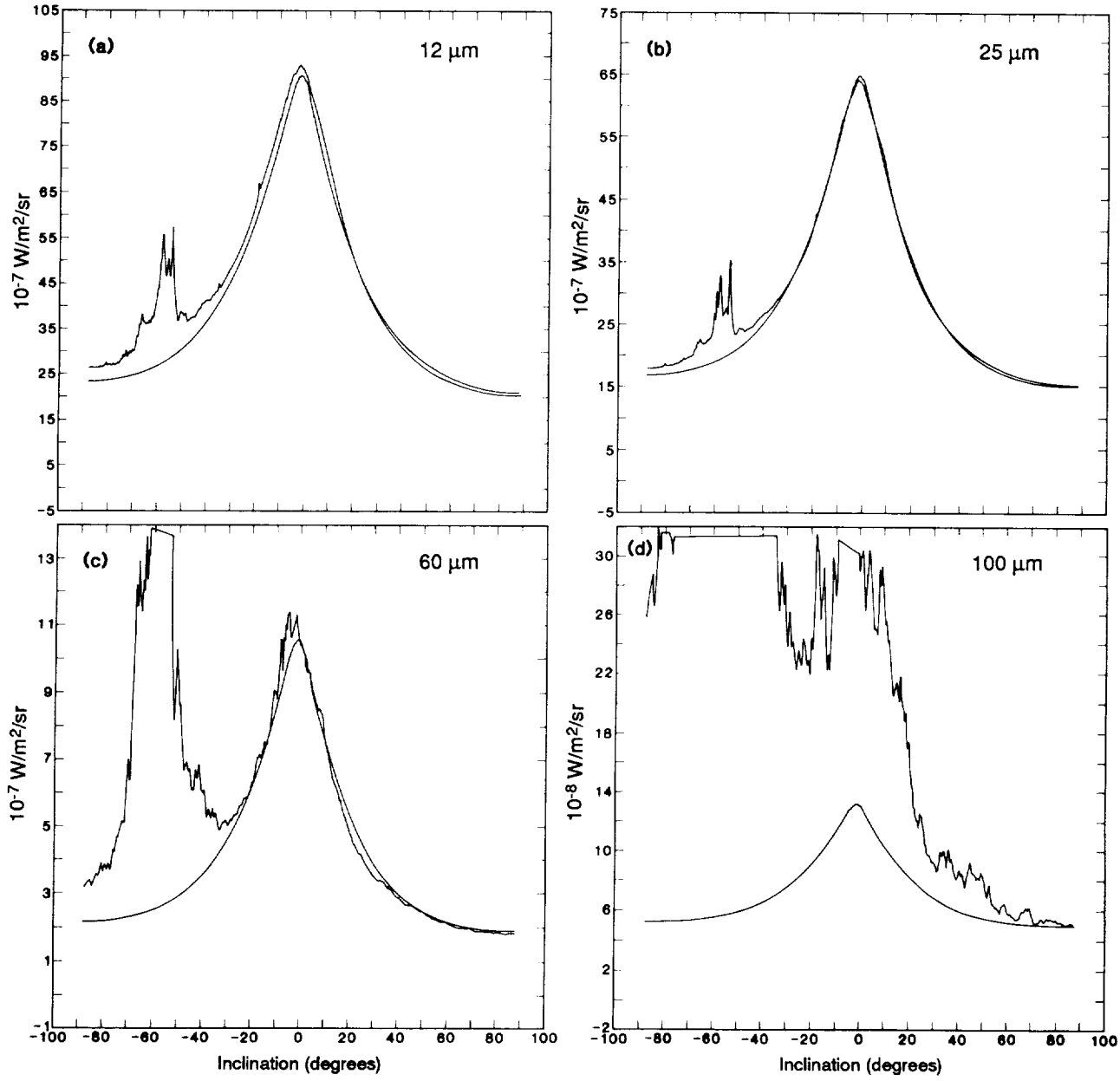

Figure G.6 Data and zodiacal dust cloud model prediction for a scan at solar elongation of 67°. The same discrepancy noted in Figure G.5 exists for these data. These profiles are narrower and more intense since this scan is observing material closer to the Sun.

Table G.2

Correlation Coefficients Between Model Parameters

Parameters												
Offsets (μm)												
25	60	100	ρ_0	α	β	γ	T_0	δ	λ_0	Ω	i	
−.11	0.00	0.00	0.30	0.24	0.24	0.18	−0.44	−0.26	0.00	−0.05	−0.01	12μm
	0.06	0.01	−0.52	−0.28	0.27	0.19	0.56	0.32	0.34	−0.11	0.04	25μm
		0.03	−0.06	−0.08	0.04	0.03	0.08	0.09	−0.31	−0.04	−0.01	60μm
			−0.02	−0.02	0.01	0.01	0.02	0.02	−0.05	−0.01	0.00	100μm
				0.73	0.25	0.0	−0.86	−0.55	−0.17	0.14	−0.19	ρ_0
					0.31	0.20	−0.77	−0.91	0.12	0.06	−0.16	α
						0.89	−0.08	−0.08	0.1	−0.47	−0.19	β
							−0.06	−0.11	0.12	−0.56	−0.10	γ
								0.78	0.18	−0.09	0.11	T_0
									−0.09	−0.05	−0.09	δ
										−0.0	−0.05	λ_0
											−0.09	Ω

The complete volumetric emissivity distribution description is given by

$$\rho = 1.43 \times 10^{-20}(R_0/r)^{1.80} \exp[-4.97z/r^{1.26}] \qquad \text{cm}^{-1} \tag{5}$$

and the temperature by

$$T = 266(R_0/R)^{0.36} \qquad \text{K.} \tag{6}$$

The implications of these profiles and the cloud orientation parameters will not be discussed here, but some discussion of the emissivity and background terms is needed. Both of these terms are quite ambiguous, the emissivity because it is a crude approximation and the background because it may well be merely a calibration effect.

The emissivity properties of the dust material are extremely uncertain, although their overall emissivity is probably quite high. Models of the absorption/emission behavior for various materials (Roser and Staude 1978) show that several likely candidates for the dust (eg., olivine, obsidian) have fairly flat (though very uneven) emission properties between about 10 and 30 μm but then drop off as λ^{-n} ($n = 1 - 3$) out to beyond 100 μm. Our approximation is very crude, but the results of our fit require a decreasing emissivity at long wavelength and relatively flat emissivity between 10 and 30 μm. The large width of the IRAS filters precludes finer analysis of the composition of the dust.

References

Briggs, R.E. 1962, *Astron. J.*, **67**, 710.

DIRBE Explanatory Supplement 19 July 1993, distributed by National Space Science Data Center (NSSDC).

Good, J.C., M.G. Hauser, and T.N. Gautier 1986, IRAS Observations of the Zodiacal Background, in "Advances in Space Research 1986," Proceedings of the XXVIth COSPAR Meeting.

IRAS Catalogs and Atlases: Explanatory Supplement 1988, ed. C.A. Beichman, G. Neugebauer, H.J. Habing, P.E. Clegg, and T.J. Chester (Washington, D.C.:GPO).

Leinert, C., M. Hanner, and E. Pitz 1978a, *Astron. Astrophys.*, **63**, 183.

Leinert, C., M. Hanner, H. Link and E. Pitz 1978b, *Astron. Astrophys.*, **84**, 119.

Leinert, C., M. Hanner, I. Richter, and E. Pitz 1980, *Astron. Astrophys.*, **82**, 328.

Leinert, C., I. Richter, E. Pitz, and B. Planck 1981, *Astron. Astrophys.*, **103**, 177.

Misconi, N.Y. 1980, "The Symmetry Plane of the Zodiacal Cloud Near 1 AU", in Solid Particles in the Solar System, eds. I. Halliday and B.A. McIntosh, (Reidel:Dordrecht), 49.

Mukai, T., and R.H. Giese 1984, *Astron. Astrophys.*, **131**, 355.

Murdock, T.L. and S.D. Price 1985, *Astron. J.*, **90**, 375.

Roser, S., and H.J. Staude 1978, *Astron. Astrophys.*, **87**, 381.

Trulsen, J., and A. Wikan 1980, *Astron. Astrophys.*, **91**, 155.

APPENDIX H

Zodiacal History File (ZOHF) Version 3.0

H.1 Introduction

The *IRAS Zodiacal History File* (ZOHF) Version 3.0 was released by IPAC in 1988. It replaced Version 2.0, which was released in 1986. Version 3.0 incorporates a number of improvements that are outlined below. A subsequent release in 1990, Version 3.1, fixed a problem found in Version 3.0. A statement of the problem and its effect is given below. All references to Version 3.0 in this appendix other than in §H.8 are applicable to Version 3.1.

The major improvements were in the calibration. The baseline calibration was improved and corrections for hysteresis effects were incorporated. The entire IRAS survey was rerun with the improved calibration. Other changes to the ZOHF included a format change, additional calibration improvements, position improvements, a sampling change, and several processing changes. Results of the verification tests are presented. This is not intended to be an exhaustive description of the ZOHF Version 3.0 or its analysis. Only essential information is presented to enable a researcher to use the ZOHF Version 3.0 product.

The ZOHF Version 3.0 incorporated the final calibration of the IRAS data. There are, however, still calibration differences at the few-percent level between observations. In particular, there remains a systematic difference between ascending and descending scans. This systematic problem is discussed in the section on anomalies below.

H.2 Product Description

The ZOHF Version 3.0 was created in the same manner as the previous versions. IRAS data from all detectors, except the 1/4–sized detectors, were boxcar averaged over eight seconds of time. This resulted in an approximately square beam 0.5° wide. The exact pixel sizes are given in Table H.1. The beam sizes have not changed from those in Version 2.0. Due to elimination of the smallest detectors, they are not the full width of the IRAS focal plane.

Table H.1
Pixel Sizes for ZOHF

Wavelength (μm)	Pixel Size (arcminutes) In-Scan	Cross-Scan
12	30.8	28.4
25	30.8	30.3
60	30.8	28.5
100	30.8	30.5

H.3 Format

The record format of the ZOHF Version 3.0 has changed from the format of Version 2.0 to give UTCS in centiseconds instead of seconds. The new format is given in Table H.2.

Table H.2

Format of ZOHF Version 3.0

(Replaces old version in *IRAS Explanatory Supplement 1988*)

byte	name	description	units	type
1	NSOP	SOP Number	-	I3
4	NOBS	OBS Number	-	I3
7	NUTCS[1]	Time UTCS	centisec	I10
17	INCL[1]	Inclination	degrees	F6.2
23	ELONG[1]	Solar Elongation	degrees	F6.2
29	BETA	Ecliptic Latitude	degrees	F6.2
35	LAMBDA	Ecliptic Longitude	degrees	F6.2
41	$I^1_{\nu_1}$	12 μm Brightness Density	Jy/sr	E10.4
51	I_{ν_2}	25 μm Brightness Density	Jy/sr	E10.4
61	I_{ν_3}	60 μm Brightness Density	Jy/sr	E10.4
71	I_{ν_4}	100 μm Brightness Density	Jy/sr	E10.4

[1] Refer to page X-62 of the *IRAS Explanatory Supplement 1988* for definitions.

H.4 Processing

Several improvements in data processing were made for ZOHF Version 3.0 and an error in Version 2.0 was corrected. The set of observations contained in Version 3.0 is slightly different from that of Version 2.0. A small set of survey scans erroneously excluded from Version 2.0 was included for the first time in Version 3.0. Observations that could not be properly calibrated using the new stimulator extraction method were excluded from Version 3.0. In total, Version 3.0 contains 0.07% fewer observations than Version 2.0.

Radiation spikes and other electronic glitches were removed by a deglitch processor prior to resampling the data (§III.A.3).

The data used in the ZOHF Version 2.0 were destriped with an algorithm which adjusted the gain and offset of each individual detector in a band to match those of the average of all detectors in that band. This destriper was *not* used for Version 3.0. This should have little effect since the destriper left the average value of the ZOHF unchanged and did not affect the striping caused by calibration variations between scans.

An error was found in Version 2.0 and corrected in Version 3.0 that advanced the position in-scan by 115″ for half of the mission data. Improvements in the satellite pointing

reconstruction made to support the *IRAS Faint Source Survey* 1992 were incorporated in the ZOHF Version 3.0. The impact of these improvements is generally not large relative to the resolution of the ZOHF (§III.A.3).

The sampling interval in the ZOHF Version 3.0 is eight seconds and there is *no* overlap between adjacent in-scan pixels. Because the ZOHF Version 2.0 was made with overlapping adjacent in-scan pixels, the file size of Version 3.0 is reduced by a factor of two as compared to Version 2.0.

H.5 Calibration

Several important changes were made in the IRAS calibration software. These are detailed in §III.A.2 of this Supplement.

H.6 Analysis Results

Several general analyses were done at IPAC to verify the ZOHF Version 3.0 data and characterize it with respect to Version 2.0.

H.6.a *Gain and Offset*

To compare intensities, each Version 3.0 observation was linearly fit to its counterpart in Version 2.0. The average gain and offsets of these fits as well as the maxima and minima for the mission are given in Table H.3. The mission mean gain and offset is approximately the value expected from the calibration changes that were implemented for Version 3.0. The mission extremes of gain and offset are caused by attempting to fit a linear transformation to the detector nonlinearities encountered when especially bright sources are covered during a scan.

Table H.3

Gain and Offset of each Version 3.0 Observation Compared to each Version 2.0 Observation

Coefficient	Wavelength Band (μm)	Mission Mean	Error of Mean (1 σ)	Mission Maximum	Mission Minimum
GAIN	12	0.896	0.013	1.083	0.685
	25	0.919	0.022	1.420	0.713
	60	1.075	0.042	1.344	0.706
	100	1.031	0.082	1.999	0.505
OFFSET (10^6 $Wm^{-2}sr^{-1}$)	12	-0.028	0.072	.441	-0.680
	25	-0.158	0.065	0.452	-1.092
	60	-0.008	0.021	0.120	-0.142
	100	0.014	0.018	0.227	-0.118

H.6.b *Position*

The cumulative effect of the position correction and the improved interpolation scheme can be shown by differencing the position given in the ZOHF to a position predicted in the Observation Parameter File for each ZOHF record in Versions 2.0 and 3.0. The Observation Parameter File is an internal IPAC file that summarizes the pointing information for each scan to an accuracy of about 20″. Histograms of these differences are given in Table H.4. Note that Version 3.0 compares much better to the Observation Parameter File than does Version 2.0. It should also be noted that both versions of the ZOHF were compared to the Version 2.0 Observation Parameter File (a Version 3.0 Observation Parameter File, which would reflect the improved pointing, does not exist). It is likely that the ZOHF Version 3.0 positions are actually slightly better than the histogram shows.

Table H.4

Histograms of Comparison of ZOHF Positions with the Observation Parameter File

Difference (″)	Version 2 (%)	Version 3.0 (%)
0-10	39.0	37.7
10-20	15.7	23.6
20-30	9.1	17.4
30-40	5.9	12.0
40-50	4.2	7.0
50-60	3.3	2.1
60-70	2.7	.1
70-80	2.5	**
80-90	2.2	0.
90-100	1.9	0.
100-200	11.9	0.
200-300	1.5	0.
300-400	**	0.
400-500	**	0.
500-600	0.	0.
600-700	**	0.
700-800	**	0.
800-900	0.	0.
900-1000	**	0.
1000-2000	**	0.
>2000	**	0.

** represents a percentage < .05

H.6.c *Calibration Verification*

M.G. Hauser, L.J. Rickard and J. Vrtilek at Goddard Space Flight Center have performed extensive analyses of the ZOHF checking noise level and calibration consistency. Their results are summarized here.

If the IRAS calibration system were working perfectly, the brightness of the TFPR measured during survey observations should agree with the TFPR model used during the daily baseline calibration observations. The discrepancy between these two values of TFPR brightness gives some measure of the stability and uncertainty of the baseline. The difference between the survey observations of the TFPR and the model is shown in Figure H.1. The scatter is seen to be approximately 3% at 12 and 25 μm, 4% at 60, and 8% at 100 μm.

We should be able to re-derive from the ZOHF the same variable part of the TFPR model that we used in the calibration. Hauser *et al.*'s check of the variable part of the TFPR model due to the inclination of the symmetry plane of the zodiacal dust reproduced that part of the TFPR model to within the model's internal consistency discussed above. This check is done by differencing the ends of survey scans that cross both ecliptic poles. It should be quite accurate and free from the effects of baseline drift. Derivation of the variability due to eccentricity from the survey data alone is unreliable because residual baseline drifts are not eliminated and are large enough to affect the calculated eccentricity term seriously. Hauser *et al.* also found systematic differences between ascending and descending survey scans, see §H.7 below.

H.7 Anomalies

Several users of the ZOHF Version 2.0 have found that the descending scans (scans which progress with decreasing ecliptic latitude) are systematically brighter at the ecliptic plane than are the ascending scans (scans which progress with increasing ecliptic latitude.) Note that, in the IRAS orbit, descending scans always look behind the Earth in its orbit while ascending scans always look ahead. We have investigated this effect and found that a discrepancy on the order of 2% (2% at 12 and 60 μm, 1.5% at 25 μm, and 4% at 100 μm) is seen at the north ecliptic pole between the ascending and descending scans. At the pole the two sets of scans are looking at the same part of the sky and the difference should be zero. The error seen at the pole is within the uncertainties of the DC gain calibration.

This difference could be caused by a residual hysteresis effect in the DC response of the detector after crossing the South Atlantic Anomaly (SAA). The model implemented in calibration for handling hysteresis after the SAA was derived only for the AC response. The DC response was assumed to vary linearly with the AC response and was obtained by applying a scale factor to the AC response. This assumption may not be correct at the few-percent level.

Due to the survey scan strategy, descending scans dominate the first group of survey scans following an SAA crossing. These scans have elevated fluxes relative to the next group of scans, which are further from SAA and are predominantly ascending. In Figure

H.1, the abscissa is the ratio of the measured flux at the North Ecliptic Pole (NEP) and the flux calculated from the calibration model and assigned to the NEP. This is plotted against the time from the SAA crossing for the 12, 25, 60, and 100 μm bands. If the calibration were perfect, all measurements would be unity. The observations fall into groups along the time axis. Figure H.2 shows the mean flux ratio and population standard deviation for each grouping of scans at 12, 25, 60, and 100 μm.

In short, we believe that a large part of the ascending-descending asymmetry can be attributed to uncorrected calibration drifts. At this time, we cannot however eliminate the possibility that some of the asymmetry is a real feature of the sky.

H.8 Zodiacal History File Version 3.1

In calculating the averages for the ZOHF Version 3.0, some intensities were erroneously included. This problem affected a small number of ZOHF samples and was fixed in Version 3.1. No samples were affected at 12 or 25 μm, one sample at 60 μm and 382 (0.03%) samples at 100 μm. Most of the samples affected were in short low gain observations. The samples affected at 100 μm were lowered 23%, on average, with a maximum decrease of 45%.

References

IRAS Catalogs and Atlases: Explanatory Supplement 1988, ed. C. A. Beichman, G. Neugebauer, H. J. Habing, P. E. Clegg, and T. J. Chester (Washington, D.C.:GPO).

Moshir, M. *et al.*, 1992, Explanatory Supplement to the IRAS Faint Source Survey Version 2, JPL D-10015 8/92 (Pasadena:JPL).

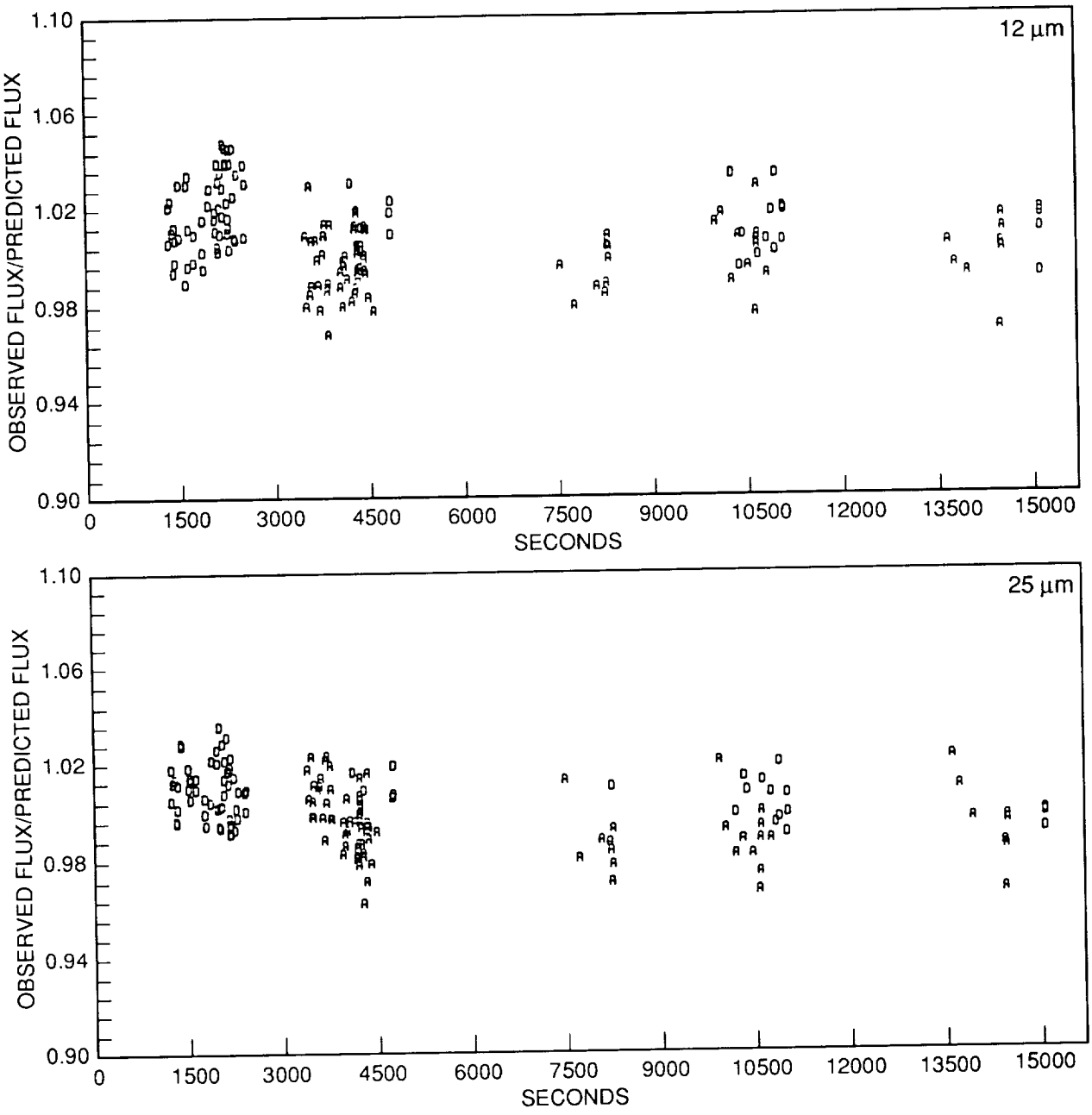

Figure H.1 Flux ratio at North Ecliptic Pole vs. time (seconds) from SAA crossing at 12, 25, 60, and 100 μm. (See text, Anomalies.)

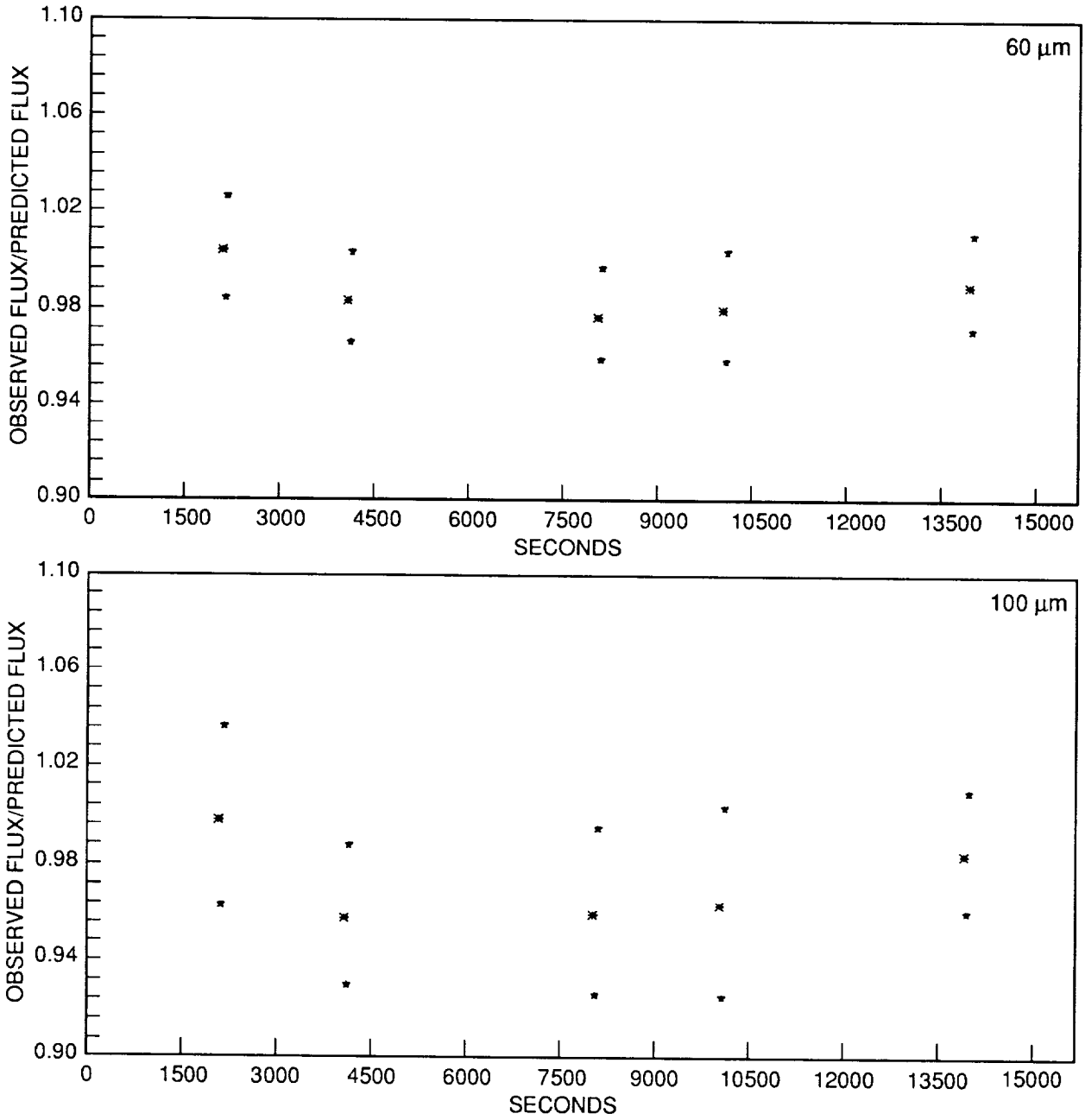

Figure H.2 (cont'd)

TECHNICAL REPORT STANDARD TITLE PAGE

1. Report No. 94-11	2. Government Accession No.	3. Recipient's Catalog No.
4. Title and Subtitle IRAS Sky Survey Atlas - Explanatory Supplement		5. Report Date May 1994 6. Performing Organization Code
7. Author(s)		8. Performing Organization Report No.
9. Performing Organization Name and Address JET PROPULSION LABORATORY California Institute of Technology 4800 Oak Grove Drive Pasadena, California 91109		10. Work Unit No. 11. Contract or Grant No. NAS7-918 13. Type of Report and Period Covered Supplement to Sky Survey Atlas
12. Sponsoring Agency Name and Address NATIONAL AERONAUTICS AND SPACE ADMINISTRATION Washington, D.C. 20546		14. Sponsoring Agency Code

15. Supplementary Notes

16. Abstract

This Explanatory Supplement accompanies the *IRAS Sky Survey Atlas* (ISSA) and the *ISSA Reject Set*. The first ISSA release in 1991 covers completely the high *ecliptic* latitude sky, $|\beta| > 50°$, with some coverage down to $|\beta| \approx 40°$. The second ISSA release in 1992 covers *ecliptic* latitudes of $50° > |\beta| > 20°$, with some coverage down to $|\beta| \approx 13°$. The remaining fields covering latitudes within 20° of the *ecliptic* plane are of reduced quality compared to the rest of the ISSA fields and therefore are released as a separate IPAC product, the *ISSA Reject Set*. The reduced quality is due to contamination by zodiacal emission residuals. Special care should be taken when using the *ISSA Reject* images (§IV.F).

In addition to information on the ISSA images, some information is provided in this Explanatory Supplement on the *IRAS Zodiacal History File* (ZOHF), Version 3.0, which was described in the December 1988 release memo (Appendix H).

The data described in this Supplement are available at the National Space Science Data Center (NSSDC) at the Goddard Space Flight Center. The interested reader is referred to the NSSDC for access to the *IRAS Sky Survey Atlas* (ISSA).

17. Key Words (Selected by Author(s))		18. Distribution Statement
Astronomy	Infrared Images	
Astrophysics	Images	
Astronomical Images	Atlas	
Infrared	Sky Surveys	
Infrared Sky Survey	IRAS	
Infrared Atlas	IRAS Images	

19. Security Classif. (of this report)	20. Security Classif. (of this page)	21. No. of Pages	22. Price
Unclassified	Unclassified	164	